

Determining the fatty acid compositions of human brown
and white adipose tissues in vivo using clinical proton
magnetic resonance spectroscopy

Licentiate's thesis
University of Turku
Department of Physics
Physics
2020
M.Sc. Kalle Koskensalo
Supervisors:
Prof. Riitta Parkkola
PhD. Jani Saunavaara
Prof. Petriina Paturi
Examiners:
Doc. Sven Månsson
Doc. Sergey Vasiliev

UNIVERSITY OF TURKU

Department of Physics and Astronomy

Koskensalo, Kalle Determining the fatty acid compositions of human brown and white adipose tissues in vivo using clinical proton magnetic resonance spectroscopy

Licentiate's thesis, 77 pp.

Physics

September 2020

Brown adipose tissue (BAT) of adult humans is metabolically active tissue which has been shown to have health-benefiting effects, such as preventing from type 2 diabetes and obesity. To develop BAT based treatment methods for obesity or diabetes the metabolism of the BAT tissue has to be well-known. Proton magnetic resonance spectroscopy (^1H MRS) is a radiation-free method for studying adipose tissue of living subjects. The method has mostly been used for assessing the fat fraction of the tissue but it also provides values for the fatty acid properties, namely, fractions of saturated (SFA), monounsaturated (MUFA) and polyunsaturated fatty acids (PUFA) as well as their carbon chain length. So far these properties of BAT have not been studied in living human subjects.

The subject of this thesis was to first develop a protocol for fatty acid composition measurement and validating it using lipid samples. Next, the protocol was used for determining fatty acid composition of human BAT and white adipose tissue (WAT) in both ambient condition and cold acclimation.

The validation study supported the application of the method for human subjects although the determination of one of the parameters, fatty acid chain length, seemed imprecise. The rest of the parameters correlated well with the real values.

The human study results indicated that human BAT and WAT have only negligible difference in the fatty acid composition between each other in the ambient condition although BAT has lower fat fraction than WAT. Cold exposure however seemed to change the fatty acid characteristics differently in BAT and WAT. In BAT the fractions of SFA and PUFA decreased in cold exposure while the fraction of MUFA increased. In WAT a decrease of PUFA was detected but the other parameters remained unchanged. The cold exposure did not have an effect on the fat fraction of the tissues. Additionally chain length elongation was observed in BAT although the determined chain length values were considerably shorter than in literature.

In conclusion, a cold exposure induced change in fatty acid characteristics can be detected even though no change in fat fraction is detected. Thus determining fatty acid characteristics might be a sensitive method for detecting activation of BAT.

TURUN YLIOPISTO

Fysiikan ja tähtitieteen laitos

Koskensalo, Kalle Ihmisen ruskean ja valkean rasvakudoksen rasvahappokoostumuksen määrittäminen in vivo kliinisellä protonimagneettispektroskopiolla

Lisensiaatin tutkielma, 77 sivua.

Fysiikka

Syyskuu 2020

Aikuisten ihmisten ruskea rasva on aineenvaihdunnallisesti aktiivista kudosta, jolla on todettu olevan terveyden kannalta hyödyllisiä vaikutuksia, sillä se suojaa muun muassa tyyppin 2 diabetekselta ja lihavuudelta. Ruskean rasvan aktivoitumiseen perustuvien lihavuuden ja diabeteksen hoitomenetelmien kehittäminen edellyttää kudoksen aineenvaihdunnan hyvää tuntemusta. Protonimagneettispektroskopia on ionisoivaa säteilyä käyttämätön menetelmä, jota voidaan käyttää elävien kohteiden rasvakudoksen tutkimiseen. Metodia on käytetty kudosten rasvapitoisuuden määrittämiseen, mutta sillä voidaan määrittää myös rasvahappojen ominaisuudet, kuten tyydyttyneiden, kertatyydyttymättömien ja monityydyttymättömien rasvahappojen osuudet sekä rasvahappojen hiiliketjun pituus. Tähän mennessä menetelmällä ei ole tutkittu elävien ihmisten ruskeaa rasvaa.

Tämän tutkielman aiheena oli ensin kehittää rasvahappokoostumuksen mittausprotokolla ja validoida se käyttämällä rasvanäytteitä. Seuraavaksi protokollaa käytettiin ihmisen ruskean ja valkean rasvan koostumuksen mittaamisen huoneenlämpötilassa ja kylmäältistuksessa.

Validaatiotutkimus osoitti, että menetelmää voidaan soveltaa ihmiskohteisiin vaikka yhden muuttujan, rasvahappojen ketjun pituuden, määrittäminen vaikutti epätarkalta. Muut muuttujat korreloivat hyvin todellisten arvojen kanssa.

Ihmiskoe osoitti, että ihmisen ruskea ja valkea rasvakudos eroavat rasvahappojen ominaisuuksien osalta häviävässä määrin toisistaan huoneenlämpötilassa, vaikka ruskea rasva on vähemmän rasvapitoista kuin valkea. Kylmäältistus näytti sen sijaan muuttavan arvoja eri tavalla ruskeassa ja valkeassa rasvassa. Ruskeassa rasvassa tyydyttymättömien ja monityydyttyneiden rasvahappojen osuus väheni kylmäältistuksessa kun taas kertatyydyttymättömien osuus kasvoi. Myös valkeassa rasvassa havaittiin monityydyttymättömien osuuden väheneminen, mutta muissa parametreissa ei havaittu muutoksia. Kylmäältistuksella ei ollut vaikutusta kudosten kokonaisrasvapitoisuuteen. Lisäksi ketjun pituuden kasvu havaittiin ruskeassa rasvassa, vaikka määritetyt ketjunpituusarvot olivat huomattavasti lyhyempiä kuin kirjallisuudessa raportoidut.

Yhteenvedon voidaan todeta, että kylmäältistuksen aikaansaamat muutokset ruskean rasvan rasvahappojen ominaisuuksissa voidaan havaita, vaikka rasvapitoisuuden muutosta ei havaita. Näin ollen rasvahappojen ominaisuuksien määrittäminen saattaisi olla herkkä menetelmä ruskean rasvan aktivaation havaitsemiseen.

ABBREVIATIONS

^{18}F -FDG	Fluorine-18 fluorodeoxyglucose
^1H	Proton
acetyl-CoA	Acetyl coenzyme A
ADP	Adenosine diphosphate
AGPAT	1-acylglycerol-3-phosphate acyltransferase
AP	Anterior-posterior
ATP	Adenosine triphosphate
BAT	Brown adipose tissue
BMI	Body-mass-index
cAMP	Cyclic adenosine monophosphate
CL	Chain length
CT	Computed tomography
DGAT	Diacylglycerol acyltransferase
DWI	Diffusion weighted imaging
FF	Fat fraction
FH	Feet-head
FID	Free induction decay
f_{mufa}	Fraction of monounsaturated fatty acids
f_{pufa}	Fraction of polyunsaturated fatty acids
f_{sfa}	Fraction of saturated fatty acids
FTHA	14-(<i>R,S</i>)-Fluorine-18-Fluoro-6-thiaheptadecanoic acid
FWHM	Full-width at half-maximum
GPAT	Glycerol-3-phosphate acetyltransferase
HDL	High-density-lipoproteins
HSL	Hormone-sensitive lipase
HU	Hounsfield units
LDL	Low-density lipoproteins
MCT	Medium-chain triglyceride
MGL	Monoglyceride lipase
MIBG	^{123}I - <i>meta</i> -Iodobenzylguanidine
MIBI	$^{99\text{m}}\text{Tc}$ -Methylisobutylisonitrile
MRI	Magnetic resonance imaging
MRS	Magnetic resonance spectroscopy
MSOT	Multispectral optoacoustic tomography
Myf5	Myogenic factor 5
NADH	Nicotinamide adenine dinucleotide
ndb	Number of double bonds
NIRS	Near-infrared spectroscopy
nmidb	Number of methylene interrupted double bonds
NMR	Nuclear magnetic resonance
NMR	Nuclear magnetic resonance
PAP	phosphatidic acid phosphatase
PDFF	Proton density fat fraction
PET	Positron emission tomography
pKA	Protein kinase A
PRESS	Point Resolved Spectroscopy

RF	Radiofrequency
RL	Right-left
SNR	Signal-to-noise ratio
SPECT	Single-photon emission computed tomography
STEAM	Stimulated Echo Acquisition Mode
TCA	Tricarboxylic acid cycle
TE	Time of echo
TM	Mixing time
TR	Repetition time
WAT	White adipose tissue

CONTENTS

Introduction	1
2 Review of literature	2
2.1 Lipids	2
2.2 The adipose organ.....	4
2.3 White adipose tissue (WAT)	5
2.3.1 Distribution of WAT	5
2.3.2 White adipocyte appearance	5
2.3.3 Fatty acid metabolism in WAT.....	6
2.4 Brown adipose tissue	10
2.4.1 Brown adipose tissue distribution.....	11
2.4.2 Brown adipocyte appearance	12
2.4.3 Thermogenesis in BAT.....	13
2.4.4 Uptake of fatty acids and other substrates in BAT	14
2.5 Non-invasive methods for studying brown adipose tissue	14
2.5.1 Positron emission tomography	15
2.5.2 Single-photon emission imaging	16
2.5.3 Computed tomography	17
2.5.4 Ultrasound	17
2.5.5 Near-infrared spectroscopy.....	18
2.5.6 Photoacoustic imaging.....	18
2.5.7 Thermal imaging and thermal probes	19
2.5.8 Magnetic resonance methods.....	19
2.6 Proton NMR physics and techniques.....	20
2.6.1 Nuclear magnetic resonance	21
2.6.2 Chemical shift.....	23
2.6.3 J-coupling	24
2.6.4 Macroscopic magnetization	25
2.6.5 T1 relaxation.....	27
2.6.6 T2 relaxation.....	28
2.6.7 MR Imaging.....	29
2.6.8 MR Spectroscopy	31
2.6.9 Assessment of relaxation times	32
2.6.10 Assessment of fatty acid properties	34
2.6.11 Assessment of fat fraction	35
3 Objectives of the study	37

4	Materials and methods.....	38
4.1	Samples for phantom validation.....	38
4.2	Construction of a phantom.....	38
4.3	Phantom measurements.....	39
4.4	Data postprocessing.....	40
4.5	Fatty acid properties of the samples.....	41
4.6	Fat fraction of butter.....	41
4.7	Spectral quality in the validation experiment.....	41
4.8	In vivo human study design.....	42
4.9	Cold exposure.....	42
4.10	Human measurements.....	42
4.11	Statistical analysis.....	44
5	Results.....	46
5.1	Relaxation times of the samples.....	46
5.2	Fatty acid properties of the samples.....	47
5.3	Fat fraction of butter.....	51
5.4	Spectral quality of the validation experiment.....	52
5.5	Human study relaxation time results.....	54
5.6	Human study fatty acid characteristics results.....	54
5.7	Human fat fraction results.....	56
6	Discussion.....	58
6.1	Phantom study.....	58
6.2	Human study.....	59
7	Limitations.....	61
8	Conclusions.....	62
9	Acknowledgements.....	63
10	References.....	64

INTRODUCTION

Brown adipose tissue (BAT) is a thermogenic organ which is characteristic to small animals and human infants [Cannon and Nedergaard 2004]. In 2009 active BAT was found also in adult humans [van Marken Lichtenbelt et al 2009; Virtanen et al 2009; Cypess et al. 2009] and further research proved it to have high metabolic activity. Improving BAT function has been suggested as a potential therapy method for type 2 diabetes and obesity because of the increased metabolic activity and the tissue's ability to clear lipids and glucose from blood circulation [Cypess and Kahn 2012]. Thus understanding BAT function and especially its lipid metabolism is highly important for future development of the treatment utilization of BAT.

Active BAT in adult humans was originally detected with positron emission tomography (PET) and computed tomography (CT). Fluorine-18-fluorodeoxyglucose (^{18}F -FDG) PET/CT imaging is still considered as the golden standard for the detection of active BAT [Frankl et al. 2019]. Also lipid metabolism has been studied using different PET tracers, such as 14-(*R,S*)-[^{18}F]Fluoro-6-thiaheptadecanoic acid (FTHA). The drawback of the PET/CT method is ionizing radiation which is a well-known risk for development of cancer [Hall et al. 2017]. Several radiation-free methods have been suggested and also methods that could be used for the detection of BAT without the need for cold-exposure which is very uncomfortable for the study subjects [Chondronikola et al. 2017]. The most popular radiation-free method is magnetic resonance imaging (MRI) which can provide superb soft tissue contrast with different kinds of weighing and also imaging sequences for studying BAT function [Wu et al. 2020]. Magnetic resonance spectroscopy (MRS) is a measurement which is usually performed during an MRI study. MRS is usually not used to form an anatomical image of the object. Instead the frequencies of the signal are studied in detail. Using the amplitudes and frequencies of the signals substances can be identified and their relative or absolute concentrations calculated. [Rhodes 2017] In addition, MRS can be used for probing the temperature of the subject [Koskensalo et al. 2017]. Importantly for adipose tissue research, MRS can be used for identifying properties of fatty acids. These are number of double bonds, number of methylene interrupted double bonds, carbon chain length and fractions of monounsaturated, polyunsaturated and saturated fatty acids. Previously fatty acids properties of BAT have been studied only in animal tissue samples [Hamilton et al. 2011; Ren 2008; Lunati et al 2001].

The aim of this licentiate's thesis is to determine fatty acid properties in human BAT and white adipose tissue (WAT) in vivo and also to determine how they are changed in cold exposure. The measurement of fatty acid properties is first validated using oil samples.

2 REVIEW OF LITERATURE

2.1 Lipids

Lipids are defined as biological substances that are soluble in nonpolar solvents [Moss et al 1995]. Different types of lipids are triglycerides, phospholipids, steroids, waxes and fatty acids which are the simplest forms of lipids [Tortora and Derrickson 2011]. Fatty acids consist of a carboxyl group (-COOH) which is located at one end of the molecule, a chain of carbon atoms attached to hydrogen atoms and a methyl group (-CH₃) which is at the other end of the molecule (Figure 1). The carboxyl group is hydrophilic and therefore ionizes in water whereas the methyl end is hydrophobic. In biological systems the total number of carbon atoms in the molecule varies typically between 10 and 28. [Desbois and Smith 2009] Fatty acids with 7 or less carbon atoms are classified as short-chain, the ones with 8 to 16 carbons are medium-chain and those with more than 16 carbon atoms are long-chain. [Beare-Rogers et al. 2001]

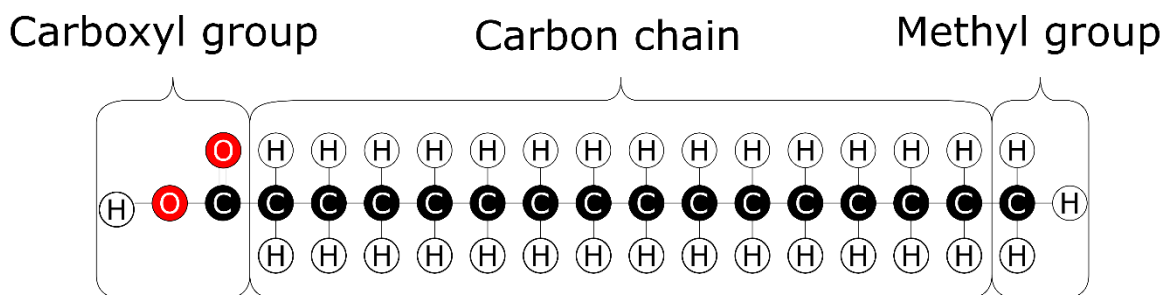


Figure 1. Molecule groups of a fatty acid molecule (stearic acid) with 16 carbon atoms. Thus it can be considered as a medium chain fatty acid.

Fatty acids are generally characterized by the number of double covalent bonds between the molecules: a saturated fatty acid has no double bonds, monounsaturated has one and polyunsaturated several double bonds (Figure 2) [Tortora and Derrickson 2011]. A simple way of naming fatty acids is the lipid number C:D where C is the number of carbon atoms in the fatty acid and D is the number of double bonds. The C:D notation is usually accompanied by the ω classification which indicates the number of atoms between the double bond and the methyl (CH₃) end (ω being the last letter of Greek alphabets). For example in Figure 2 the linoleic acid (B) has 18 carbon atoms, two double bonds and the first double bond is located six carbon atoms away from end of the molecule. Thus it is identified as C18:2 ω 6. [Laposata 1995]

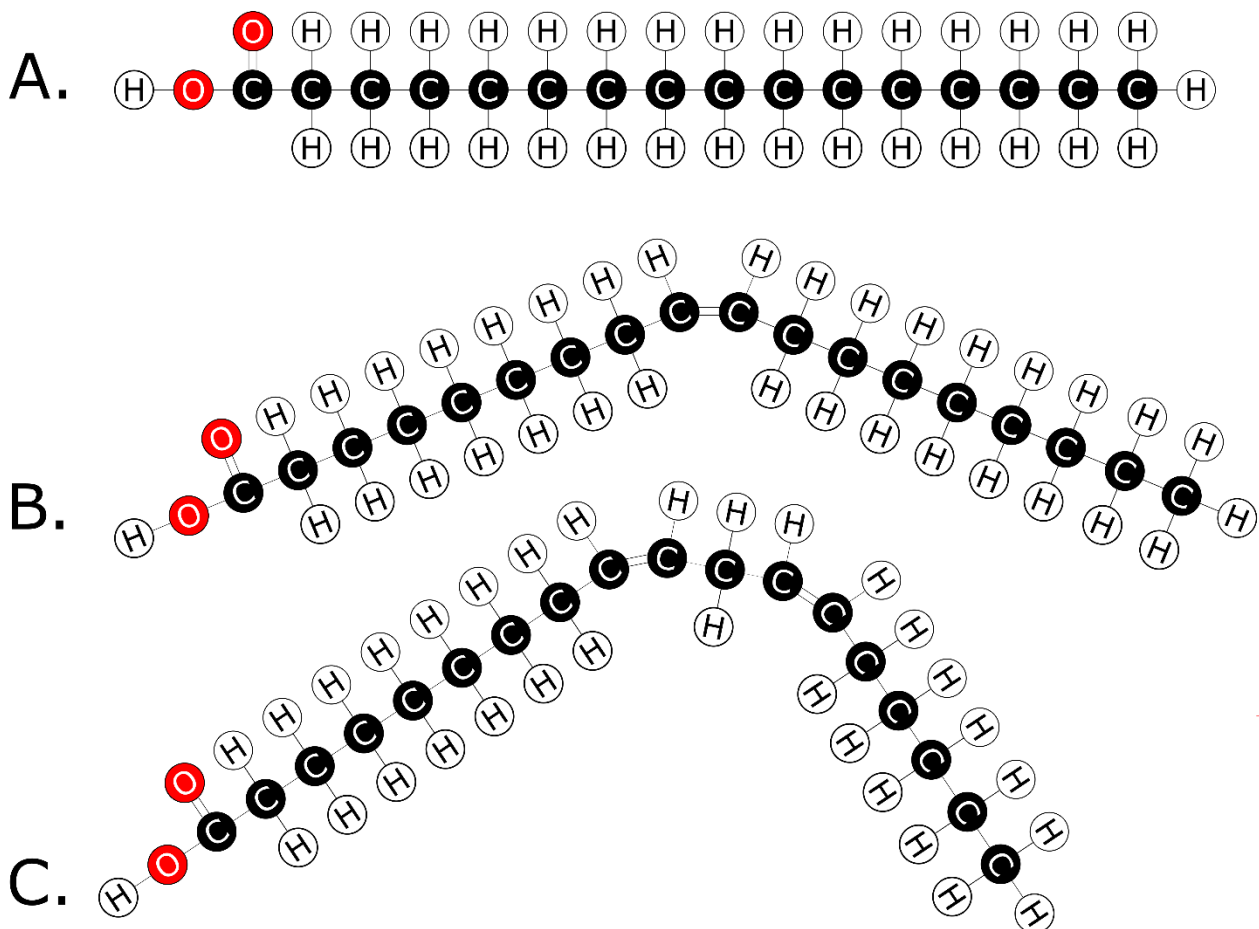


Figure 2. Different types of fatty acids in human adipose tissue. A: saturated palmitic acid $C_{16}H_{32}O_2$ (C16:0). B: monounsaturated oleic acid $C_{18}H_{34}O_2$ (cis C18:1 ω 9. The most abundant in humans). C: Linoleic acid $C_{18}H_{32}O_2$ (cis C18:2 ω 6). [Bolton-Smith et al 1997; Yoon et al 2018]

Additionally the unsaturated fatty acids can also be classified by the stereochemistry of the hydrogen atoms around the double bond: in cis configuration the hydrogen atoms are on the same side of the carbon chain whereas in trans configuration they are on the opposite sides. [Moss 1996] Cis double bond causes the fatty acid to bend, as in both Oleic and linoleic acids in Figure 2, whereas trans straightens the molecule as in Figure 3. Thus trans fatty acids are more closely packed than cis fatty acids [Laposata 1995]. The same obviously applies also to saturated fatty acids [Tortora and Derrickson 2011]. In human body different kinds of fatty acids are needed for different tasks. Most of them are derived directly from consumed diet but most of them can also be synthesized from glucose or other fatty acids. However, in human diet saturated and trans fatty acids lower the level of healthy high-density-lipoproteins (HDL) and raise the level of unhealthy low-density lipoproteins (LDL) increasing the risk of cardiovascular disease. A positive correlation has been found between the metabolic profile of type 2 diabetes and high intake of saturated fatty acids. Trans fatty acids are also related to metabolic diseases as they promote inflammation. [Calder 2015]

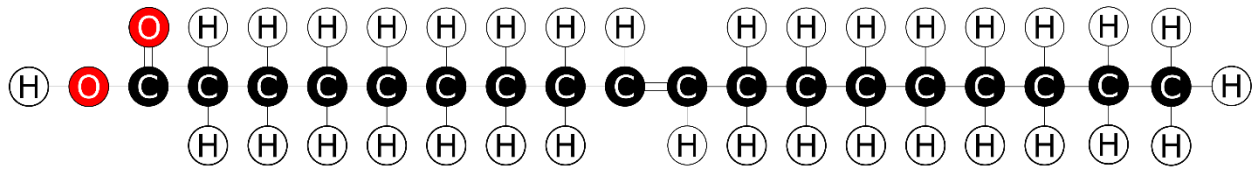


Figure 3. Elaidic acid (trans C18:1 ω9) which is the trans isomer of oleic acid (Figure 2) [Yoon et al 2018].

In biological systems fatty acids are utilized in several functions one of which is the production of adenosine triphosphate (ATP). The hydrolysis of ATP is the main source of biochemical energy [Kamerlin et al 2013]. When fatty acids are joined (esterified) with glycerol they form triglycerides (also known as triacylglycerols) (Figure 4) which act as a dense energy storage in biological systems. [Tortora and Derrickson 2011] In higher eukaryotes triglycerides are primarily stored into adipose tissue [Ahmadian et al 2007]

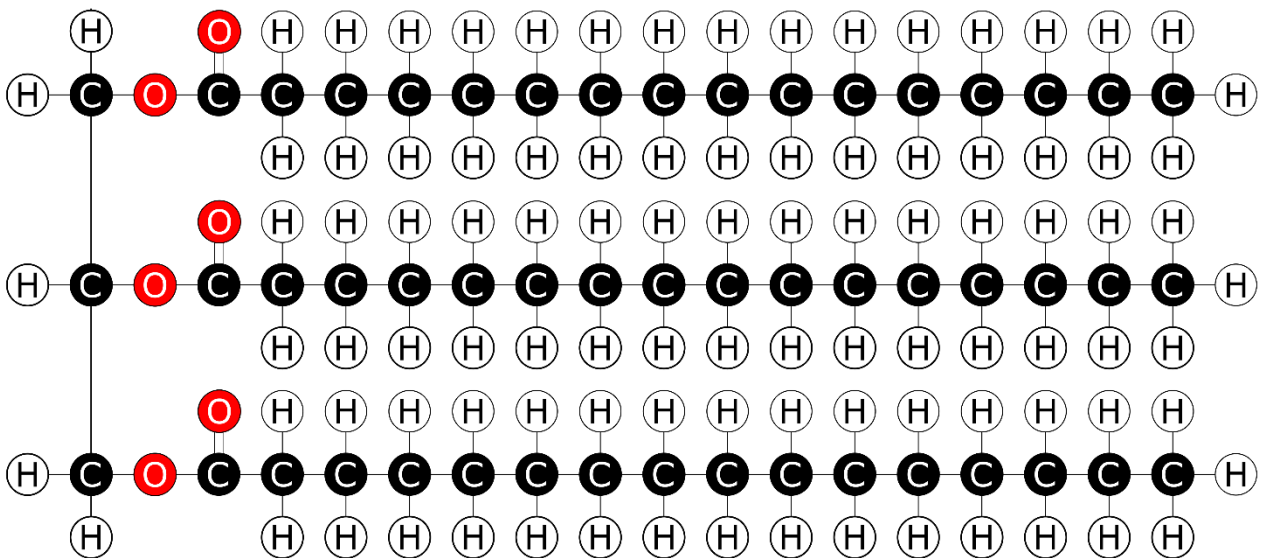


Figure 4. A triglyceride molecule composed of a glycerol backbone and three palmitic acid molecules.

2.2 The adipose organ

The adipose tissue is a complex organ with high metabolic and endocrinal activity [Kereshaw and Flier 2004]. It consists of several depots which contribute to many important tasks such as thermogenesis, lactation, immune responses and energy storage [Cinti 2012]. The depots are located in two major compartments: under the skin (subcutaneous) and inside the trunk (intra-abdominal) (Figure 5) [Ràfols 2014; Cinti 2011].

The main cells of adipose tissue are called adipocytes which in mammals can be divided into two types: white and brown [Cinti 2012]. The functions of both are very different [Saely et al. 2010]. In addition to adipocytes, adipose tissue contains several other cells and tissues which have active interaction with adipocyte functions. Some of these are preadipocyte cells, connective tissue matrix, vascular cells, neural tissue cells, immune cells, macrophages (inflammatory cells) and fibroblasts. [Kereshaw and Flier 2004; Ibrahim 2010]

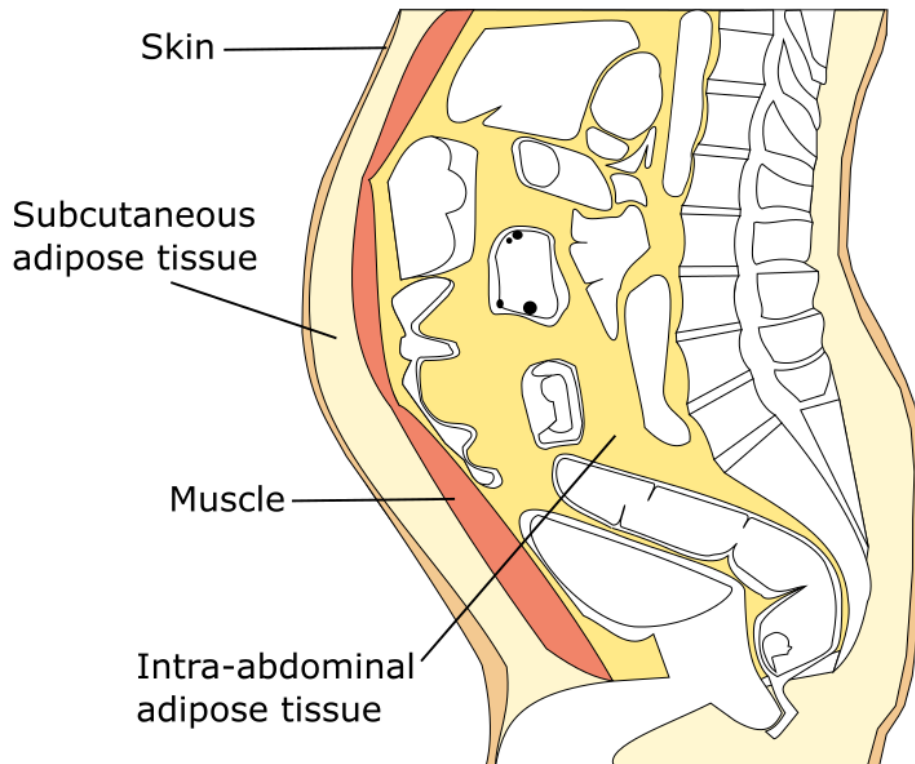


Figure 5. A sagittal view (from the left side) of human abdominal area depicting the locations of the two major adipose tissue compartments: subcutaneous is located between the skin and muscle layers and intra-abdominal is located inside the trunk.

2.3 White adipose tissue (WAT)

The white adipose tissue (WAT) acts mainly as an energy storage [Gesta et al. 2007]. The adipocytes below the dermal skin are insulating material and form a physical barrier against microbial infection [Alexander et al. 2015]. For vital organs WAT provides isolation and mechanical protection [Ràfols 2014].

2.3.1 Distribution of WAT

In humans WAT is distributed throughout the body. The main subcutaneous WAT depots are in buttocks, thighs and abdomen while in intra-abdominal WAT they are the omental, visceral and retroperitoneal depots. Smaller amounts also exist in bone marrow, face and pericardial, perivascular, retro-orbital and intramuscular areas. [Gesta et al. 2007] Distribution and accumulation of WAT is greatly influenced by genetics [Nelson et al. 2000].

2.3.2 White adipocyte appearance

A white adipocyte (Figure 6) contains a lipid vacuole which can be more than 90% of the cell volume. It is separated from the cytoplasm by a barrier which contains functionally important proteins. Other organs of a

white adipocyte are nucleus, thin, elongated mitochondria with randomly orientated cristae, under-developed Golgi apparatus, endoplasmic reticulum and lysosomes. [Cinti 2009; Cinti 2011]

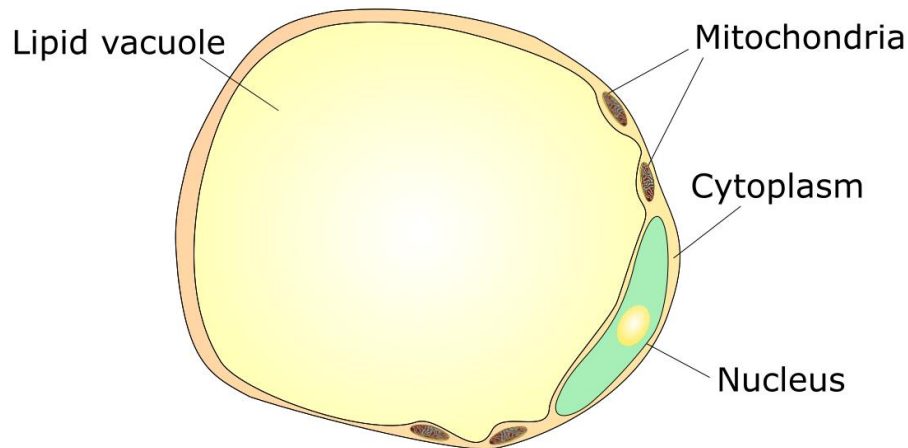


Figure 6. A white adipocyte with some of the characteristic cell organs.

2.3.3 Fatty acid metabolism in WAT

When energy intake exceeds expenditure subcutaneous adipose tissue stores the excess fatty acids and glycerol as triglycerides in a process called lipogenesis [Ràfols 2014] or more generally triglyceride synthesis or esterification [Ahmadian et al. 2007].

The major sources of fatty acids are diet and de novo synthesis. In the former ingested water-insoluble triglycerides are emulsified and hydrolyzed to monoglycerides and free fatty acids before being absorbed in the intestinal lumen. In the de novo synthesis carbohydrates from the circulation are converted into fatty acids. This occurs primarily in the liver and adipose tissue. In mammals the end product of de novo fatty acid synthesis is mostly palmitic acid ($C_{16}:0$, $C_{16}H_{32}O_2$, see Figure 2) and small amounts of Stearic acid ($C_{18}:0$, $C_{18}H_{36}O_2$). These saturated fatty acids are further elongated and desaturated because unsaturated $\omega 3$, $\omega 6$, $\omega 7$ and $\omega 9$ fatty acids are also needed in the body. [Lehner and Kukis 1996; Lapasota 1995] However, $\omega 3$ and $\omega 6$ cannot be generated but have to be obtained in the diet. Therefore they are called the essential fatty acids. [Lapasota 1995] Fatty acids as such are not soluble in water. Therefore they have to be attached to transporter proteins called lipoproteins to be delivered through the blood circulation. The types of lipoproteins are chylomicrons, very-low-density lipoproteins (VLDL), low-density lipoproteins (LDL) and high-density-lipoproteins (HDL). Each type of lipoprotein contains specific amount of proteins, triglycerides, phospholipids and cholesterol. [Schumaker and Adams 1969]

Fatty acids in the diet influence the fatty acid composition of blood serum triglycerides in hours, serum cholesterol esters and phospholipids in 3 to 6 weeks, erythrocyte membrane phospholipids in months and adipose tissue in several months or years [Katan et al. 1997]. The carbon chain length, degree of unsaturation

and isomeric form of the fatty acids contribute to membrane properties, gene expression, metabolic signaling, eicosanoid production and energy expenditure. Thus the fatty acid profile of the diet influences several physiological processes in the body. For example, low degree of saturation of the tissues is related to good insulin sensitivity. [Vessby et al. 2002]

Lipogenesis occurs most actively in WAT, liver and intestine although all tissues are capable of it. WAT and liver use the phosphatic acid pathway, which will be covered in detail further in the text, whereas the intestine uses the monoglyceride pathway. [Lehner and Kukis 1996] Lipogenesis and uptake of fatty acids from blood stream are promoted by insulin hormone whereas leptin and β -adrenergic agonists reduce them [Qaid and Abdelrahman 2016].

The glycerol for the triglyceride synthesis is derived from glycolysis in the form of glycerol-3-phosphate or dihydroxyacetone. Another source is the 2-monoacylglycerol from lipolysis [Lehner and Kukis 1996].

The phosphatic acid pathway begins in both the endoplasmic reticulum and the mitochondria. Fatty acids enter the pathway in the form of fatty-acyl-CoA ester. At first lysophosphatic acid is synthesized from one fatty-acyl-CoA ester and glycerol-3-phosphate which includes the glycerol backbone of the upcoming triglyceride molecule. The reaction is catalyzed by glycerol-3-phosphate acetyltransferase (GPAT) enzyme which is believed to be a rate-limiting factor in the synthesis. At this point one fatty acid chain is attached to the glycerol while the two remaining fatty acid sites are occupied by -H (hydrogen) and -H₂O₃P (dihydrogen phosphite) (Figure 7). [Ahmadian et al. 2007; Lehner and Kukis 1996]

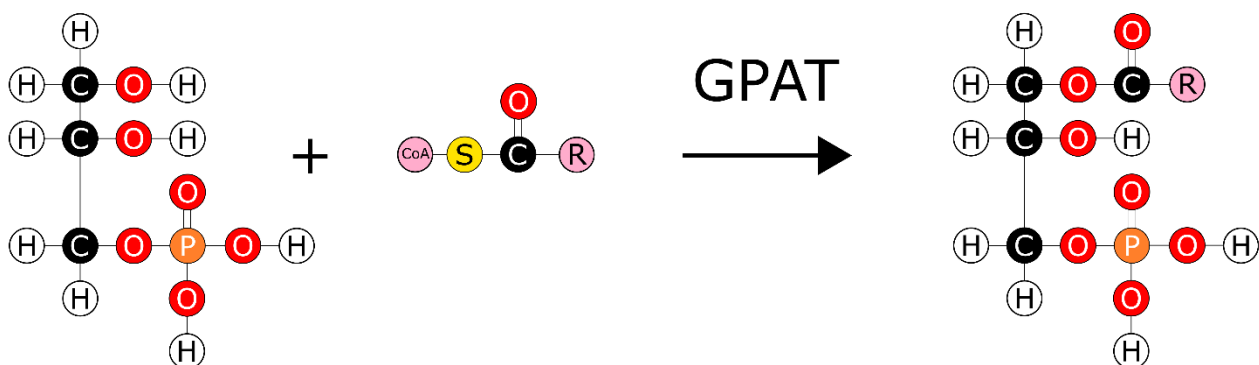


Figure 7. The first phase of triglyceride synthesis: in a chemical reaction catalyzed by GPAT enzyme glycerol-3-phosphate and fatty-acyl-CoA (R is the carbon chain of the fatty acid molecule and CoA denotes the CoA molecule) are transferred into lysophosphatic acid.

In the next phase lysophosphatic acid is converted into phosphatidic acid in a reaction catalyzed by 1-acylglycerol-3-phosphate acyltransferase (AGPAT) which is mainly present in endoplasmic reticulum. Again, fatty acid enters the reaction in the form of fatty-acyl-CoA ester (Figure 8). [Ahmadian et al. 2007; Lehner and Kukis 1996]

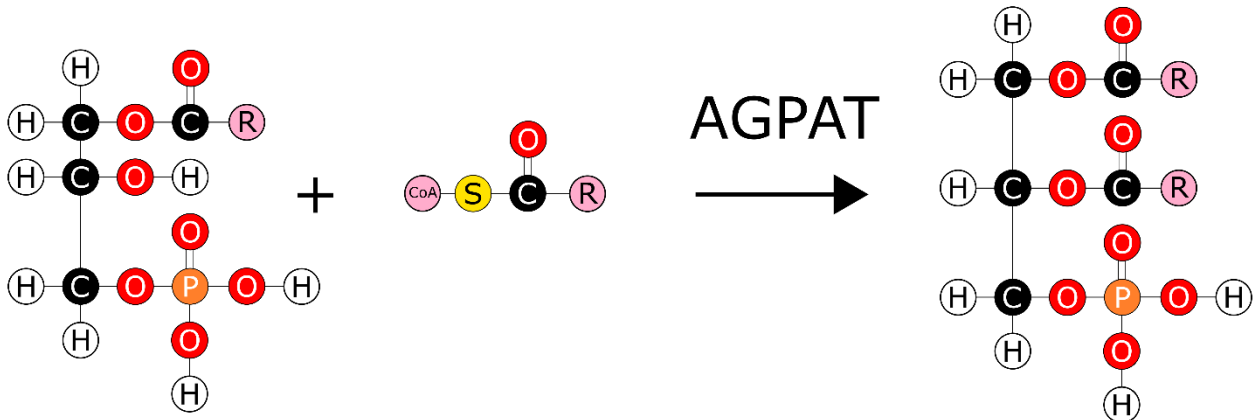


Figure 8. The second phase of triglyceride synthesis: in a chemical reaction catalyzed by AGPAT enzyme lysophosphatic acid and fatty-acyl-CoA are transferred into phosphatidic acid.

In the third phase (Figure 9) phosphatidic acid will either enter into synthesis of phospholipids or continue in the synthesis of triglycerides in which the phosphatidic acid is converted into diglyceride (intermediate 1,2-diacylglycerol). The reaction is catalyzed by phosphatidic acid phosphatase (PAP). [Ahmadian et al. 2007; Lehner and Kukis 1996]

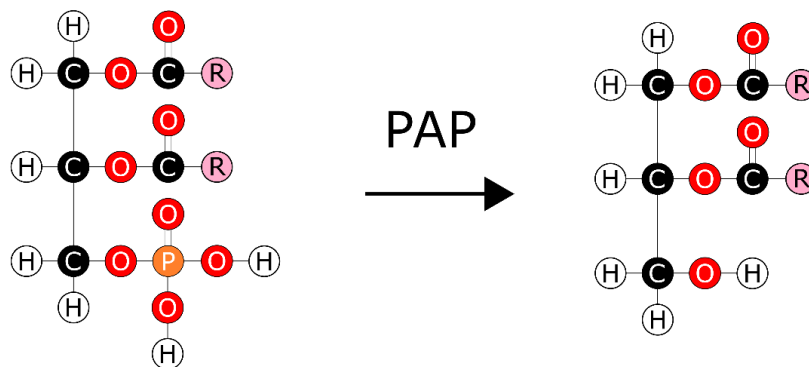


Figure 9. The third phase of triglyceride synthesis: in a chemical reaction catalyzed by PAP enzyme phosphatidic acid is converted into diglyceride.

In the fourth and final phase (Figure 10) of the triglyceride synthesis the diglyceride reacts with the final fatty-acyl-CoA with Diacylglycerol acyltransferase (DGAT) as a catalyst. The end product is triglyceride. [Ahmadian et al. 2007; Lehner and Kukis 1996]

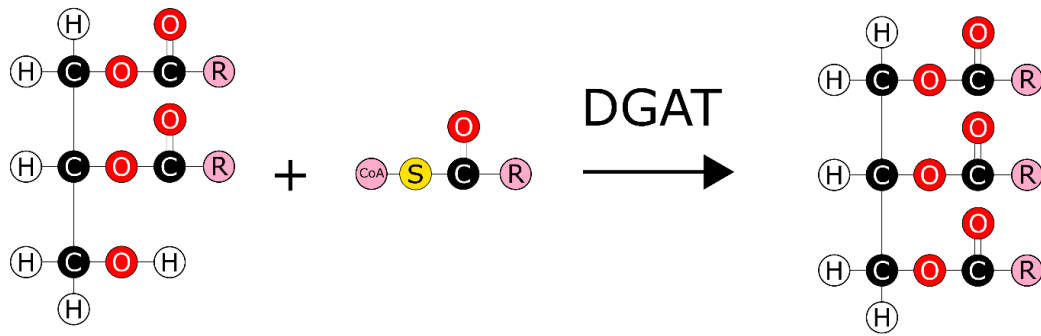


Figure 10. The final phase of triglyceride synthesis: in a chemical reaction catalyzed by DGAT enzyme diglyceride and fatty-acyl-CoA are transferred into triglyceride.

To make room for the stored triglycerides either the size of the existing adipocytes is increased or new adipocyte are created [Cinti2012]. Intra-abdominal adipose tissue starts to accumulate when storage capacity of subcutaneous adipose tissue is exceeded or it cannot generate new adipocytes due to genetic reasons or stress. [Ibrahim 2010] Over time storing excess energy can lead to a pathological condition called obesity which is characterized by a body-mass-index (BMI) equal to or over 30 kg/m². [Conway and Rene 2004]. Obesity and increased intra-abdominal fat are associated with high risk of metabolic disorders while the high amount of subcutaneous fat in thighs and hips has little or no association [Gesta et al. 2007]. Obesity also promotes the accumulation of triglycerides within the cells of non-adipose tissue such as muscle or liver that normally have a small triglyceride content. These deposits of triglycerides are called ectopic fat. [Lettner and Roden 2008]

When energy expenditure increases WAT starts a process called lipolysis (more generally hydrolysis, [Ahmadian et al. 2007]) in which it releases fatty acids and glycerol into the blood stream [Duncan et al. 2007]. Eventually the fatty acids are oxidized in tissues to provide energy while the glycerol is used mostly as a substrate for glucose production in the liver. [Ràfols 2014; Bolsoni-Lopes and Alonso-Vale 2015] Lipolysis is promoted by several hormones such as glucagon, epinephrine, cortisol and growth hormone whereas insulin decreases the activity of the process [Qaid and Abdelrahman 2016].

Chemically hydrolysis is defined as the splitting of an ester by water in the presence of a catalyst into alcohol and an acid [Beare-Rogers et al. 2001]. The hydrolysis of a triglyceride molecule occurs in three phases each of which is catalyzed by its own enzyme (Figure 11). First, triglyceride is split into diglyceride and a free fatty acid by an enzyme called the adipose triglyceride lipase (ATGL). In the next phase the hormone-sensitive lipase (HSL) enzyme catalyzes the hydrolysis of the diglyceride into a monoglyceride and a free fatty acid. Finally, the monoglyceride is hydrolyzed into glycerol and a free fatty acid by the monoglyceride lipase (MGL) enzyme.

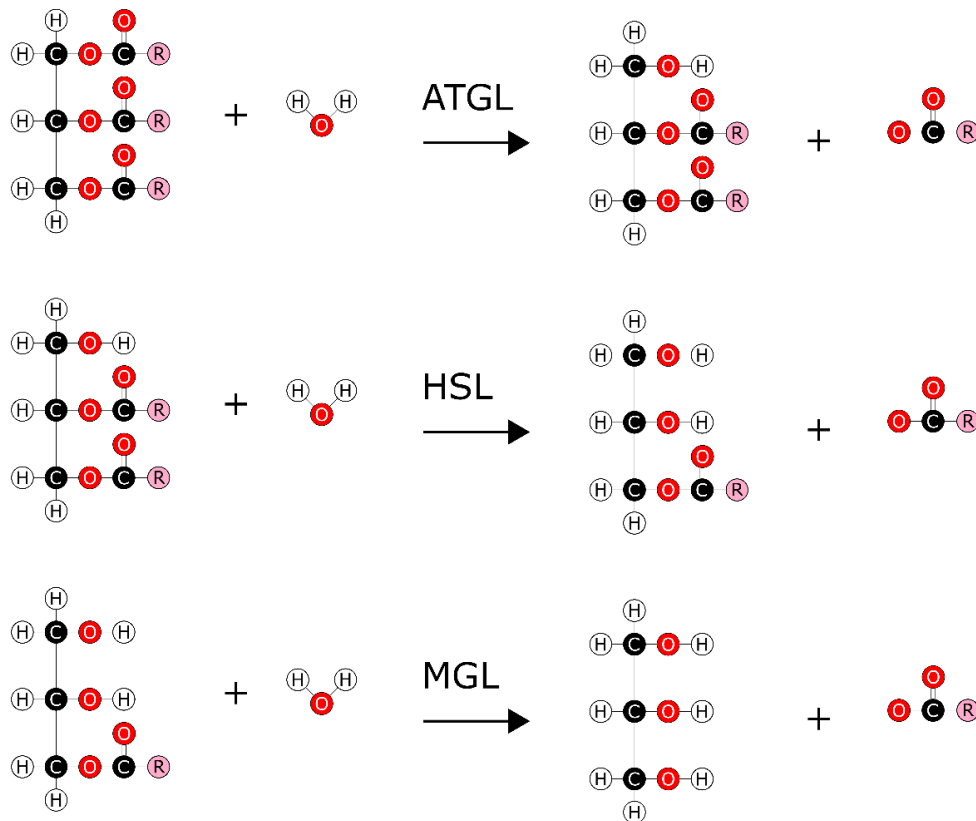


Figure 11. A triglyceride molecule is hydrolyzed in three phases each of which releases a free fatty acid. The enzymes catalyzing each phase are: adipose triglyceride lipase (ATGL), hormone-sensitive lipase (HSL) and monoglycerol lipase (MGL). Glycerol is released in the final phase.

2.4 Brown adipose tissue

Brown adipose tissue (BAT) was described already in 1551 by Conrad von Gesner [Gesner 1551] although its role as a thermogenic organ was not discovered until 1960s [Smith and Horwitz 1969]. It was known that human fetuses have BAT [Hatai 1902] but autopsy reports in 1970s and 1980s confirmed that it can also be found in adults [Heaton 1972] particularly in outdoor workers [Huttunen et al 1981]. Positron emission tomography (PET) imaging became a valuable tool for oncology during the 1990s. Especially useful was the Fluorine-18 fluorodeoxyglucose (¹⁸F-FDG) tracer which accumulates in various tumors and a few non-malignant tissues such as exercised muscle [Engel et al 1996; Yamada et al 1995]. Some groups reported symmetrical accumulations of ¹⁸F-FDG in the neck and paravertebral region of the thoracic spine [Barrington and Maisey 1996]. These were thought to be muscle tension until further studies aided by the hybrid PET/CT (computed tomography) proved that this kind of ¹⁸F-FDG uptake is in fact located in adipose tissue [Hany et al 2002; Cohade et al 2003a, 2003b]. In 2007 Nedergaard et al showed that this was BAT [Nedergaard et al 2007]. Two years later five independent groups – one of which was from Turku PET Centre – confirmed that cold activated BAT exists in human adults [Saito et al 2009; van Marken Lichtenbelt et al 2009; Virtanen et al 2009; Cypess et al. 2009; Zingaretti et al. 2009]. The two main functions of BAT are protection against cold

exposure by non-shivering thermogenesis and dissipation of excess energy from food [Calderon-Dominguez et al. 2016].

2.4.1 Brown adipose tissue distribution

Brown adipose tissue depots are located mainly in cervical and supraclavicular areas but smaller depots can also be found in the axillary, paraspinal, periaortic, perirenal, perihepatic and perisplenic areas (Figure 12) [Cypess et al. 2015]. Infants also have an interscapular BAT depot but it disappears when one reaches adulthood [Heaton 1972; Lindell 2013]. BAT is essential for newborns who lack the ability to produce heat by shivering. Therefore at birth BAT comprises up to 5% of body weight but its amount decreases as skeletal muscles develop during childhood. [Rogers 2015] In vivo imaging studies of human adults have reported BAT masses from 0.02 to 300 g [Cypess et al. 2009; Gerngroß et al. 2017; van Marken Lichtenbelt et al. 2009; Muzik et al. 2012; Orava et al. 2009]. Based on positron emission tomography (PET) studies it has been estimated that 50% of young adults (ages 20 – 35 years) have BAT while only 10% still have it after 40 years of age [Saito et al. 2009; Yoneshiro et al. 2011].

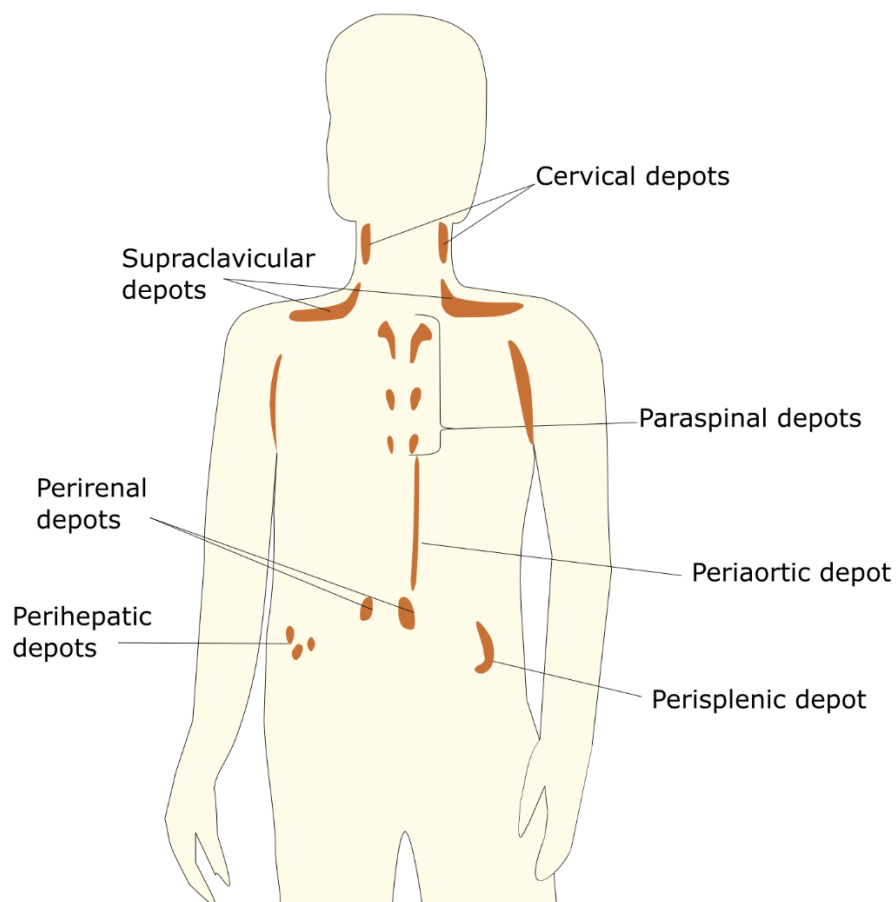


Figure 12. The sites where brown adipose tissue can be found in humans. Most frequently it exists in the cervical and supraclavicular depots.

2.4.2 Brown adipocyte appearance

In contrast to a white adipocyte, a brown adipocyte has multilocular lipid droplets and multiple large round mitochondria with transverse cristae (Figure 13). The brown color of BAT is provided by the mitochondria together with the tissue's dense vasculature. [Cypess 2009] Indeed, every brown adipocyte is surrounded by capillaries that provide oxygen and lipids. The activity of the cell is controlled by nerve fibers reaching each cell. [Cannon and Nedergaard 2004] The dense vasculature and multitude of mitochondria are thought to be the reason for the lower fraction of fat in BAT compared to WAT which is reported by several studies [Holstila et al. 2017; Franssens et al. 2017; Franz et al. 2015; Raiko and Holstila et al. 2015; Holstila et al. 2013].

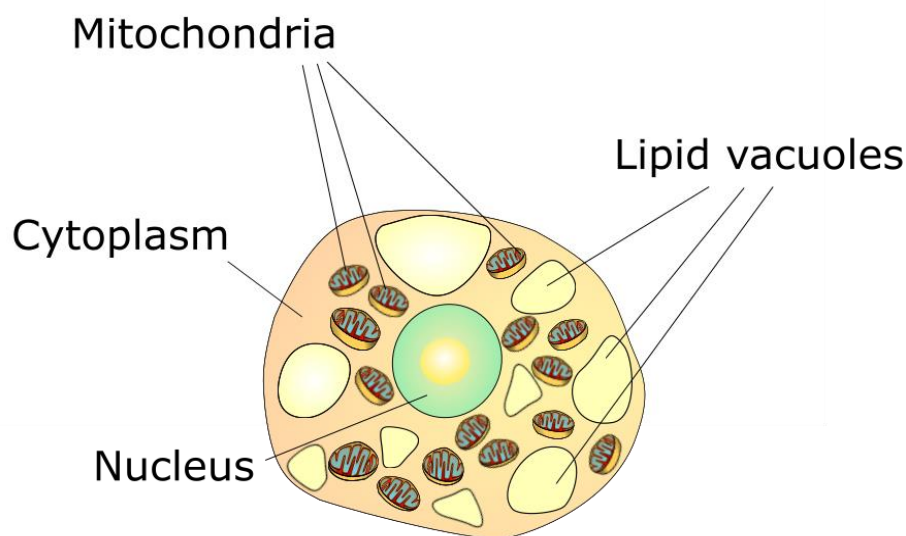


Figure 13. A brown adipocyte with some of the characteristic cell organs.

Brown adipocytes exist in two types: classic brown and beige or recruitable brown adipocytes. While classic BAT is located in the areas mentioned in the previous section the beige adipocytes exist also within white adipocytes [Calderon-Dominguez et al. 2016]. Evidence suggests that they have different embryotic origins: classic BAT shares a common origin with skeletal muscle cells, namely the progenitor cells of dermomyotome expressing the myogenic factor 5 (Myf5) [Seale et al 2008]. On the other hand, the origin of beige adipocytes is still under investigation. They may either originate from Myf5 negative progenitor cells like white adipocytes [Ishibashi and Seale 2010] or they may be converted from white adipocytes by reversible transdifferentiation [Cinti 2009]. It has been suggested that most of BAT in adult humans is beige [Wu et al. 2012; Sharp et al. 2012] but recent studies have shown that classic brown adipocytes of mice living in thermoneutral conditions (30°C) like humans resemble more human brown adipocytes than beige adipocytes in mice. Thus human BAT is not different in nature from classical mouse BAT. [Cannon et al. 2020] The author of this thesis is not aware of any previous research about the fatty acid characteristics of human BAT. However, several animal studies have reported that BAT has more saturated fatty acids [Hamilton et al. 2011; Strobel et al. 2001] and less polyunsaturated fatty acids than WAT [Strobel et al. 2001].

2.4.3 Thermogenesis in BAT

Thermogenesis (production of heat) occurs as a byproduct of metabolic activity in all tissues. All mammals have a specific thermoneutral zone which is a certain ambient temperature range within which the general metabolism produces enough heat to maintain the predetermined body temperature. Outside this zone the body temperature is maintained first by vasoconstriction and piloerection (goosebumps). If this is not enough, more energy consuming methods are employed. In shivering thermogenesis involuntary muscle contractions adenosine triphosphate (ATP) is hydrolyzed and heat is generated as a byproduct. [Cannon and Nedergaard 2011] In BAT the cellular respiratory chain is uncoupled from the production of ATP and heat is generated directly from the substrates that would normally be used for the ATP synthesis [Fedorenko et al. 2012].

In general, energy of cells is provided by oxidation of carbohydrates, lipids and proteins. The energy released from the oxidation is stored into high-energy bonds of adenosine diphosphate (ADP) and adenosine triphosphate (ATP) which is the primary energy “currency” of the cells readily available when energy is quickly needed [Bonora et al. 2012; Törnroth-Horsefield and Neutze 2008]. The production of ATP involves three steps: glycolysis, tricarboxylic acid cycle (TCA) and oxidative phosphorylation. In the first step the main energy source glucose is converted into pyruvate. Already low amount of ATP is produced at this stage. Next, pyruvate is converted into acetyl coenzyme A (acetyl-CoA) which can also be generated from lipids and proteins. Acetyl-CoA enters the mitochondria in the form of acyl-carnitine before being converted back to acetyl-CoA. Then it enters the TCA cycle and eventually reduced electron carrier nicotinamide adenine dinucleotide (NADH) is produced. Finally in the oxidative phosphorylation NADH is oxidized for generating a proton gradient through the inner mitochondrial membrane allowing the production of large amounts of ATP by mitochondrial ATP synthase. [Bonora et al. 2012; Saponaro et al. 2015]

In brown adipocytes the energy acquired from the oxidation of substrates is uncoupled from the ATP synthesis by an uncoupling protein UCP-1 which is unique to brown adipocytes. The process begins when the brain activates the sympathetic nerves reaching each brown adipocyte. From the nerve endings the neurotransmitter norepinephrine is released which then binds to β_3 receptors. These receptors exist only in brown and white adipose tissue. The β_3 activation triggers the production of cyclic adenosine monophosphate (cAMP) which in turn activates the protein kinase A (pKA). Finally the pKA induces the hydrolysis of the stored triglycerides which act both as activators of UCP-1 and fuel for the thermogenesis. After the UCP-1 activation the hydrolyzed triglycerides are converted into acetyl-CoA which enter the mitochondria in the form of acyl-carnitine and are converted back to acetyl-CoA and enter the TCA cycle just like in the ATP synthesis. However the proton gradient through the inner membrane of the mitochondrion does not lead to the production of ATP but is discharged as heat. [Cannon and Nedergaard 2004]

2.4.4 Uptake of fatty acids and other substrates in BAT

BAT is metabolically very active tissue. Cold exposure is the most effective activator of BAT although others, for example dietary activators exist as well. Some of the most interesting are capsinoids, which can be found in chili peppers [Osuna-Prieto et al 2018]. The activation of BAT increases perfusion in the tissue providing it with more oxygen and nutrients but also transferring the generated heat to other parts of the body [Orava et al 2011]. Activation increases glucose uptake of the tissue up to 12-fold and it is assumed to represent the thermogenic activity of BAT [Virtanen et al 2009; Orava et al. 2011; Muzik et al. 2013]. In vitro studies on animal and human brown adipocytes suggest that the glucose is used for glycerol-3 production in the triglyceride synthesis [Moura et al. 2005; Laplante et al. 2008; Barquissau et al. 2016].

As stated in the previous section hydrolysis of the stored triglycerides in the brown adipocyte are essential for the activation of the UCP-1 protein and the thermogenesis. Namely, studies performed on rats and humans showed that by blocking the intracellular lipolysis the thermogenesis is considerably suppressed [Blondin et al. 2017a; Labbé et al. 2015]. Other studies however suggest that thermogenesis can still be initiated if lipolysis is taking place in WAT or the fatty acids are provided by blood circulation [Schreiber et al. 2017; Shin et al. 2017]. Indeed, BAT seems to uptake fatty acids only after the intracellular triglyceride stores are depleted [Hoeke et al. 2016]. These circulatory fatty acids are utilized either from free fatty acids in plasma or lipoproteins [Berbée et al. 2015; Blondin et al. 2017a; Khedoe et al. 2015]. The fatty acid uptake is also accompanied by de novo lipogenesis [Hoeke et al. 2016; Schreiber et al. 2017]. A previous study indicates that both saturated and unsaturated fatty acids used during cold exposure not only in BAT but also WAT [Lu et al. 2016].

2.5 Non-invasive methods for studying brown adipose tissue

There are multiple methods which provide a non-invasive scope into BAT detection or study of its function. They can be divided into methods using and not using ionizing radiation. The former includes nuclear imaging and computed tomography (CT) both of which had a key role in the original detection of functioning BAT in adult humans [Hany et al 2002; Cohade et al 2003a, 2003b]. Still ¹⁸F-FDG PET/CT hybrid imaging is considered as the golden standard for in vivo BAT localization. However, the health risk involved with ionizing radiation [Hall et al. 2017] has directed research into finding radiation-free methods for BAT research. In this field MRI with its numerous sub-methods is a very promising and widely used but also an expensive modality [Wu et al. 2020]. Some studies have experimented on more affordable methods such as ultrasound, thermal imaging and near-infrared spectroscopy [Chondronikola et al. 2017]. The next sections will give an insight into some of the methods for BAT research. The main topic of this thesis, magnetic resonance, is covered in greater detail.

2.5.1 Positron emission tomography

Positron emission tomography (PET) is a nuclear imaging method in which proton rich nuclei are administered into study subjects. The nuclei remove the excess protons by either electron capture or positron emission which is more prevalent in lower-weight nuclei. The emitted antimatter electron called positron travels a short distance in the medium losing energy until it combines with an electron. Then they form a short-lived positronium particle or annihilate. Either way, two 511 keV photons are emitted in approximately opposite directions from each other (Figure 14). If these photons are detected by opposite PET detectors within a narrow time frame it is registered as a coincidence event. The annihilation is assumed to have taken place on a line between the two detectors which is called the line of response. When millions of lines are recorded the spatial distribution of annihilations can be estimated. [Basu et al. 2011] If the exact arrival times of the photons are taken into account the point of the annihilation on a line of response can be estimated and thus the precision of the imaging is improved. [Chondronicola et al. 2017] Various positron emitters are used in PET imaging including ^{11}C , ^{13}N , ^{15}O and ^{18}F which is the most commonly used. They differ by their half-life and positron energy which contributes to the distance which the positron travels in the medium before combining with an electron. The half-life ranges typically from few minutes (half-life of ^{15}O 2 min) to less than two hours (half-life of ^{18}F 110 min) requiring the nuclei to be produced in a cyclotron close to the imaging site making the cost of a PET facility very high. [Basu et al. 2011] The positron emitting nuclei have to be attached to ligands which interact with the biology of the study subject in a desired way. Together the positron emitter and the ligand form a PET radiopharmaceutical, or more commonly a PET tracer. [Wadsak and Mitterhauser 2010]

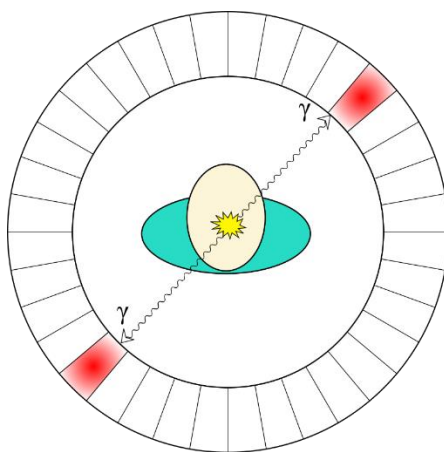


Figure 14. A simplified principle of the PET imaging: Annihilation of a positron and an electron create two 511 keV gamma quanta which are directed away from the annihilation site in almost opposite directions. When the gamma quanta are detected at two opposite detectors the line on which the annihilation occurred can be calculated. The calculation is improved if the arrival time of the gamma quanta is taken into account. Thus the actual annihilation site can be estimated.

The most common PET tracer is ^{18}F -flourodeoxyglucose (FDG) which acts as a glucose analog in the body. An activated brown adipocyte takes up ^{18}F -FDG among plasma glucose, phosphorylates it but cannot metabolize it further. Thus ^{18}F -FDG gets trapped inside the cell and visualizes activated BAT in PET imaging.

[Chondronicola et al. 2017] Another useful tracer for BAT research is 14-(*R,S*)-[¹⁸F]Fluoro-6-thiaheptadecanoic acid (FTHA) which acts like a fatty acid. It goes through oxidation but binds to mitochondrial proteins allowing the PET imaging of the uptake. [Bauwens et al. 2014] Fatty acid oxidation of BAT can also be studied with ¹¹C-acetate which is a fatty acid. However the half-life of ¹¹C is very short (20 min) and the metabolic fate of acetate in the cell is only based on assumptions. [Chondronicola et al. 2017] Blood perfusion can be studied using ¹⁵O-H₂O which has been shown to increase in BAT during cold exposure [Orava et al. 2011]. It can also provide an insight into the oxygen consumption of the tissue [U Din et al. 2016].

2.5.2 Single-photon emission imaging

Unlike PET, single photon emission tomography uses tracers that emit only one photon at a time, just as the name of the modality suggests. It can be performed in either 2-dimensional planar mode or 3-dimensional single-photon emission computed tomography (SPECT) mode (Figure 15). Quantification and resolution of single-photon emission imaging is inferior to PET but the tracers have considerable longer half-life and can thus be used without a production facility in close proximity. [Ljungberg 2018; Jaszcak et al. 1980]

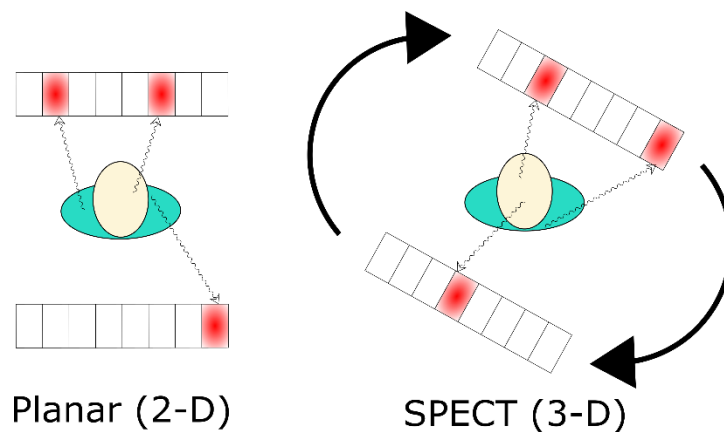


Figure 15 Simplified principles of two imaging modes of single photon emission imaging. In planar mode the detectors are kept at constant positions over and under the subject providing 2-dimensional projections of the distribution of the photon emitters inside the subject. In SPECT mode (single photon emission computed tomography) the detectors are rotated around the subject and a 3-dimensional image of the photon emitter distribution is reconstructed.

A few single-photon emitting tracers have been used for BAT research. ¹²³I-*meta*-Iodobenzylguanidine (MIBG) is a norepinephrine analog and clinically used for cardiac studies. It has been shown that MIBG uptake increases during cold exposure [Baba et al. 2007] and it correlates with ¹⁸F-FDG uptake [Admiraal et al. 2013]. In addition lipophilic tracers ^{99m}Tc-Methylisobutylisonitrile (MIBI) and ^{99m}Tc-Tetrofosmin have been used for BAT studies as they bind to tissues with high mitochondrial density [Cypess et al. 2013; Fukuchi et al. 2003].

2.5.3 Computed tomography

Computed tomography (CT) is based on measuring attenuation of x-ray in the study subject. The scanning procedure is usually performed by moving a subject through a rotating beam of x-ray and continuously recording the x-ray passing through the subject. [Kalender 2006] The x-ray attenuation coefficient of the tissue is referred to as radiodensity and measured in Hounsfield units (HU) [Chen et al. 2016]. The recorded x-ray data is then reconstructed into 3-dimensional image of the attenuation within the subject (Figure 16). [Kalender 2006] CT is commonly used in combination with PET and SPECT imaging to provide attenuation correction increasing the precision of the nuclear imaging methods and also providing anatomical information [Basu et al. 2011].

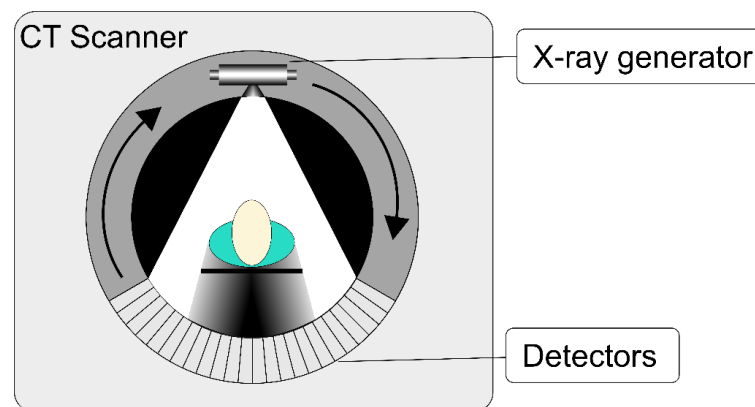


Figure 16. A simplified principle of computed tomography (CT). A subject is moved through a rotating x-ray beam and a volumetric image of the x-ray attenuation is produced afterwards. Figure adapted and modified from [Raiko et al. 2020]

Radiodensity of BAT has been shown to correlate with ^{18}F -FDG uptake and it is higher than the radiodensity of WAT. It has also been shown to increase during cold exposure [Baba et al. 2010] and correlate with other metabolic parameters [U Din et al. 2017].

2.5.4 Ultrasound

Ultrasound imaging utilizes mechanical waves which are transmitted into tissue with piezoelectric crystals. The time from the transmission to the return of the reflected echo correlates to the depth of the reflected objects (Figure 17). The intensity of the echo depends on the difference of the acoustic impedances between different media. [Carovac et al. 2011] Using contrast-enhanced ultrasound the perfusion of BAT has been shown to increase during cold exposure [Flynn et al. 2015].

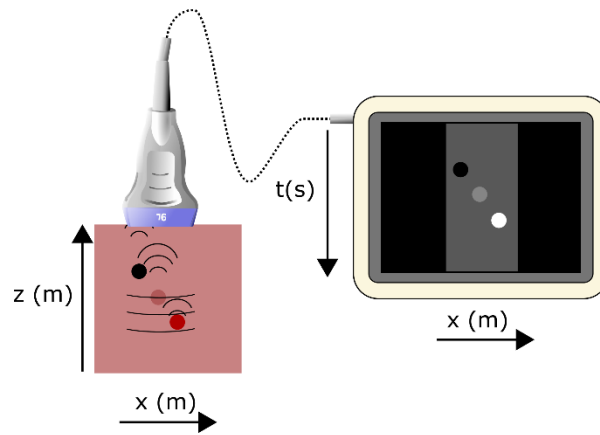


Figure 17. A schematic representation of ultrasound imaging. Pulsed sound waves are transmitted into tissue and the arrival time of returning echoes are recorded. Time of the echo arrival correlates to the depth of the sound reflecting object.

2.5.5 Near-infrared spectroscopy

Near-infrared spectroscopy (NIRS) is based on transmitting near-infrared light into tissue and detecting the changes in the spectrum of the reflected light (Figure 18). It is sensitive to the detection of hemoglobin oxygenation. NIRS has been used to show an increased oxygen consumption in BAT compared to skeletal muscle during cold exposure [Muzik et al. 2013] and also a correlation has been found between BAT hemoglobin concentration and ^{18}F -FDG uptake in supraclavicular BAT [Nirengi et al. 2015].

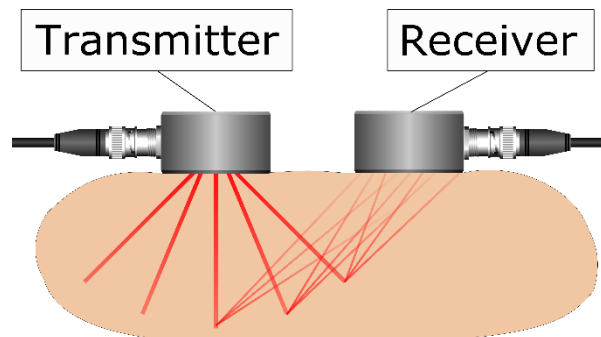


Figure 18. The working principle of near-infrared spectroscopy (NIRS). Near-infrared light is transmitted into tissue and reflected light is detected by a receiver. Changes in the spectrum of the light are analyzed. Figure adapted from [Raiko et al. 2020].

2.5.6 Photoacoustic imaging

In photoacoustic (or optoacoustic) imaging laser light is transmitted into tissue. The light is absorbed by an optically absorbing substance such as hemoglobin. This causes a local temperature rise which in turn creates a pressure wave which can be detected with an ultrasonic receiver (Figure 19). [Liu et al. 2018] BAT has been studied using multispectral optoacoustic tomography (MSOT) which was able to detect BAT activation by observing the change in hemoglobin signal [Reber et al. 2018].

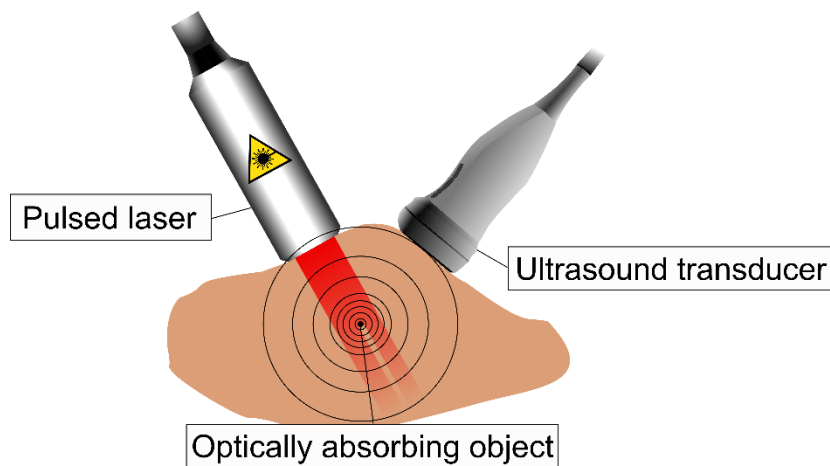


Figure 19. The principle of photoacoustic sensing: Pulsed laser is absorbed by an optically absorbing object, for example hemoglobin, which causes a local pressure rise and an ultrasonic mechanical wave which can be detected at the surface. Figure adapted from [Raiko et al. 2020].

2.5.7 Thermal imaging and thermal probes

Measuring skin temperature with either thermal cameras or probes is an affordable way of conducting BAT research. Therefore several studies utilizing these methods have been published and many interpret the change in supraclavicular skin temperature as an activation of BAT [Symonds et al. 2012; Ang et al. 2017; Zhou et al. 2018]. However, the insulating effect of subcutaneous adipose tissue and the other heat producing organs in close proximity make the method prone to errors [Sarasniemi et al. 2018].

2.5.8 Magnetic resonance methods

Magnetic resonance imaging (MRI) and spectroscopy (MRS) are based on a physical phenomenon called nuclear magnetic resonance (NMR). It was first discovered by the group of Isidor Isaac Rabi who reported the absorption of radiofrequency (RF) energy on a molecular beam of lithium chloride passing through a vacuum chamber and a magnetic field in 1938 [Rabi et al. 1938]. In 1944 Rabi was awarded the Physics Nobel prize for his work. In 1946 two independent research groups lead by Felix Bloch and Edward Mills Purcell reported NMR measurements of solid material for which they were awarded the Nobel Physics prize in 1952 [Bloch et al. 1946; Purcell et al. 1946]. NMR spectroscopy developed remarkably in 1957 when Lowe and Nordberg showed that the NMR signal could be turned into a spectrum using Fourier transformation which allowed the study of complex NMR signals [Lowe and Nordberg 1957]. The process was made more convenient in 1966 by Ernst and Anderson who published a study about using a computer to perform the Fourier transformation [Ernst and Anderson 1966]. Ernst received a Nobel prize in physics for his contribution to the development of NMR spectroscopy in 1991. In 1973 Lauterbur published an article in which he described that by tuning the magnetic field gradients in a NMR spectrometer he could acquire projections of his sample and reconstruct them into two-dimensional images thus he had invented zeugmatography which would later be called magnetic

resonance imaging (MRI). [Lauterbur 1973] He shared the 2003 Nobel prize in medicine with Mansfield who had developed magnetic field gradient based slice selection method [Garroway et al. 1974] and pulse sequences for fast image acquisition [Mansfield and Maudsley 1977]. Clinical applications of NMR usually leave the word “nuclear” out of the modality name to avoid misconception with methods utilizing ionizing radiation such as nuclear medicine [van der Graaf 2010].

BAT has multiple characteristics which can be used for differentiating it from WAT using magnetic resonance methods. One of the most utilized is the lower fat fraction of BAT compared to WAT [Wu et al. 2020]. This has been shown in both MRS [Koskensalo et al. 2017; Raiko and Holstila et al. 2015] and MRI studies [Holstila et al. 2017; Franz et al. 2015; Lundström et al. 2015; Holstila et al. 2013]

The depletion of fatty acids during activation of BAT decreases the fat fraction even more [Gifford et al. 2016; Oreskovich et al. 2019]. However, this has not been observed in all studies [Holstila et al. 2017; Ong et al. 2018].

Magnetic susceptibility (the measure of how much a material becomes magnetized in a magnetic field [Plewes and Kucharczyk 2012]) is altered by the numerous mitochondria of BAT containing iron on their inner membrane and also the fat-water interfaces on the lipid droplets which appears as a reduction in the T2 and T2* times in several studies [Hu et al. 2013; Holstila et al 2017; Lundström et al. 2015].

Diffusion of water is restricted through the inner mitochondria wall [Wu et al. 2020]. Water-based diffusion weighted imaging (DWI) of BAT has been performed in some studies [Deng et al. 2015; Dieckmeyer et al. 2017]. Diffusion weighted MRS offers an interesting insight into the lipid droplet size in the cells [Verma et al. 2017].

Activation of BAT increases the perfusion and oxygen consumption which affect several MR parameters [Wu et al. 2020]. The increased perfusion can be detected using contrast media [Sbarbati et al. 2006; Yalingar et al. 2019] and arterial spin labeling technique [Dai et al. 2015]. The oxygenation of BAT decreases during activation and thus the T2* time decreases too [Khanna and Branca 2012; Simhick et al. 2017]

Temperature affects the resonance frequency of water. Thus detecting the frequency difference between lipids and water might be used as an indicator of BAT activation [Koskensalo et al. 2017].

2.6 Proton NMR physics and techniques

The next sections cover the basics physics of nuclear magnetic resonance as well as the relevant imaging and spectroscopic methods of BAT. Finally, the quantitative parameters of lipid magnetic resonance spectroscopy are introduced.

2.6.1 Nuclear magnetic resonance

Spin is an intrinsic angular momentum vector \mathbf{I} which is possessed by protons, neutrons and electrons. If a nucleus has odd number of protons and neutrons it has a non-zero spin quantum number. This is the case for hydrogen atom which consists of a single proton, thus it has a spin quantum number of 1/2. With respect to a given direction, such as the direction of an external magnetic field, the orientation of the proton angular momentum can have only two values. [Gibby 2005] Hence, the magnitude of the angular momentum \mathbf{I} can only have discrete values due to quantum mechanics. The values are given by the following equation:

$$|\mathbf{I}| = \hbar\sqrt{I(I + 1)}, \quad (1)$$

where \hbar is the reduced Planck's constant ($1.054571817 \times 10^{-34}$ Js). For proton this gives a magnitude of $\hbar\sqrt{3/4}$. In an external magnetic field \mathbf{B}_0 the component of angular momentum I_z which is parallel to the external field can have values given by the following equation:

$$I_z = m\hbar, \quad (2)$$

where m is the magnetic quantum number. It can have values $(-I, -I+1, \dots, I-1, I)$ and is thus limited to $2I+1$ different possible values. [Gupta et al. 2015] Hence, for proton the I_z can have only two values: $-\hbar/2$ and $\hbar/2$. As the values for $|\mathbf{I}|$ and I_z of proton are known the angle θ between $\boldsymbol{\mu}$ and \mathbf{B}_0 can be calculated:

$$\sin \theta = \frac{I_z}{|\mathbf{I}|} = \frac{\pm\hbar/2}{\hbar\sqrt{3/4}} \quad (3)$$

$$\Rightarrow \theta \approx \pm 35.26^\circ \quad (4)$$

Figure 20 illustrates a proton in an external magnetic field with the two possible orientations. [Gibby 2005]

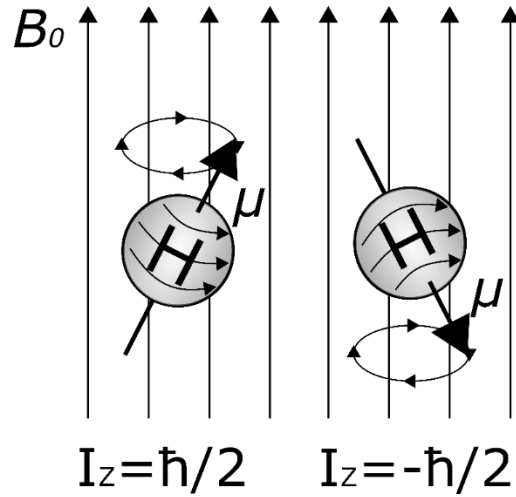


Figure 20. The precession of a magnetic momentum vector of a proton in an external magnetic field with the two possible orientations.

Proton also has a positive charge, and as a moving charge creates a magnetic field, proton is a magnetic dipole. [Gibby 2005] The relationship between the magnetic momentum vector μ and the angular momentum I is given by the following equation:

$$\mu = \gamma I, \quad (5)$$

where γ is the gyromagnetic ratio. An external magnetic field B_0 creates a torque T on the magnetic momentum μ . The magnitude of the torque is given by the following equation:

$$T = \mu \times B_0, \quad (6)$$

which gives rise to the potential energy:

$$E = -\mu \cdot B_0. \quad (7)$$

The potential energy achieves minimum value when the angle θ between μ and B_0 is zero, i.e. when they are parallel and $\theta = 0^\circ$. [Dixon and Ekstrand 1982] In this situation the equation (7) becomes:

$$E = -\mu_z B_0, \quad (8)$$

where μ_z is the magnitude of the magnetic dipole in the orientation of the B_0 field. When this is combined with equations (2) and (5) the relation in equation (8) can be written as:

$$E = -\gamma m \hbar B_0, \quad (9)$$

which represents the potential energy at different spin orientations. The energy difference between the two spin orientations of hydrogen atom is thus:

$$\Delta E = -\gamma m_2 \hbar B_0 - (-\gamma m_1 \hbar B_0) = \gamma \Delta m \hbar B_0. \quad (10)$$

As for proton $\Delta m = 1/2 - (-1/2) = 1$ and generally $\Delta E = \hbar\omega$ the equation (10) can be written as:

$$\omega = \gamma B_0. \quad (11)$$

which is called the Larmor equation. ω represents the frequency at which the angular momentum precesses around the vector B_0 and it is also the frequency at which it is possible to induce transitions between two energy states. [Dixon and Ekstrand 1982]

2.6.2 Chemical shift

The Larmor frequency varies between different chemical environments. This is because the electrons around nuclei cause a small magnetic field opposing the main magnetic field making the local magnetic field smaller. [Mlynárik 2017] This phenomenon is called shielding and its effect on local magnetic field B_{loc} can be described by the following equation:

$$B_{loc} = (1 - \sigma)B_0, \quad (12)$$

where σ is the shielding constant [Buckingham 1960]. The effect of shielding on a Larmor frequency f is called the chemical shift (denoted with δ) in it is usually expressed as a relation to a reference frequency f_{ref} as follows:

$$\delta = (f - f_{ref})/f_{ref}. \quad (13)$$

The chemical shift is characteristic of specific structural fragments of organic compounds and can thus be used to identify compounds by their Larmor frequencies. [Mlynárik 2017] Temperature has also an effect on the Larmor frequency. For example when Brownian motion of water molecules increases the hydrogen bonding between the molecules start to bend, stretch and break. Thus the water protons spend less time in hydrogen-bonded state and become more influenced by the shielding effect of the electrons circling the large oxygen atom and thus their local magnetic field and Larmor frequency is reduced (Figure 21). [Quesson et al. 2000]

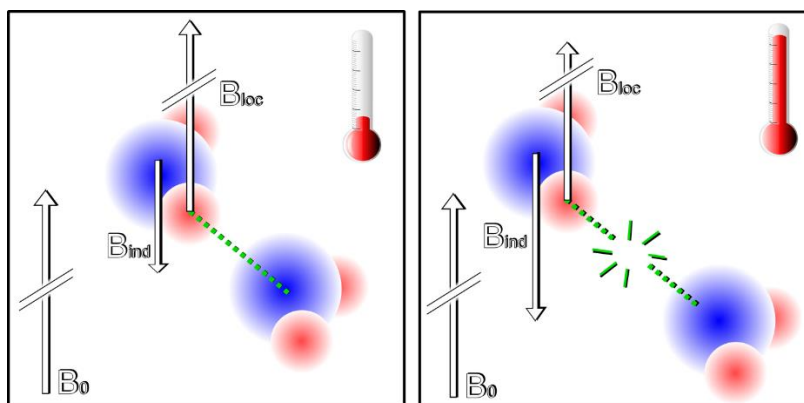


Figure 21. A hydrogen atom in a water molecule is influenced by the shielding effect of the electrons surrounding an oxygen nucleus. The effect is reduced by the hydrogen bonding between neighboring water molecules. However, when the temperature increases the Brownian motion increases and the hydrogen bonds bend stretch and break. This causes the hydrogen atom to be more influenced by the shielding of the electrons of the oxygen atom. The B_{ind} depicts the magnitude of the magnetic field induced by the electrons of the oxygen atom experienced by the hydrogen nucleus. B_{loc} is the local magnetic field experienced by the hydrogen nucleus. B_0 is the external magnetic field. Adapted from [Raiko et al. 2020].

2.6.3 J-coupling

As discussed in the chapter 2.6.2, the chemical environment affects the local magnetic field a nucleus experiences. In addition, the neighboring nuclei affect each other's magnetic field as the magnetic momenta can be at either parallel to or against the external field causing a splitting of spectral lines. This interaction gives rise to the splitting of the Larmor frequencies and is called the J coupling. It does not happen through open space between any nuclei because of molecular motion but chemical bonds mediate the effect between the nuclei which are parts of the same molecule. [Mlynárik 2017]

The number of neighboring nuclei affects the splitting pattern: for example in ethanol ($\text{CH}_3\text{CH}_2\text{OH}$, see Figure 22) the signal of CH_3 is affected by the neighboring CH_2 molecule in which there are two protons with two possible orientations of magnetic momenta: one with both parallel to the external field and one with both against the external field. One causes a downshift in the Larmor frequency and the other upshift. There are two possible combinations in which the other is parallel to the external field and the other one is against. However the effect of these combinations is the same and it does not change the Larmor frequency. Thus the magnetic momenta of CH_2 make the signal of CH_3 split into three different Larmor frequencies. However, the magnitude at the middle frequency is twice as high as the two others as there are two possible combinations which cause the central frequency. [Rhodes 2017]

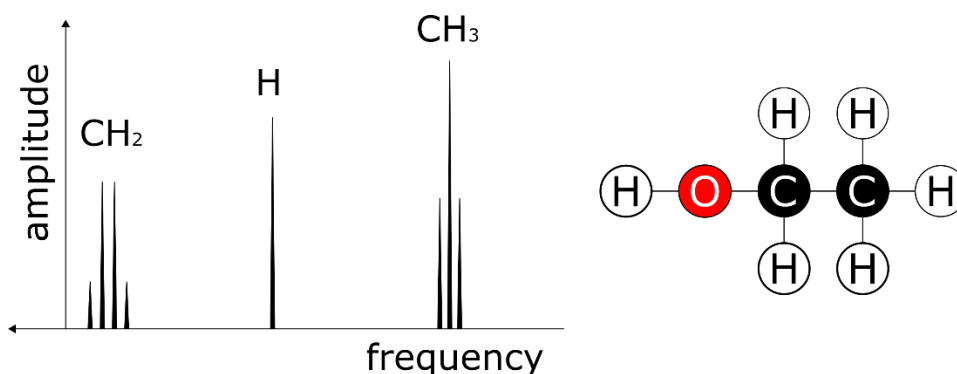


Figure 22. An NMR spectrum of ethanol. The integrals of the peaks are proportional to the signal amplitude which in turn is proportional to the number of nuclei transmitting the signal. For example if here the integral of H peak is 1 (arbitrary units) the amplitudes of CH₂ and CH₃ are 2 and 3 respectively. The splitting of the signals results from J-coupling of neighboring spins.

2.6.4 Macroscopic magnetization

The net effect of a large number of nuclear magnetic moments gives rise to a macroscopic magnetization M which is the vector sum of all the individual magnetic moment vectors (Figure 23). It is aligned with the external magnetic field B_0 .

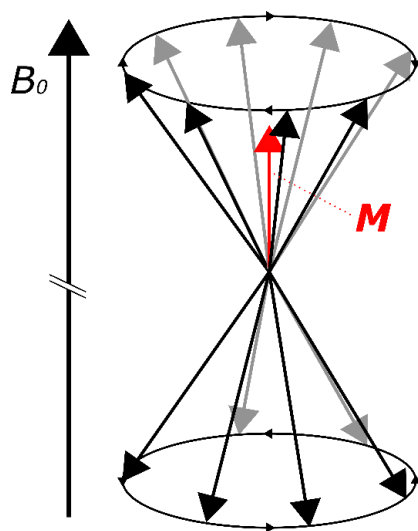


Figure 23. The net magnetization vector M (red arrow) is the vector sum of individual magnetization components. Although not quantum mechanically correct [Hanson 2008] it can be comprehended as in this figure.

The magnitude of the net magnetization depends on how the individual spins are distributed on either $+1/2$ or $-1/2$ states. It is affected by temperature and given by the Boltzmann distribution:

$$\frac{N_+}{N_-} = e^{-\frac{\Delta E}{kT}} \approx 1 + \frac{\hbar\gamma B}{kT}, \quad (14)$$

where k is the Boltzmann's constant ($1.38066 \times 10^{-23} \text{ JK}^{-1}$), T is the absolute temperature. The approximation is given by Taylor's expansion. For hydrogen ($\gamma = 2.6751978 \times 10^8 \text{ s}^{-1} \text{ T}^{-1}$) in field strength of 3 T and room temperature (298.15 K) the N_+/N_- ratio is 1.00002, i.e. only 2 more nuclei are on the +1/2 state compared to 100000 on -1/2 state. [Gibby 2005]

The interaction between the magnetization \mathbf{M} and the external magnetic field \mathbf{B}_0 can be described using classical electrodynamics:

$$\frac{d\mathbf{M}}{dt} = -\gamma \mathbf{M} \times \mathbf{B}_0 = -\mathbf{M} \times \boldsymbol{\omega}, \quad (15)$$

where t is time. When then angle between the magnetization and external magnetic field is zero, i.e. when they are aligned, \mathbf{M} is stationary. When the angle is non-zero the magnetization precesses about the \mathbf{B}_0 vector at the angular frequency ω (Figure 24). [Mlynárik 2017]

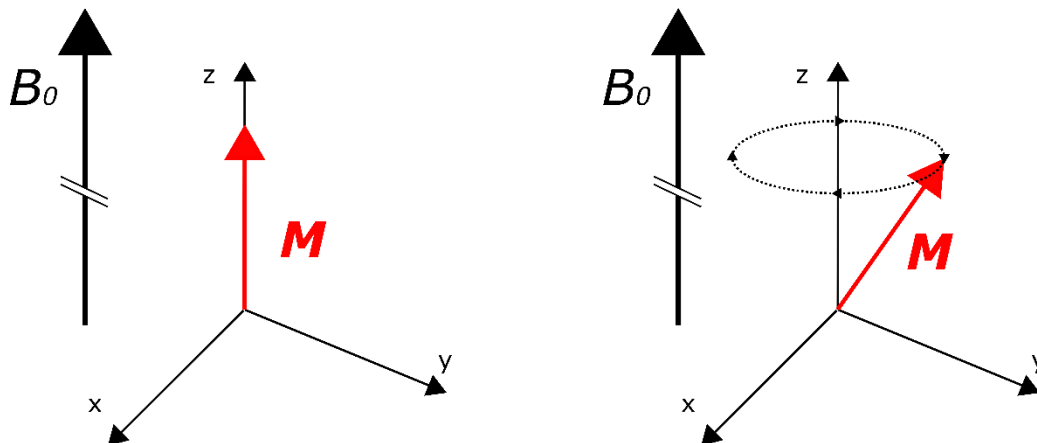


Figure 24. The net magnetization vector keeps stationary when it is aligned with the external magnetic field. If the angle between the magnetization and the external magnetic field is non-zero the magnetization precesses around the direction of the external field vector.

The orientation of the magnetization vector can be manipulated by applying radiofrequency (RF) energy at a certain direction and frequency, i.e. the Larmor frequency. If the RF field is applied perpendicular to the external field direction the magnetization starts to precess around the magnetic field component \mathbf{B}_1 of the RF field. This is visualized in Figure 25 where the coordinate system is changed from laboratory (x, y, z) to rotating frame (x', y', z), i.e. the coordinates x' and y' rotate at the Larmor frequency and the magnetization precessing around the external field direction is stationary in the rotating frame coordinate system although the angle between the magnetization and the external field is non-zero. Likewise, the magnetic field component \mathbf{B}_1 of the RF field is stationary in the rotating frame system although it rotates in the laboratory coordinate system. [Mlynárik 2017]

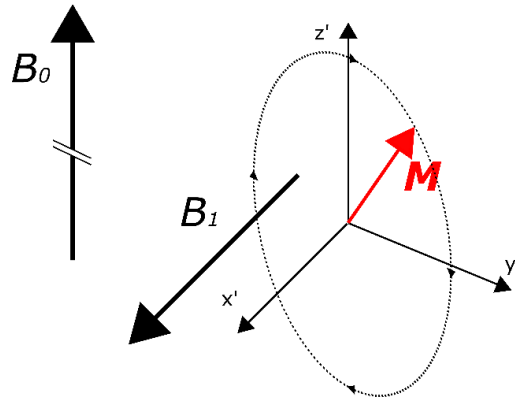


Figure 25. When an RF field is applied in the x' direction in the rotating frame coordinate system, the magnetization \mathbf{M} starts to precess around the axis which is parallel to the magnetic component \mathbf{B}_1 of the RF field.

The RF field is used for flipping the magnetization to make it precess around the external magnetic field vector in the xy -plane. The precessing magnetization can be detected using a coil into which the magnetization induces a current according to Faraday's law. This is the NMR signal which is called the free induction decay (FID). Maximum signal amplitude is acquired after a flip angle of 90° . [Mlynárik 2017]

2.6.5 T1 relaxation

The NMR signal decays as the magnetization \mathbf{M} does not stay precessing in the x, y -plane forever but starts to align itself back towards the external magnetic field direction due to relaxation effects. The recovery of the magnetization in z -direction is called longitudinal relaxation and it is characterized by the following equation:

$$\mathbf{M}_z(t) = \mathbf{M}_0(1 - e^{-t/T_1}), \quad (16)$$

where \mathbf{M}_z is the component of the magnetization vector that is parallel to the external magnetic field, t is time and T_1 is the relaxation time constant. In the longitudinal relaxation the individual spins are transferred from higher to lower energy state. These transitions are stimulated by molecular motion which give rise to fluctuating magnetic fields within the medium. These fluctuating fields are caused by several mechanisms, one of them being the dipole-dipole interactions between individual nuclei. In the dipole-dipole interaction a nucleus with magnetic momentum can produce a magnetic field on its neighboring nucleus. The amplitude of the field is μ/r where r is the distance between the nuclei. The frequency components which are close to the Larmor frequency in the fluctuating fields stimulate transitions from higher energy state to lower. The released energy is transferred to thermal energy of the medium. Hence the longitudinal relaxation time is also called the spin-lattice relaxation time. [Dixon and Ekstrand 1982]

2.6.6 T2 relaxation

Another relaxation mechanism happens due to the loss of phase coherence of the individual magnetic moments. The reason is that the local magnetic field experienced by the nuclei is not uniform throughout the medium. As the Larmor frequency depends on the magnetic field, nuclei at different parts of the medium start to precess at different frequencies and the phase coherence giving rise to the macroscopic magnetization is lost. This is called the spin-spin dephasing as the spins come out of phase with one another. [Gibby 2005] Usually this is much shorter process than the T1 relaxation. [Plewes and Kucharczyk 2012]

If the phase coherence is lost due to a static magnetic field which vary in intensity over space the phase coherence can be recovered by applying an RF pulse which flips the magnetization around and makes the phase of the spins recover creating a signal which is called an echo – in this case a spin echo. This kind of RF pulse is called a 180° pulse and its effect on the magnetization is called refocusing. Although the effect of the static magnetic fields is thus reversed the effect of the fluctuating magnetic fields within the space cannot be reversed by the refocusing pulse. The relaxation time caused by the fluctuating magnetic fields is called the T2 relaxation time. The sum effect of the static and fluctuating magnetic field inhomogenities is called the T2* time. [Gibby 2005] Figure 26 shows hypothetical T2 and T2* relaxation effects on a free induction decay signal which is refocused at every 100 ms. This kind of pulse sequence is called spin-echo. The amplitude of the T2 signal decay over time $A(t)$ is characterized by the following equation:

$$A(t) = A_0 e^{-t/T_2}, \quad (17)$$

where A_0 is the initial signal amplitude. [Dixon and Ekstrand 1982]

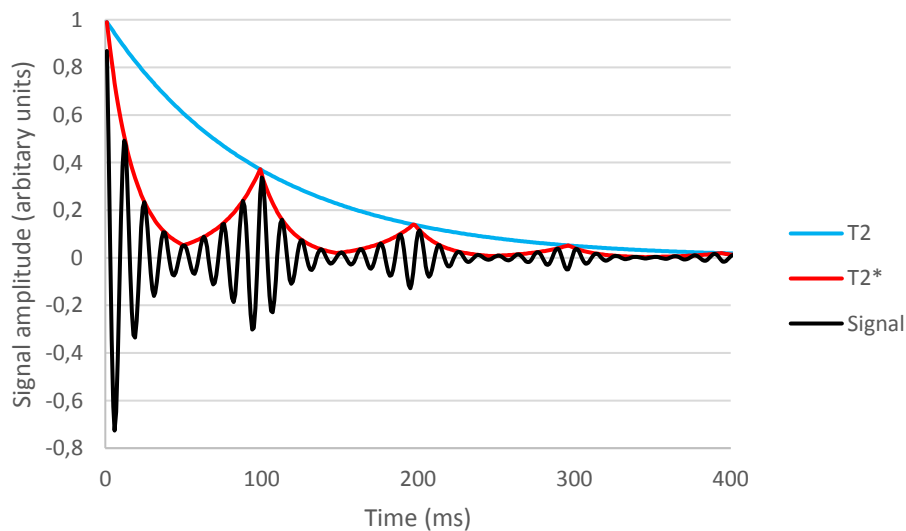


Figure 26. A hypothetical free induction decay (FID) signal. A refocusing a 180° pulse is applied at 50 ms and every 100 ms thereafter.

2.6.7 MR Imaging

Essentially, magnetic resonance imaging (MRI) involves acquiring and localizing multiple FID signals from an object and process the signals to form an image of the object. This chapter presents a simple localization method on a 2-dimensional slice of an object.

By applying a magnetic field gradient over the object (e.g. in the z direction) the spins can be made to precess at different frequencies. Then an RF pulse at a specific bandwidth can be transmitted into the object. It affects only the spins which are precessing at the frequencies within the bandwidth and can thus be used for the initial excitation of these spins using for example a 90° pulse. This step is called the slice selection. (Figure 27) [Plewes and Kucharczyk 2012]

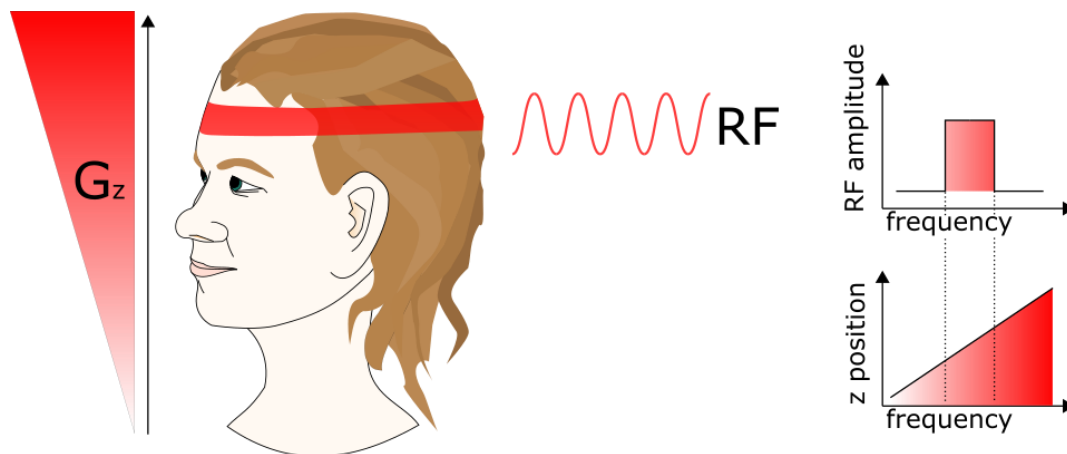


Figure 27. By applying a magnetic field gradient over the object the spins along the gradient axis start to precess at different frequencies. An RF pulse of a certain bandwidth is able to flip the spins whose frequencies are within the bandwidth.

Next, the spins within the slice have to be spatially encoded in the x and y directions. An MR signal has two properties that can be utilized for this: the phase and the frequency. Phase encoding is done by applying a magnetic field gradient (e.g. in the x direction) for a short while and letting the spins acquire different phases of precession. Thus the spins in the x direction are precessing at different phases but at the same frequency. The frequency encoding gradient is applied in the y direction simultaneously as the signal is acquired (Figure 28). [Plewes and Kucharczyk 2012]

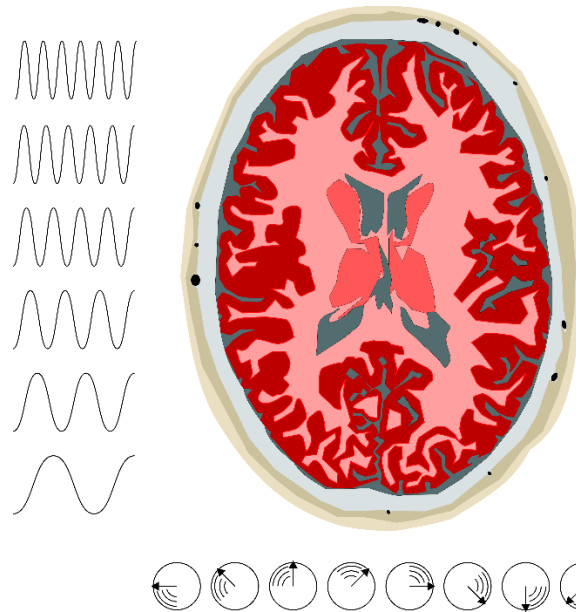


Figure 28. The spatial encoding in the selected (excited) slice is done by setting the spins on one axis (the horizontal in this example) precess at different phases before the signal acquisition and the spins along the other axis (the vertical in this example) precess at different frequencies during the signal acquisition.

The acquired signal is a combination of signals on a certain bandwidth and at different phases which is recorded into a 2-dimensional frequency domain matrix called K-space [Ljunggren 1983] as a single line. This process is repeated with varying amplitudes of the phase encoding gradient over and over again until the K-space is filled sufficiently. Finally using 2-dimensional Fourier transformation the K-space data is transformed into a 2-dimensional spatial domain image (Figure 29). [Plewes and Kucharczyk 2012] There are several ways to make the image acquisition faster and produce images with different contrasts but they are out of the scope of this thesis.

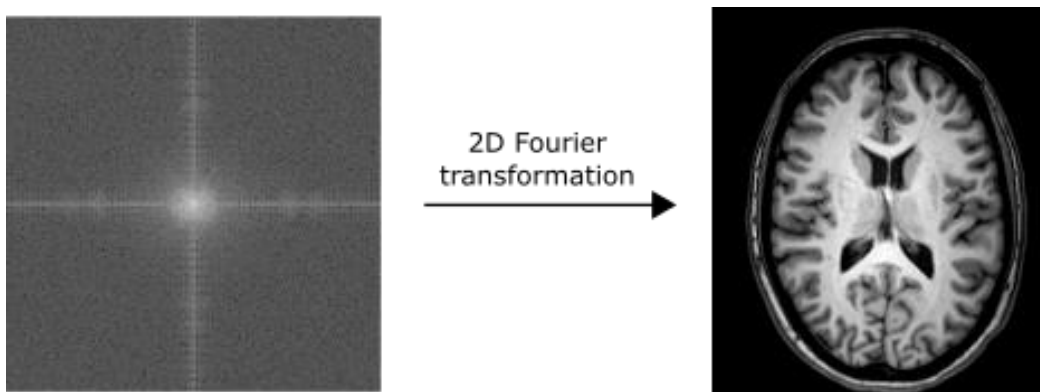


Figure 29. The raw data is stored into a frequency domain matrix called the K-space. A 2-dimensional Fourier transformation yields the image in the spatial domain.

2.6.8 MR Spectroscopy

The idea of MRI is to resolve the spatial origin of signals and their amplitudes. Usually just two frequencies matter: water and fat. On the contrary, the idea of magnetic resonance spectroscopy (MRS) is to resolve precisely what frequencies a signal from a certain point in tissue involves. This information is used for identifying biochemical substances and determining their concentrations. [Rhodes 2017] MRS is not restricted to measuring single volumes of tissue (single-voxel techniques): Multivoxel spectroscopy [Öz et al. 2014] and spectroscopic imaging [Peterson and Månsson 2013] can also provide spatial information by measuring MRS from multiple parts within an area of interest.

Most clinical applications of MRS are related to the brain where several products of metabolism (metabolites) can be used as markers for pathological conditions such as tumors [Polimeni and Uludağ 2018] or hypoxia [Zou et al. 2018]. Another clinically relevant organ is the liver where concentrations of water and lipids can be used as a marker for fatty liver disease [Qayyum 2009]. MRS of other organs is typically used only for research purposes.

The most used pulse sequences for single-voxel MRS are Stimulated Echo Acquisition Mode (STEAM) and Point Resolved Spectroscopy (PRESS). Due to the lower contribution of J-coupling effects [Ruschke et al 2016], the former is utilized in this thesis and is therefore given more attention. Both of the sequences consist of three consecutive RF pulses with simultaneous slice selecting gradients that are usually perpendicular to each other. The intersection of the pulses and gradients forms a rectangular volume from which the signal is recorded. The difference between STEAM and PRESS is that the former uses three 90° pulses (Figure 30) whereas the latter has one 90° pulse and two 180° pulses.

After the first 90° pulse in STEAM the magnetization starts to dephase in accordance of $T2^*$ relaxation immediately due to static field inhomogeneities and the applied gradients. At the time point $TE/2$ (time of echo divided by 2) a second 90° pulse flips the magnetization components so that the sum vector points opposite to the external field. However, due to the initial dephasing and also the additional magnetization excited by the second 90° pulse there are components of the magnetization that precess in the transversal plane after the flipping. A spoiler gradient is applied to dephase these components. The component of the magnetization that is pointing opposite to the external field experiences only $T1$ relaxation which is generally much longer than $T2$ or $T2^*$. The time between the first and second pulses is called the mixing time (TM). The second 90° pulse flips the magnetization vectors back to the transversal plane. Once again a gradient is applied to dephase the components that do not precess in the same plane as the sum magnetization, this time the components parallel to the longitudinal axis. Finally at the time point $TE + TM$ an echo appears. The amplitude is characterized similarly as in stimulated echo, namely affected by $T2$ relaxation, not $T2^*$. [Klose 2008]

STEAM can achieve shorter times of echo while PRESS provides twice as much signal due to its double spin echo behavior where each 180° rephrases the magnetization. Signal of STEAM sequence is lost due to the magnetization lost in the dephasing gradients. [Klose 2008]

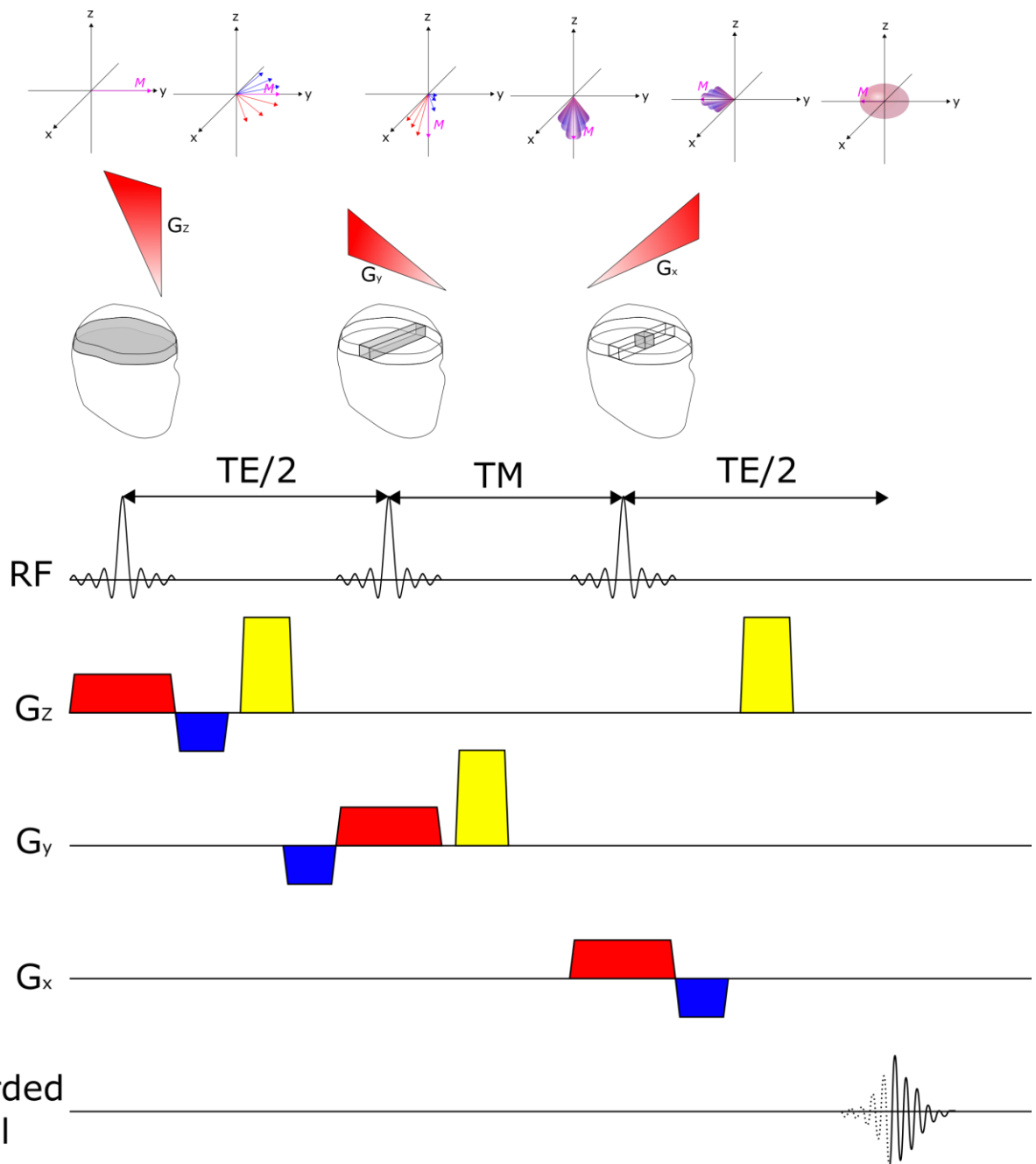


Figure 30. The pulse sequence scheme of STEAM where all three RF pulses flip the magnetization by 90° . The red blocks are the slice selecting gradients. The blue blocks are rephasing gradients which set the spins back into coherent precession after the slice selecting gradient. Yellow blocks are spoiler gradients (also known as crusher gradients) which reduce signals originating outside of the voxel. TE is the echo time and TM is mixing time which is the time that the magnetization resides pointing opposite to the external field.

2.6.9 Assessment of relaxation times

Both fat fraction and fatty acid composition have been shown to be affected by relaxation effects [Peterson et al. 2014]. Therefore measuring the relaxation times and correcting the results with them provides more accurate

results. The signal intensity as a function of relaxation times and timing parameters in the STEAM sequence can be written as follows:

$$S = S_0 \left(1 - e^{-\frac{TR-TM-TE/2}{T1}} \right) e^{-\frac{TE}{T2}} e^{-\frac{TM}{T1}} \quad (18)$$

where S is the recorded signal, S_0 is the initial signal intensity when no relaxation has yet occurred, TR is the repetition time, TM is the mixing time, TE is the echo time, $T2$ is the transversal relaxation time and $T1$ is the longitudinal relaxation time [Soher et al 1996].

When other components are kept constant the signal depends on the TE as follows:

$$S = S_0 e^{-\frac{TE}{T2}}. \quad (19)$$

The $T2$ constant can be solved as:

$$\ln(S) = \ln \left(S_0 e^{-\frac{TE}{T2}} \right) \quad (20)$$

$$\Rightarrow T2 = - \frac{TE \ln(S_0)}{\ln(S)}. \quad (21)$$

To determine the $T2$ relaxation time a linear regression on the natural logarithm of the resonance areas $\ln(S)$ of the $T2$ spectra and the echo times TE was conducted.

When all components in the equation (18) except TM are kept constant the signal depends on TM as follows:

$$S = S_0 e^{-\frac{TM}{T1}}. \quad (22)$$

As the dependence is similar as the function of signal over TE , the $T1$ time is determined similarly as $T2$ time by conducting a linear regression on the natural logarithm of the resonance areas of the $T1$ spectra and the mixing times. Finally, the regression results are inverted and multiplied by -1. Thus the equation for $T1$ time becomes:

$$\Rightarrow T1 = - \frac{TM \ln(S_0)}{\ln(S)}. \quad (23)$$

To correct the acquired signals S into the initial signals S_0 the individual signals of each spectrum (one general and five from each relaxation time measurement) were corrected by the following equation:

$$S_0 = \frac{S}{\left(1 - e^{-\frac{TR-TM-TE/2}{T1}}\right) e^{-\frac{TE}{T2}} e^{-\frac{TM}{T1}}}. \quad (24)$$

2.6.10 Assessment of fatty acid properties

The fatty acid properties can be assessed using the model presented by Hamilton [Hamilton et al. 2011]: The signal from the methylene between two double bonds produces a signal at 2.8 ppm (Figure 31). Thus, the number of methylene interrupted double bonds per triglyceride ($nmidb$) is calculated by dividing the normalized signal of diacyl at 2.8 ppm ($S_{2.8}$) by two:

$$nmidb = \frac{S_{2.8}}{2}. \quad (25)$$

The protons in a methane with a double bond produce a signal at 5.3 ppm. Thus, the number of double bonds is calculated from the normalized sum signal of glycerol and olefinic protons at 5.2 and 5.3 ppm ($S_{5.2+5.3}$):

$$ndb = \frac{S_{5.2+5.3} - 1}{2}. \quad (26)$$

The sum of the fractions of mono and polyunsaturated fatty acids ($f_{mufa} + f_{pufa}$) is calculated by subtracting $nmidb$ from ndb (the latter includes the former) and dividing the result by the number of carbon chains in a triglyceride:

$$f_{mufa} + f_{pufa} = \frac{ndb - nmidb}{3}. \quad (27)$$

By assuming that the number of double bonds in the fatty acids is less than 3 the fraction of polyunsaturated fatty acids (f_{pufa}) is calculated by dividing $nmidb$ by the number of carbon chains in a triglyceride i.e. 3:

$$f_{pufa} = \frac{nmidb}{3}. \quad (28)$$

The fraction of saturated fatty acids is calculated using the following equation:

$$f_{sfa} = 1 - (f_{mufa} + f_{pufa}). \quad (29)$$

The fatty acid chain length (CL) can be calculated using the following equation:

$$CL = \frac{S_{1.3} + 8ndb - 2nmidb}{6} + 4, \quad (30)$$

where $S_{1.3}$ is the signal of methylene protons at 1.3 ppm.

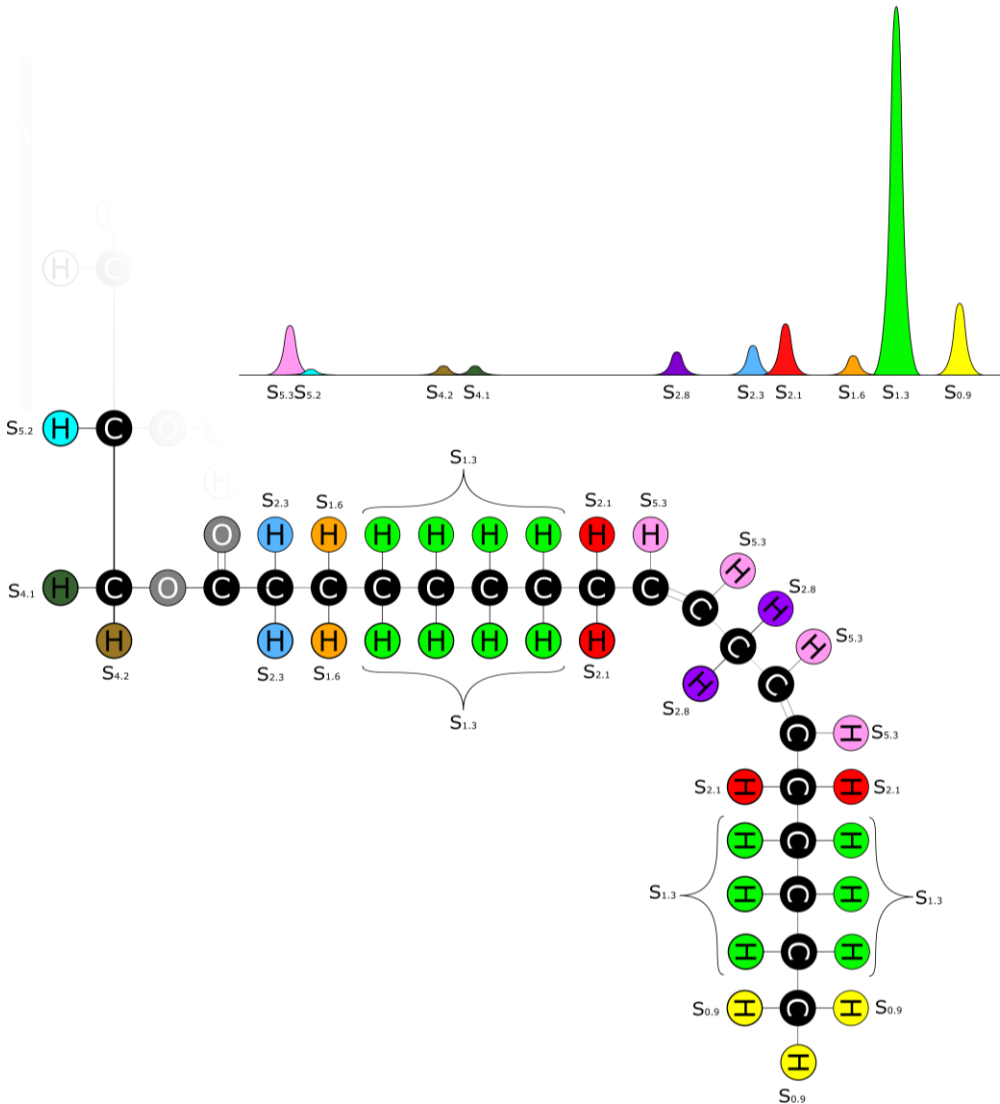


Figure 31. Protons in a single fatty acid of a triglyceride and their signals in a spectrum are color coded and named according to their frequency in ppm scale, for example $S_{0.9}$ marks the signal of the methyl protons precessing at 0.9 ppm.

2.6.11 Assessment of fat fraction

In magnetic resonance studies fat fraction is usually assessed as proton density fat fraction (PDFF) [Reeder et al 2012] in which the fat fraction of tissue is given by the ratio of fat signals and the sum of fat and water signals. MRI methods have usually utilized the 2-point Dixon method in which MR signal is acquired at two echo times: with water and fat at the same phase and at opposite phases. From this raw data images with only water and only fat can be reconstructed [Dixon 1984]. However, this method is affected by the $T2^*$ relaxation and only the methyl signal of lipids are considered as fat. Therefore, multi-echo methods have

been developed for more accurate fat quantitation [Peterson and Månsson 2014]. In adipose tissue MRS the fat fraction can be calculated by taking into account all fat signals as follows:

$$FF = \frac{S_{rel,09} + S_{rel,13} + S_{rel,16} + S_{rel,21} + S_{rel,23} + S_{rel,28} + 4 + S_{rel,52} + S_{rel,53}}{S_{rel,09} + S_{rel,13} + S_{rel,16} + S_{rel,21} + S_{rel,23} + S_{rel,28} + 4 + S_{rel,52} + S_{rel,53} + S_{rel,water}}, \quad (31)$$

where S_{rel} is a normalized signal of a component, the number in the lower index denotes the frequency of the triglyceride signal. The number 4 compensates for the strongly J-coupled signals at 4.1 and 4.2 ppm (Hamilton et al. 2011) which were excluded.

3 OBJECTIVES OF THE STUDY

- 1) The measurement of fatty acid properties on the 3T Philips Ingenuity TF PET/MR (Philips Healthcare, Cleveland, OH, USA) imaging system was validated using a phantom with fat and various oil samples.
- 2) The fatty acid properties of human BAT and WAT were determined and their change in response to cold exposure was studied.

4 MATERIALS AND METHODS

4.1 Samples for phantom validation

The measurement of fatty acid properties was validated using lipid samples which differ from one another in their fatty acid characteristics. Seven edible oils and butter were bought at local grocery stores: avocado oil (Emile Noël Avocado organic virgin oil), butter (Pirkka suomalainen voi), medium-chain triglyceride (MCT) oil (Cocovi MCT-öljy), olive oil (Pirkka extra-neitsytoliiviöljy), palm oil (Bonred Punainen palmuöljy), rapeseed oil (Rainbow rapsiöljy) and sunflower oil (Keiju auringonkukkaöljy). Fatty acid properties as given in the sample labels are listed in Table 1. Also listed in the table are the number of double bonds (ndb) and the number of methylene interrupted double bonds (nmidb) which are calculated based on the fatty acid properties using formulas (25) and (26). Chain length values are based on literature [Institute of Shortening and Edible Oils 2016; Flores et al. 2019]. The label of butter did not have information on the values of monounsaturated and polyunsaturated fatty acids. Therefore, all values of butter fatty acid properties in Table 1 are based on literature [Institute of Shortening and Edible Oils 2016]. Butter is also the only sample with less than 100% fat. According to the label the butter it contains 80% fat, 1% carbohydrates, less than 1% protein and 1.5% salt.

Table 1. The samples used in the validation study with their fatty acid properties as stated in their labels. Number of double bonds (ndb) and number of methylene interrupted double bonds (nmidb) calculated using formulas (25) and (26) and expressed as average per triglyceride. Chain length (CL) values are based on literature [Institute of Shortening and Edible Oils 2016]

Sample type	f_{sfa} (%) ^a	f_{mufa} (%) ^b	f_{pufa} (%) ^c	ndb	nmidb	CL ^d
Avocado oil	20	65	15	2.85	0.45	17.18
Butter ^d	66	31	3	1.14	0.09	15.59
Medium-chain triglyceride (MCT) oil	100	0	0	0	0	8.88
Olive oil	15	78	7	2.76	0.21	17.74
Palm oil	41	46	13	2.16	0.39	17.06
Rapeseed oil	7	62	31	3.72	0.93	17.92
Sunflower oil	12	30	58	4.38	1.74	17.86

^a Fraction of saturated fatty acids (f_{sfa}); ^b Fraction of monounsaturated fatty acids (f_{mufa}); ^c Fraction of polyunsaturated fatty acids (f_{pufa}), ^d literature values [Institute of Shortening and Edible Oils 2016].

4.2 Construction of a phantom

A phantom was constructed from a 1-litre plastic yoghurt container. Seven 50 ml test tubes were attached to the lid of the container using sanitary silicone (Figure 32). The test tubes were filled with the samples, closed and the remaining volume of the container was filled with tap water. The water in between the test tubes made the phantom more uniform and thus helped the MRI scanner reach a better shimming of the magnetic field within the phantom. It also provided a strong reference water signal for the calibration of the frequency scale. A 1.5 ml Eppendorf tube filled with sunflower oil was attached with tape between two test tubes to provide a

reference for orientation of the phantom in the MRI images. Otherwise it would have been hard to distinguish the test tubes from one another when the spectroscopic voxels were placed in the samples.

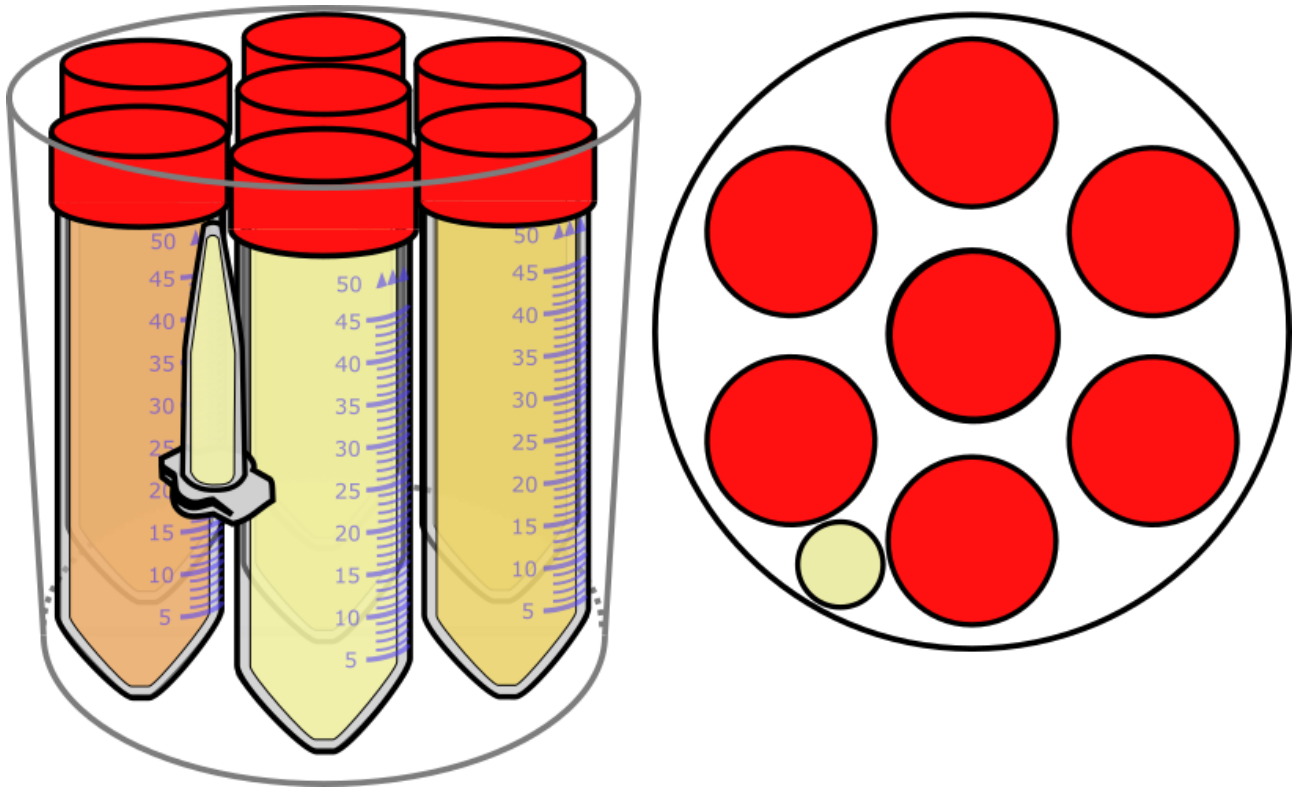


Figure 32. A schematic illustration of the phantom used for the validation measurements. A view from the top on the right.

4.3 Phantom measurements

All measurements were performed using a 3T Philips Ingenuity TF PET/MR (Philips Health Care, Amsterdam). The phantom was inserted into a Philips SENSE Head 32 coil. After survey, B1 calibration and reference scans, an mDixon image was taken in three orthogonal directions (axial, coronal and sagittal). The parameters of the mDixon sequence are listed in Table 2. All three scans were identical except for the orientation.

Table 2. The parameters of the mDixon sequence used for localization of the samples.

Parameter	Value
Scan time (s)	8.6
TR/TE1/TE2 (ms)	3.3 / 1.17 / 2.1
Acquisition voxel size (mm)	1.50 / 1.50 / 3.00
Reconstructed voxel size (mm)	0.94 / 0.94 / 1.50
Bandwidth (Hz)	1944.4
Field of view Right-left / anterior-posterior / feet-head (mm)	150 / 150 /150
Scan mode	3D
Scan technique	Fast Field Echo
Flip angle (°)	10

Three proton (^1H) MRS sequences were performed on each sample: a single good quality measurement, a T2 relaxation time series and a T1 relaxation time series. In the relaxation time series five spectra with altering TE or TM values were recorded. The parameters of the measurements are listed in Table 3. Single voxel STEAM sequence was used in all measurements. Suppression of water or any other components was not used. For time saving reasons the repetition time in the T2 and T1 series was made shorter and the number of acquisitions smaller than in the single measurement. The measurement time in the Table 3 does not include the time needed for preparation steps which typically last less than one minute for each sequence. The total time to measure all the seven samples was more than two hours.

Table 3. The parameters of the phantom spectroscopy measurements.

Parameter	Single	T2	T1
Measurement time (min:s)	3:18	5:40	8:20
Readout duration (ms)	2048	1024	1024
TR (ms)	3000	2000	2000
TE (ms)	11	15 / 30 / 45 / 60 / 75	11
TM (ms)	17	17	20 / 80 / 140 / 200 / 260
Number of acquisitions	64	32	48
Phase cycles	16	16	16
Voxel size AP / RL / FH (mm)	10 / 10 / 10	10 / 10 / 10	10 / 10 / 10
Number of data points	4096	2048	2048
Bandwidth (Hz)	2000	2000	2000
Flip angle (°)	90	90	90
Shim mode	2 nd order pencil beam	2 nd order pencil beam	2 nd order pencil beam

4.4 Data postprocessing

After the measurements, the spectra were exported into a memory stick in Philips SPAR/SDAT format. Then they were analyzed on LCModel software (version 6.3-0C) using the “lipid-8” protocol. The software provided the estimated resonance areas of each spectral peak in arbitrary units in CSV files which were further processed on Microsoft Excel (2013).

The relaxation time correction was performed as described in chapter 2.6.9: The T1 and T2 relaxation time were assessed from the data of T1 and T2 sequences using equations 21, and 23. The signals of all metabolites in all spectra were then corrected for the relaxation effects using equation 24.

The relaxation-effect-corrected signals were then normalized by using the signals of methyl at 0.9 ppm and α -carboxyl at 2.3 ppm. These signals were the most reliable based on their coefficients of variation of the signal value estimates provided by LCModel. In a single triglyceride molecule, the signal of methyl is given by nine protons and the signal of α -carboxyl by six protons. Thus, the normalization of each signal S_0 was performed using the following equation:

$$S_{rel} = \frac{S_0}{S_{0.9} + S_{2.3}} \times 15 \quad (32)$$

where $S_{0.9}$ is the corrected signal of methyl at 0.9 ppm and $S_{2.3}$ is the corrected signal of α -carboxyl at 2.3 ppm.

4.5 Fatty acid properties of the samples

The fatty acid properties were determined from all the acquired spectra: the good quality single spectrum and the five spectra in T2 series and five spectra in T1 series. Thus there were eleven measurements of each sample. Fatty acid properties were calculated using the formulas (25), (26), (27), (28) (29) and (30).

4.6 Fat fraction of butter

Although not the primary aim of this study, the fat fraction of the butter sample was determined using formula (31) as it is usually the main interest of clinical trials with adipose tissue ^1H MRS.

4.7 Spectral quality in the validation experiment

The LCModel spectral analysis program provides values for full-width at half-maximum (FWHM) and signal-to-noise ratio (SNR) for each spectrum (11 of each sample). The former is defined in the manual only as “a rough estimate of the linewidth” whereas the latter has been given a more precise definition of being “the ratio of the maximum in the spectrum-minus-baseline over the Analysis Window to twice the rms Residuals”. [LCModel_manual] Both parameters depend obviously on the parameters TE and TM. Still, they were compared between the samples to confirm a uniform quality. The program also provides estimates of standard deviations (Cramér-Rao lower bounds) of the estimated concentrations of the signals. The values are given in percentages and indicate how much the estimated concentration can deviate from the given value.

4.8 In vivo human study design

The human study was given approval by the ethics committee of the Hospital District of Southwest Finland. The 4 subjects (3 females, 1 male) recruited for this study had been studied 3 years prior in Dixon BAT project [Koskensalo et al. 2017]. All study subjects signed a written informed consent. Age range of the subjects was 29 – 40 years and BMI range was 19.8 – 26.0 kg/m². All subjects were studied in ambient condition and 3 also in cold exposure. Both studies were performed in fasting condition.

4.9 Cold exposure

The cold exposure was performed using an adjustable cooling blanket (temperature range 4 – 18°C). A non-shivering cold exposure was maintained by adjusting the temperature. Shivering and arrhythmias were monitored using an electrocardiogram recording visually. The study subjects were also asked about cold sensation and muscle tremor. The cold exposure was started 2 hours prior to entering the MRI. Electrocardiogram was monitored during the exposure to detect arrhythmias and muscle tremor which was also estimated visually and asking the study subjects' sensations. The only exception to the previous exposure protocol was that cooling of feet during the MRI imaging was not performed in this study.

4.10 Human measurements

The human MRI and ¹H MRS were performed using the same imaging system as in the phantom study. Instead of the 32-channel SENSE Head coil a 32-channel SENSE cardiac coil was used. The anterior part of the coil was placed as close to the subjects' chins as possible to cover the two areas of interest sufficiently. These were 1) the supraclavicular BAT being the most prominent sine for brown adipocytes in humans and 2) the subcutaneous adipose tissue in the upper back. This location will be referred to as WAT. An mDixon image was taken in three orientations to provide an anatomical reference for the positioning of the ¹H MRS voxel. The border between muscle and adipose tissue is well visible in the out-phase image due to the signal loss in the areas with both tissues (Figure 33). Parameters of the mDixon sequence are listed in Table 4.

Table 4. Parameters of the mDixon MRI sequences.

Slice orientation	Transversal	Coronal	Sagittal
Scan time (s)	16.1	11.1	5.8
TR/TE1/TE2 (ms)	3.1 / 1.07 / 1.9	3.0 / 1.08 / 1.9	3.0 / 1.08 / 1.9
Acquisition voxel size (mm)	1.75 x 2 x 1.5	1.74 / 1.99 / 3.00	1.74 / 2.01 / 3.00
Reconstructed voxel size (mm)	1 x 1 x 1	1.01 / 1.00 / 1.50	0.95 / 0.93 / 1.50
Bandwidth (Hz)	1898.6	2250.2	2250.2
Field of view Right-left / anterior-posterior / feet-head (mm)	450 x 302.3 x 199.5	479.2 x 90 x 250	75 x 298.6 x 250
Scan mode	3D	3D	3D
Scan technique	Fast Field Echo	Fast Field Echo	Fast Field Echo
Flip angle (°)	10	10	10

The voxels were placed carefully in the same positions as they were in the previous Dixon BAT study: BAT MRS was acquired from the supraclavicular adipose tissue and the WAT MRS from the upper thoracic subcutaneous fat in the back (Figure 33). As in the phantom study three ¹H MRS sequences were performed: a single good quality measurement, a T2 relaxation time series and a T1 relaxation time series. The parameters of the sequences are listed in Table 5.

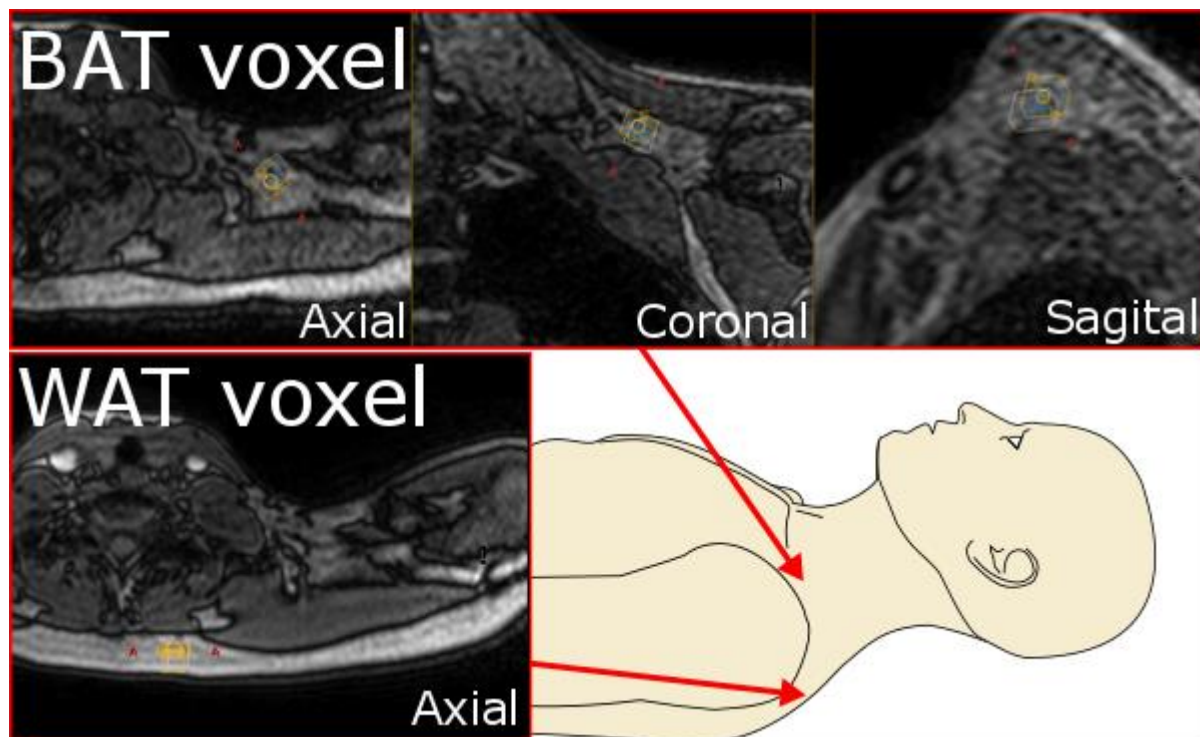


Figure 33. The positions of the spectroscopic voxels: BAT was measured from the supraclavicular adipose tissue depot and WAT from the upper posterior thoracic subcutaneous adipose tissue. The MR images are out-phase images of the mDixon sequence showing the characteristic signal loss between fat and water containing tissues. Yellow voxel represents the origin of water signal and white voxel the origin of fat signal.

Table 5. The parameters of the human spectroscopy measurements.

Parameter	Single	T2	T1
Measurement time (min:s)	3:18	5:40	8:20
Readout duration (ms)	512	512	512
TR (ms)	3000	2000	2000
TE (ms)	11	15 / 30 / 45 / 60 / 75	11
TM (ms)	17	17	20 / 80 / 140 / 200 / 260
Number of acquisitions	64	32	48
Phase cycles	16	16	16
Voxel size AP / RL / FH (mm)	10 / 10 / 10	10 / 10 / 10	10 / 10 / 10
Number of data points	1024	1024	1024
Bandwidth (Hz)	2000	2000	2000
Flip angle (°)	90	90	90
Shim mode	2 nd order pencil beam	2 nd order pencil beam	2 nd order pencil beam

The spectra were analyzed and processed similarly as the phantom spectra. However, the quality of the human data was significantly worse due to physiological reasons and therefore the relaxation values could not be determined reliably for all single lipid signals. In such cases the relaxation was determined for a sum of signals which LCModel can detect with better confidence. For example, instead of determining the T2 relaxation of $S_{2.8}$ it was determined for the sum signal of $S_{2.1}$, $S_{2.3}$ and $S_{2.8}$. This value was then used for relaxation correction of $S_{2.8}$. For one subject the measurement of T1 times of BAT signals failed due to a technical failure in both cold exposed and warm condition. In this case the median of the relaxation values of all other subjects in both organs (BAT and WAT) and conditions (cold and warm) was used.

The following criteria was set for the quality of the data for determining the fatty acid characteristics: $SNR > 40$, $FWHM < 0.5$ and standard deviations of signals $S_{0.9}$, $S_{2.3}$ and $S_{5.2+5.3} < 200\%$. Thus 29 of the total 144 spectra were excluded.

The most dominant signals in the formula for fat fraction (31) are water at 4.7 ppm and methylene at 1.3 ppm. Thus, the quality of the spectra does not need to be as high as in determining fatty acid characteristics in which weak signals such as the sum of glycerol and olefinic protons at 5.2 and 5.3 ppm ($S_{5.2+5.3}$) have to be detected with good confidence. Therefore, for fat fraction analysis all spectra were included except the ones that did not meet the following criteria: SNR over 10, and standard deviations of signals $S_{1.3+1.6}$ and S_{water} less than 200%. Thus 6 of the 144 spectra were excluded.

4.11 Statistical analysis

The normality of continuous variables was evaluated visually using histograms. Two-sample t-test or Mann-Whitney U-test was used to test the differences in continuous variables. Adjusted analyses were performed

using standard least squares analysis. A 2-sided p-value less than 0.05 was considered statistically significant. All statistical analyses were performed using JMP Pro for Mac, version 14.2 (SAS institute Inc, Cary, NC).

5 RESULTS

5.1 Relaxation times of the samples

The determined relaxation times of the metabolites and their sums are presented in Table 6 and Table 7. The relaxation times could not be reliably resolved for the lipid signals at 1.6 and 5.3 ppm as they overlap with the adjacent stronger signals. Likewise the values were not determined for signal at 4.1 and 4.2 ppm as they are strongly J-coupled. An example spectrum of sunflower oil is presented in Figure 34 with signal annotations. Examples of the spectra of the other samples are presented in Figure 35.

Table 6. The measured T2 values of the samples. The triglyceride signals are named according to their frequencies in ppm units. All numbers of the table in ms units.

	S_{0.9}	S_{1.6}+S_{1.3}	S_{2.1}	S_{2.3}	S_{2.8}	Water	S_{5.2}+S_{5.3}
Avocado oil	39.40	66.88	33.78	34.56	32.79		42.96
Butter	40.44	56.51	34.35	32.71	18.37	41.20	41.81
MCT oil	41.77	72.64	25.48	58.55	13.04		34.42
Olive oil	39.91	70.63	35.38	38.29	32.32		47.83
Palm oil	41.77	79.75	35.29	41.01	34.85		45.42
Rapeseed oil	45.66	63.69	34.65	40.25	38.43		41.36
Sunflower oil	42.30	57.95	31.12	58.21	41.73		41.73

Table 7. The measured T1 values of the samples. The signals are named according to their frequencies in ppm units. All numbers of the table in ms units.

	S_{0.9}	S_{1.6}+S_{1.3}	S_{2.1}	S_{2.3}	S_{2.8}	Water	S_{5.2}+S_{5.3}
Avocado oil	451.9	262.2	238.3	166.7	267.4		413.7
Butter	457.6	263.90	368.5	198.4	359.9	864.3	423.7
MCT oil	547.5	346.23	111.4	240.9	490.3		327.7
Olive oil	473.0	266.9	228.2	168.8	240.3		387.1
Palm oil	500.4	291.5	267.6	193.7	351.2		414.2
Rapeseed oil	523.5	270.6	269.6	182.2	341.8		415.0
Sunflower oil	566.3	300.8	316.3	204.2	335.4		421.9

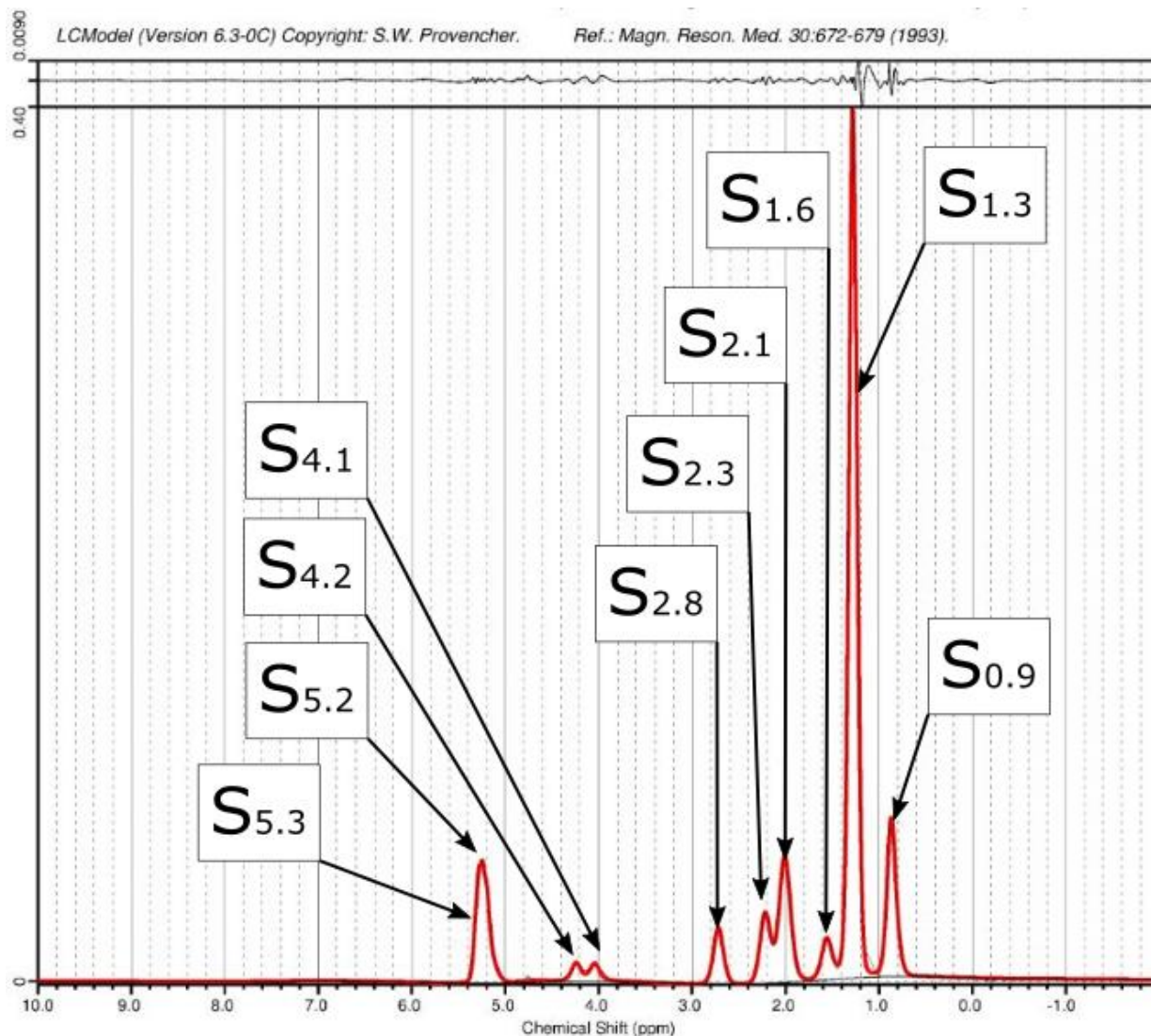


Figure 34. An LCMoel printout of a sunflower oil spectrum with added signal annotations. The fitted signal is plotted red and the recorded signal black. Due to a near-perfect fitting result the recorded signal is overlapped by the fitted signal. The black curve at the top is the residual of the fitted signal. The signals are named according to their frequencies in ppm units.

5.2 Fatty acid properties of the samples

The results of the fatty acid properties are presented in Table 8 and the measurement errors in Table 9 (Figure 36). The errors are presented graphically in Figure 36. The determined ndb and nmldb values correlated well with the values calculated based on the labels of the samples ($R^2 = 0.97$ for ndb, $R^2 = 0.95$ for nmldb and $R^2 = 0.89$ for CL). The correlations are presented graphically in Figure 37.

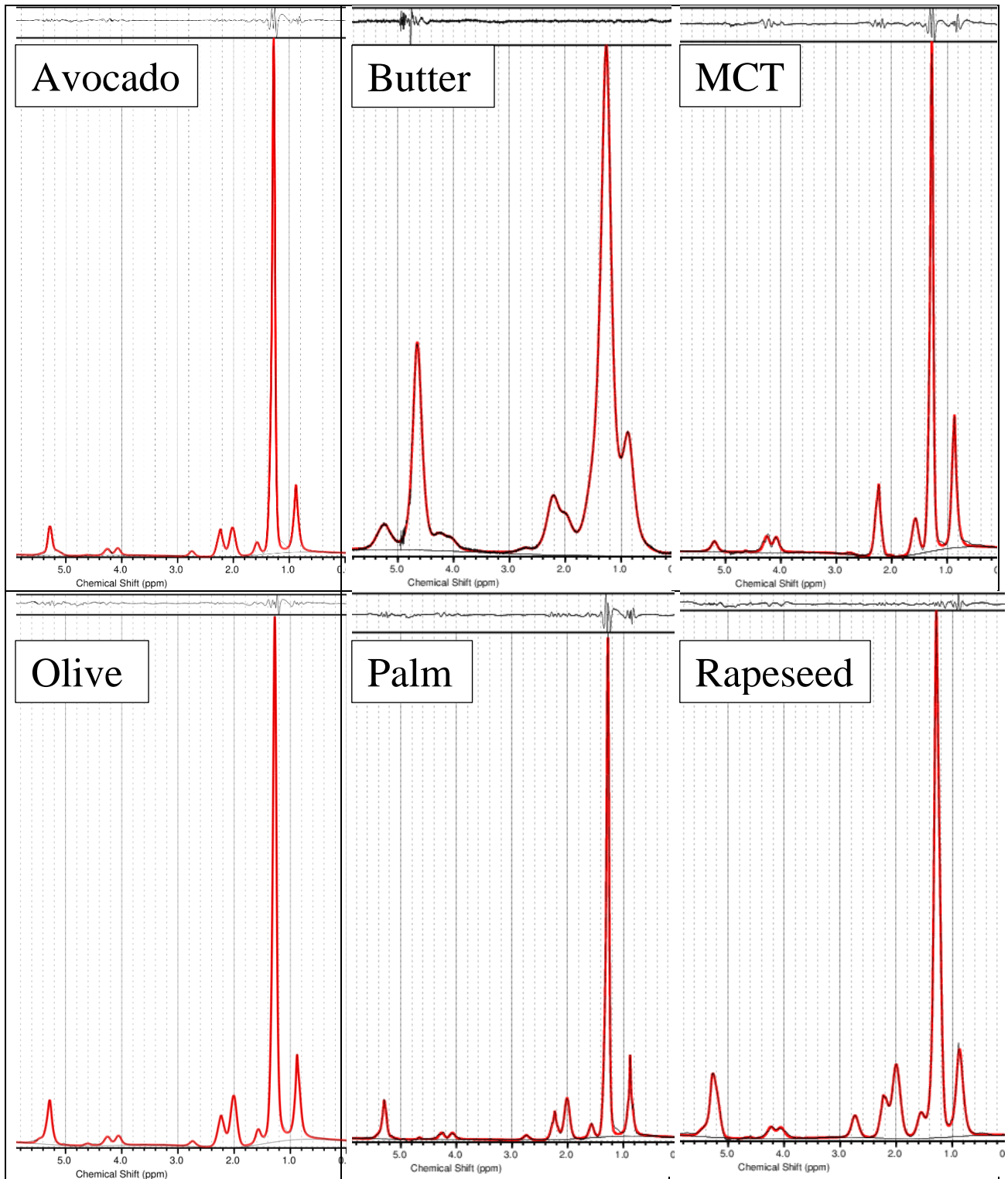


Figure 35. Single spectra of all samples except sunflower oil (Figure 34). Note the amplitude differences of signal $S_{2.8}$ which originates from the methylene molecules between double bonded methines and amplitude differences of signal $S_{5.2}$ which originate from the double bonded methines. Note also the considerably larger width of butter signals which is possibly caused by the added salt of the product. Butter is also the only sample with water content (20 %).

Table 8. The determined fatty acid properties presented as median (range).

Sample	f _{sfa} (%)	f _{mufa} (%)	f _{pufa} (%)	ndb	nmidb	CL error
Avocado oil	30.1 (19.0 – 39.3)	53.9 (47.6 – 70.8)	12.1 (8.6 – 16.4)	2.59 (2.14 – 2.76)	0.36 (0.26 – 0.49)	13.4 (11.7 - 14.6)
Butter	72.5 (61.6 – 76.0)	26.1 (18.0 – 36.4)	3.4 (0.6 – 7.0)	0.98 (0.86 – 1.22)	0.10 (0.02 – 0.21)	12.5 (11.5 - 14)
MCT oil	99.5 (92.8 – 102.1)	-1.0 (-5.3 – 6.2)	1.0 (0.0 – 3.3)	0.04 (-0.06 – 0.25)	0.03 (0.00 – 0.10)	7.4 (6.8 - 7.8)
Olive oil	26.4 (24.1 – 37.1)	62.5 (52.6 – 66.9)	10.0 (7.3 – 12.4)	2.50 (2.14 – 2.58)	0.30 (0.22 – 0.37)	13.8 (12.4 - 14.6)
Palm oil	49.5 (39.0 – 55.7)	37.3 (30.0 – 50.6)	13.2 (10.4 – 18.4)	1.94 (1.64 – 2.14)	0.39 (0.31 – 0.55)	13.4 (12.2 - 14.1)
Rapeseed oil	7.3 (3.5 – 18.2)	46.0 (34.8 – 52.6)	44.8 (39.2 – 58.0)	4.09 (3.72 – 4.53)	1.35 (1.18 – 1.74)	15.7 (14.4 - 17.3)
Sunflower oil	8.1 (0.3 – 37.1)	33.3 (10.6 – 42.1)	57.7 (50.9 – 69.2)	4.42 (3.42 – 4.96)	1.73 (1.53 – 2.08)	15.3 (12.9 - 16.7)

Table 9. The errors of the fatty acid properties. The values are calculated as the subtraction of the measured values and the values in the labels (Table 1). All values are presented as median (range).

Sample	f _{sfa} error (%)	f _{mufa} error (%)	f _{pufa} error (%)	ndb error	nmidb error	CL error
Avocado oil	10.1 (-1.0 - 19.3)	-11.1 (-17.4 – 5.8)	-2.9 (-6.4 – 1.4)	-0.26 (-0.71 – -0.09)	-0.09 (-0.19 – 0.04)	3.8 (2.5 - 5.5)
Butter	6.5 (-4.4 – 10.0)	-4.9 (-13.0 – 5.4)	0.4 (-2.4 – 4.0)	-0.10 (-0.22 – 0.14)	-0.02 (-0.10 – 0.09)	3.1 (1.6 - 4.1)
MCT oil	-0.5 (-7.2 - 2.1)	-1.0 (-5.3 – 6.2)	1.0 (0.0 – 3.3)	0.04 (-0.06 – 0.25)	0.03 (0.00 – 0.10)	1.5 (1.1 - 2.1)
Olive oil	11.4 (9.1 - 22.1)	-15.5 (-25.4 – -11.1)	3.0 (0.3 – 5.4)	-0.26 (-0.62 – -0.18)	0.09 (0.01 – 0.16)	3.9 (3.2 - 5.3)
Palm oil	8.0 (-2.5 - 14.2)	-8.5 (-15.8 – 4.8)	0.5 (-2.3 – 5.7)	-0.22 (-0.52 – -0.02)	0.00 (-0.08 – 0.16)	3.6 (2.9 - 4.9)
Rapeseed oil	0.3 (-3.5 - 11.2)	-16.0 (-27.2 – -9.4)	13.8 (8.2 – 27.0)	0.37 (0.00 – 0.81)	0.42 (0.25 – 0.81)	2.2 (0.7 - 3.6)
Sunflower oil	-3.9 (-11.7 - 25.1)	3.3 (-19.4 – 12.1)	-0.3 (-7.1 – 11.2)	0.04 (-0.96 – 0.58)	-0.01 (-0.21 – 0.34)	2.5 (1.2 - 5.0)

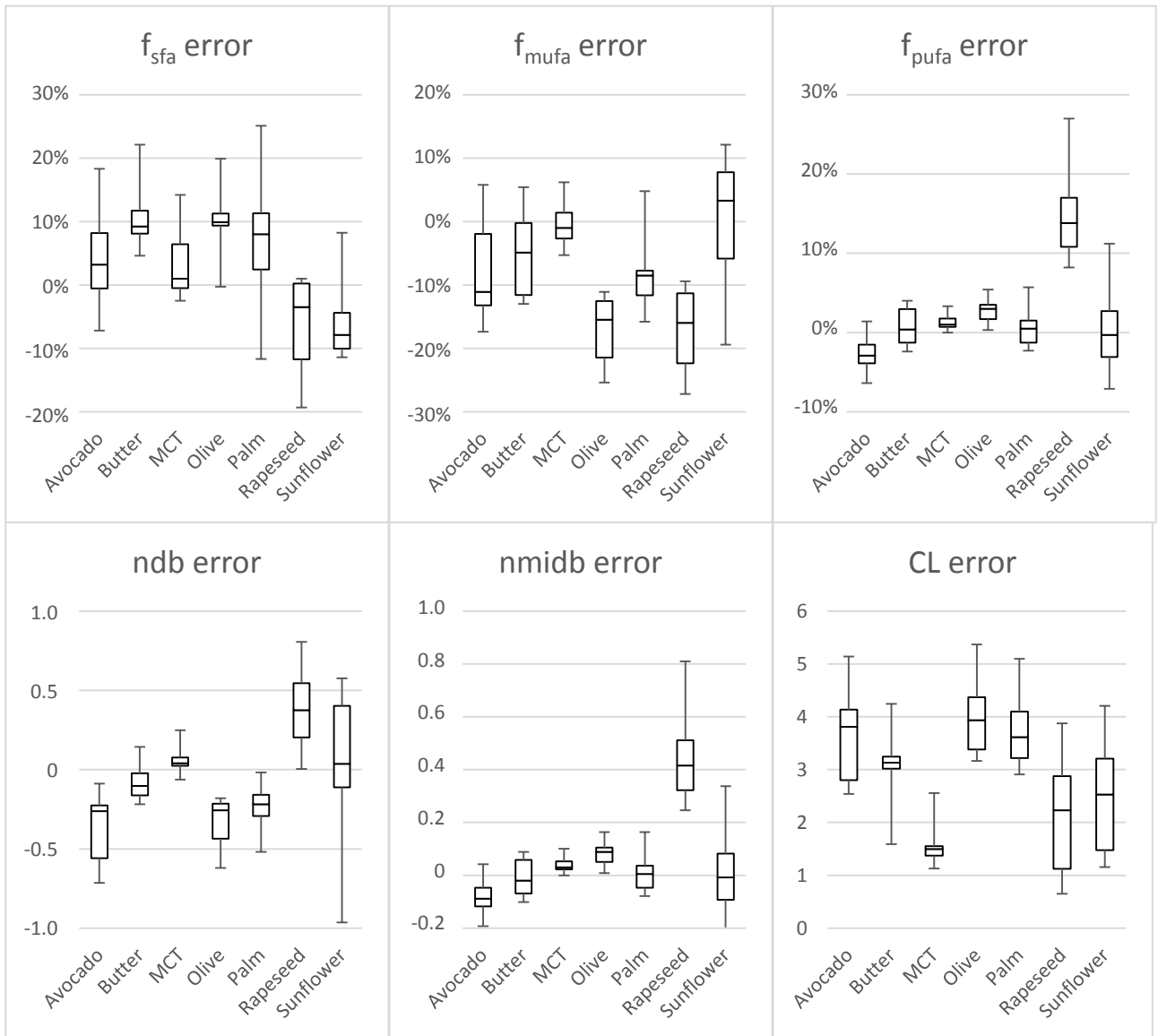


Figure 36. Whisker plots representing the median and range of the absolute measurement errors in each sample.

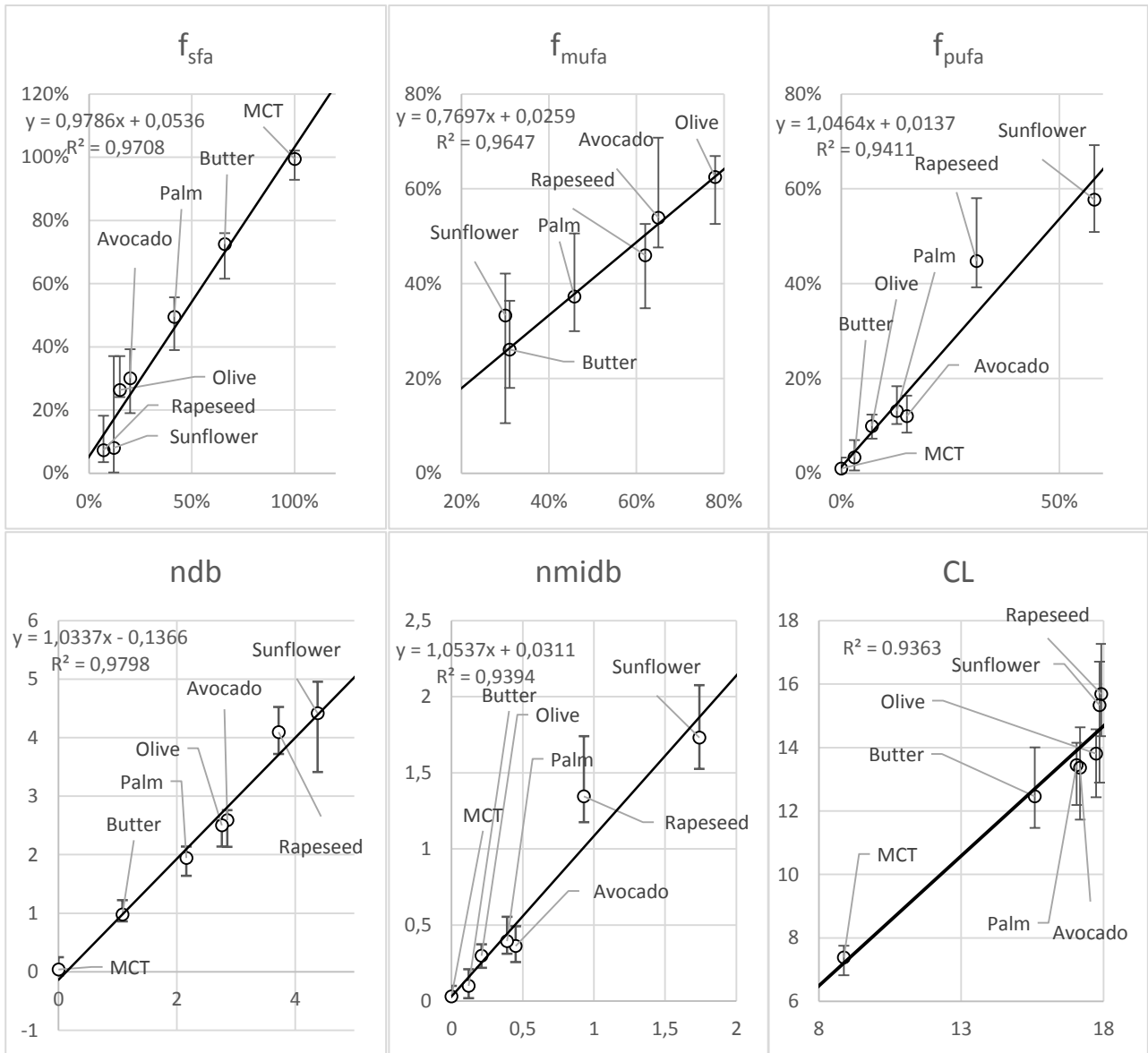


Figure 37. The correlations between the median (range) of the measured values and the values given by sample label information.

5.3 Fat fraction of butter

The fat fraction of butter was determined from 11 spectra. The median (range) of the values was 86.5% (86.4% - 87.1%). The individual fat fractions of each spectra are visualized in Figure 38.

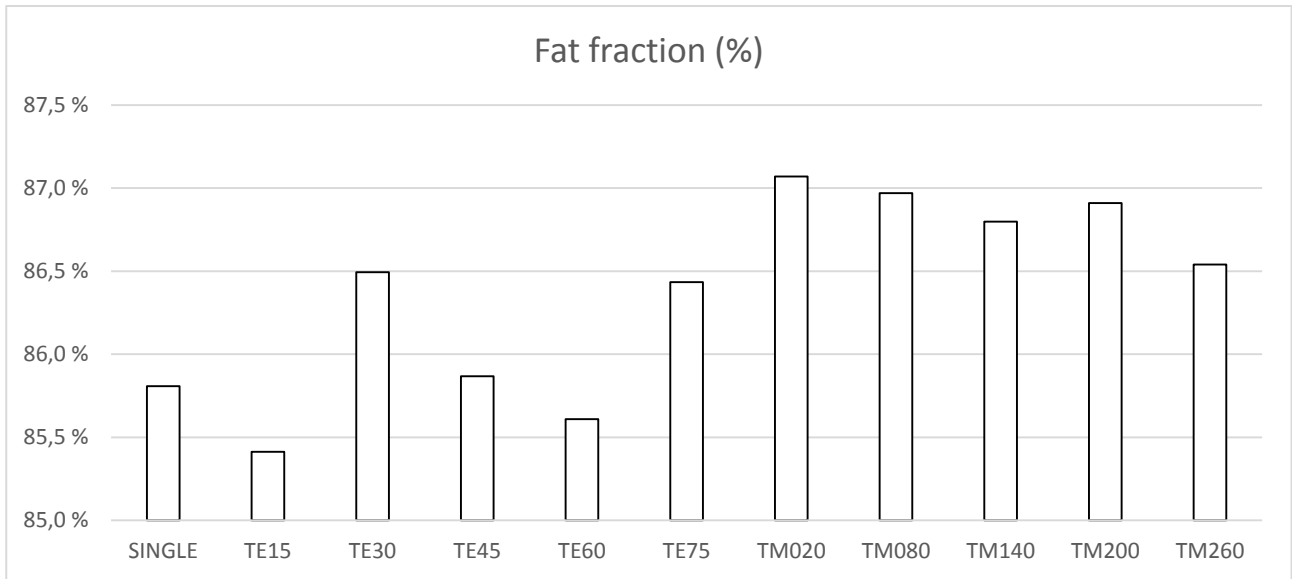


Figure 38. The fat fraction of each 11 butter spectra. The labeling refers to the series of the measurement (TE from the T2 series, TM from the T1 series) and the number refers to the echo or mixing time.

5.4 Spectral quality of the validation experiment

The spectral quality parameters SNR and FWHM are listed in Table 10 and graphically in Figure 39. SNR values differed between most samples but were within the same magnitude in all spectra. The FWHM values differed significantly between all samples except between sunflower and avocado oils and between rapeseed and avocado oils. However, the FWHM values in Butter spectra were almost three times higher than in any of the other samples.

Table 10. The mean (SD) SNR and FWHM in each sample.

	Avocado oil	Butter	MCT oil	Olive oil	Palm oil	Rapeseed oil	Sunflower oil
SNR mean (SD)	259.0 (20.0)	258.3 (82.1)	157.5 (8.8)	229.7 (42.9)	200.2 (21.7)	226.5 (50.2)	176.5 (19.5)
FWHM mean (SD)	0.074 (0.002)	0.219 (0.002)	0.063 (0.001)	0.061 (0.003)	0.058 (0.003)	0.073 (0.002)	0.076 (0.002)

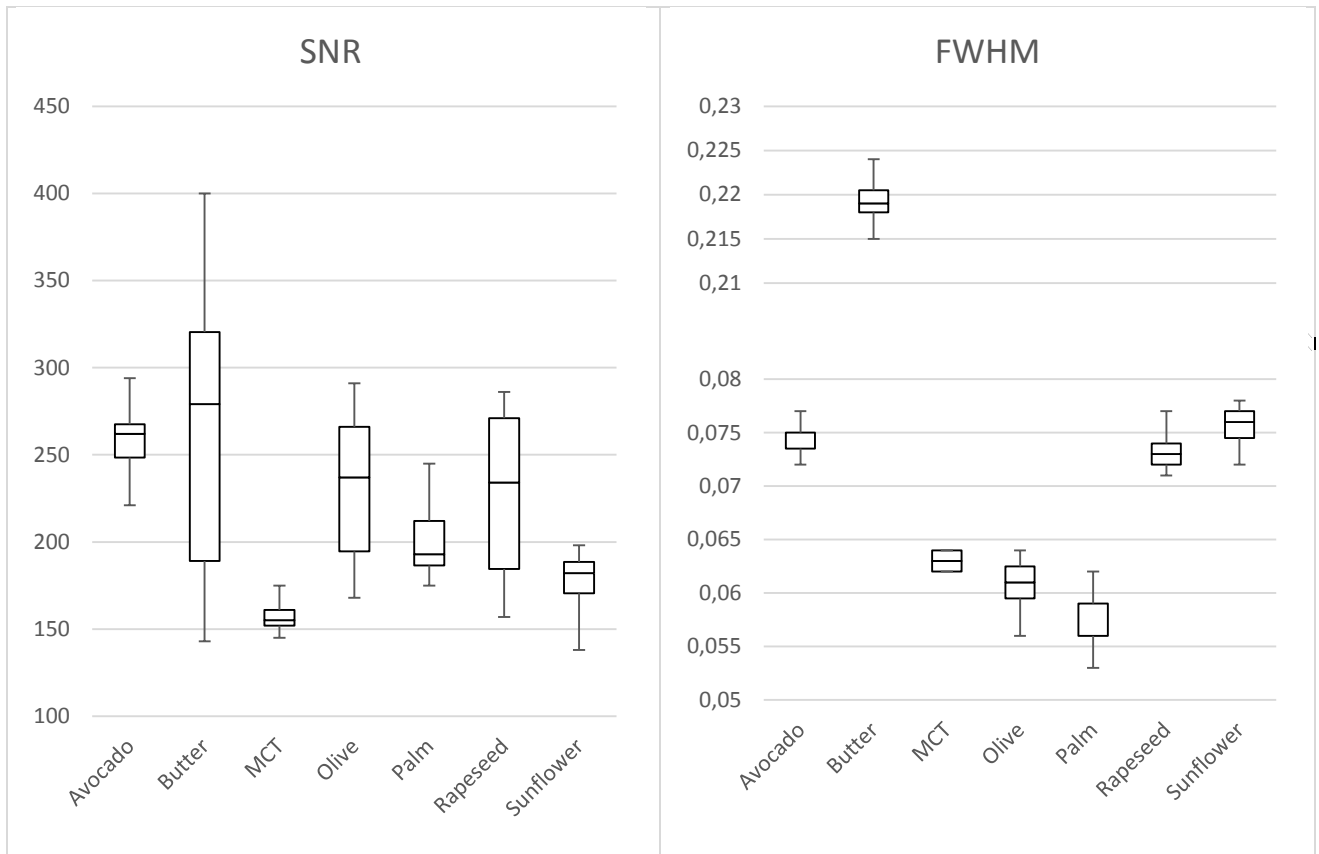


Figure 39. The distributions of the SNR and FWHM values in the spectra of the samples. Note that the vertical axis of the FWHM graph has been broken between 0.08 and 0.21 since the FWHM values of butter are considerably higher than the others.

5.5 Human study relaxation time results

The relaxation times of the human study are presented in Table 11 and Table 12. Some relaxation values could not be acquired from all subjects due to bad quality (limits given in chapter 4.10).

Table 11. The T2 relaxation values of human lipid and water signals in BAT and WAT tissues in both cold exposure and warm condition. All values are presented as median (range) and are in ms units.

	S_{0.9}	S_{1.6}+S_{1.3}	S_{2.1}	S_{2.3}	S_{2.8}	S_{2.1}+S_{2.3}+S_{2.8}	Water	S_{5.2}+S_{5.3}
BAT cold (N = 3)	30.38 (22.95– 36.78)	64.09 (59.61– 69.25)	25.33 (19.39– 38.07)	39.77 (18.49– 41.27)	18.12 ^a	33.16 (18.99– 39.89)	25.35 (24.89– 35.66)	38.61 (30.65– 39.93)
BAT warm (N = 4)	25.77 (15.58– 50.94)	62.82 (47.1– 78.13)	32.57 (23.98– 63.89)	38.13 (29.68– 50.02)	34.2 (22.3– 46.11) ^b	33.73 (30.21– 66.03)	30.37 (13.03– 32.25)	33.87 (28.1– 44.08)
WAT cold (N = 3)	35.34 (34.56– 39.9)	85.57 (76.41– 87.34)	43.4 (40.39– 59.68)	38.07 (36.22– 40.6)	48.08 ^a	41.06 (38.69– 48.25)	22.14 (19.34– 22.63)	40.01 (39– 41.03)
WAT warm (N = 4)	37.95 (35.03– 42.78)	86.8 (84.91– 88.14)	55.04 (51.21– 56.4)	44.01 (38.12– 47.69)	50.21 (29.16– 69.6) ^c	49.34 (45.19– 51.22)	24.9 (19.17– 30.12)	44.09 (41.94– 46.2)

^a N = 1; ^b N = 2; ^c N = 3

Table 12. The T1 relaxation values of human lipid and water signals in BAT and WAT tissues in both cold exposure and warm condition. All values are presented as median (range) and are in ms units.

	S_{0.9}	S_{1.6}+S_{1.3}	S_{2.1}	S_{2.3}	S_{2.8}	S_{2.1}+S_{2.3}+S_{2.8}	Water	S_{5.2}+S_{5.3}
BAT cold (N = 2)	188.5 (101.6– 482.5)	198.6 (99.0– 340.7)	197.2 (105.6– 417.8)	145.2 (81.0– 239.1)		157.9 (96.0– 292.2)	149.5 (99.8– 199.2)	104.1 (89.8– 118.3)
BAT warm (N = 3)	145.1 (141.1– 149.1) ^a	119.2 (99.0– 139.5)	120.6 (105.6– 135.5) ^a	87.0 (81.0– 92.9) ^a	117.6 (109.2– 126.0) ^a	105.8 (96.0– 115.6)	208.5 (141.6– 281.7)	248.6 (247.8– 249.4) ^a
WAT cold (N = 3)	145.0 (101.6– 188.5)	136.3 (109.5– 313.0)	164.7 (111.9– 217.6)	153.2 (134.6– 171.8)		126.1 (99.6– 204.2)	253.3 (146.7– 269.8)	302.4 (212.8– 336.7)
WAT warm (N = 4)	337.2 (289.3– 355.7) ^a	226.2 (171.0– 256.7)	243.6 (176.9– 355.4) ^b	145.2 (130.9– 175.0)	250.6 (182.4– 318.8)	193.0 (152.9– 235.0)	252.1 (185.6– 305.7)	424.9 (203.0– 471.0) ^b

^a N = 2; ^b N = 3

5.6 Human study fatty acid characteristics results

The fatty acid characteristics are presented in Table 13 and Table 14 and graphically in Figure 40. The difference in the characteristics between the tissues was significant in f_{pufa} ($p = 0.0303$) and nmidb ($p = 0.0223$) in cold exposure with BAT having less nmidb and thus being less polyunsaturated. In addition and chain length of BAT was longer compared to WAT in cold exposure ($p < 0.0001$). There were some differences in the fatty acid characteristics of BAT between the cold exposure and warm condition: nmidb was smaller in cold exposure than in warm condition ($p = 0.0019$). Therefore, f_{pufa} was also significantly smaller in cold exposure ($p = 0.0022$). In addition, f_{mufa} was significantly greater ($p = 0.0006$) and f_{sfa} significantly smaller ($p = 0.0052$).

in cold exposure. Also the chain length was significantly longer in cold exposure ($p = 0.0450$). WAT tissue had also smaller n_{midb} in cold exposure ($p = 0.0006$) and thus also smaller f_{pufa} ($p = 0.0004$).

In the subject, spectrum and condition adjusted analysis only fatty acid characteristic that differed between the two tissues was chain length ($p = 0.0002$) with BAT having longer chain length. However, when studying the differences of fatty acid characteristics between the two conditions using a subject and spectrum adjusted analysis separately in the two tissues the results were partly in line with the non-adjusted results: n_{db} was higher in cold exposure in both BAT ($p = 0.0007$) and WAT (0.0175). On the contrary, n_{midb} was significantly lower in cold exposure only in BAT ($p = 0.0120$) although the significance in WAT reached borderline level ($p = 0.0639$). The differences in f_{sfa} , f_{mufa} and f_{pufa} between cold exposure and warm conditions were significant in both tissues: f_{sfa} was lower in cold exposure (BAT $p < 0.0001$, WAT $p = 0.0041$), f_{mufa} was higher in cold exposure (BAT $p < 0.0001$, WAT $p = 0.0019$), f_{pufa} was lower in cold exposure (BAT $p = 0.0117$, WAT $p = 0.0491$). The adjusted chain length was surprisingly longer in both tissues in cold exposure compared to warm condition ($p = 0.0002$ for BAT and $p = 0.0070$ for WAT).

Table 13. Fatty acid characteristics in BAT tissue in both cold exposure and warm condition. Values are expressed as median (range).

	BAT cold (N = 18)	BAT warm (N = 26)	P value	Adjusted p value
f_{sfa} (%)	25.0 (-45.0 – 47.0)	41.0 (-3.0 – 72.0)	0.0052	< 0.0001
f_{mufa} (%)	71.5 (52.0 – 134.0)	44.5 (22.0 – 98.0)	0.0006	< 0.0001
f_{pufa} (%)	2.5 (0.0 – 12.0)	7.0 (0.0 – 29.0)	0.0022	0.0117
n_{db}	2.39 (1.59 – 4.69)	2.08 (0.91 – 3.49)	0.0626	0.007
n_{midb}	0.07 (0.00 – 0.35)	0.21 (0.01 – 0.86)	0.0019	0.0120
CL	8.09 (5.15 – 16.14)	6.81 (-1.03 – 11.20)	0.0450	0.0002

Table 14. Fatty acid characteristics in WAT tissue in both cold exposure and warm condition. Values are expressed as median (range).

	WAT cold (N = 32)	WAT warm (N = 39)	P value	Adjusted p value
f_{sfa} (%)	26.5 (6.0 – 71.0)	28.0 (-6.0 – 95.0)	0.4019	0.0041
f_{mufa} (%)	67.5 (21.0 – 91.0)	62.0 (-12.0 – 93.0)	0.1056	0.0019
f_{pufa} (%)	6.0 (1.0 – 14.0)	9.0 (3.0 – 32.0)	0.0004	0.0491
n_{db}	2.45 (1.10 – 3.13)	2.52 (0.34 – 3.54)	0.9355	0.0175
n_{midb}	0.17 (0.02 – 0.43)	0.27 (0.08 – 0.97)	0.0006	0.0639
CL	5.91 (2.00 – 8.43)	5.82 (-1.79 – 9.86))	0.6439	0.0070

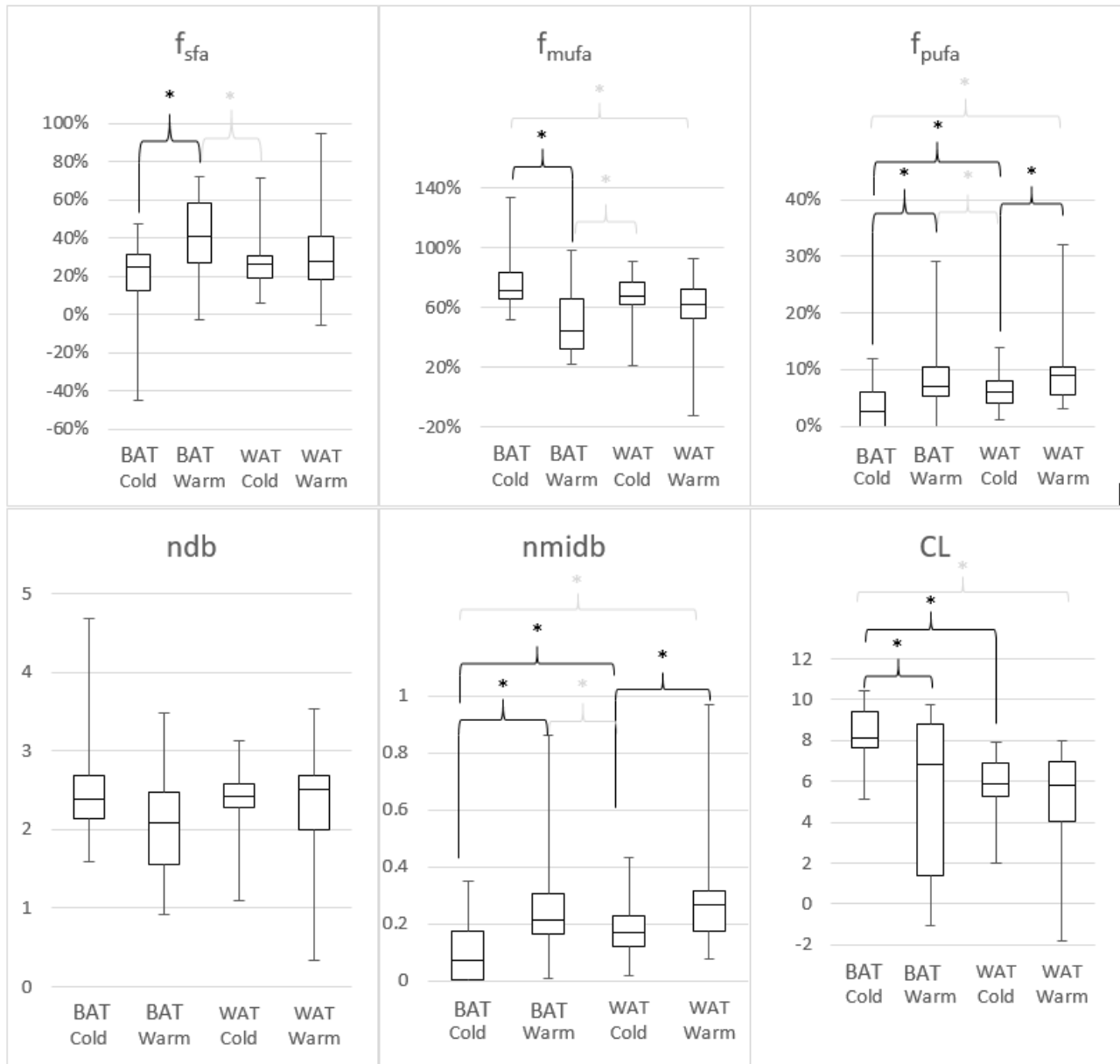


Figure 40. Distributions of f_{sfa} , f_{mufa} , f_{pufa} , ndb and $nmidb$ in BAT and WAT tissues in both cold exposure and warm condition. Significant differences ($p < 0.05$) are marked with *. Significant yet irrelevant differences are colored light grey.

5.7 Human fat fraction results

The fat fractions are presented in Table 15 and graphically in Figure 41. The difference between BAT and WAT tissues was significant in both cold exposure ($p < 0.0001$) and warm condition ($p < 0.0001$). The difference in fat fraction between the two conditions was not statistically significant in either tissue. However, the subject and spectrum adjusted fat fraction values in cold exposure were significantly lower in both tissues ($p = 0.0016$ for BAT and $p = 0.0006$ for WAT).

Table 15. Fat fractions in BAT and WAT tissues in both cold exposure and warm condition. Results expressed as median (range).

	Cold	Warm	p value	Adjusted p value
BAT Fat fraction (%) (N = 24 in cold; N = 38 in warm)	84.5 (77.0 – 90.0)	84.0 (72.0 – 95.0)	0.4506	0.0016
WAT Fat fraction (%) (N = 33 in cold; N = 43 in warm)	90.0 (86.0 – 94.0)	93.0 (78.0 – 97.0)	0.0978	0.0006

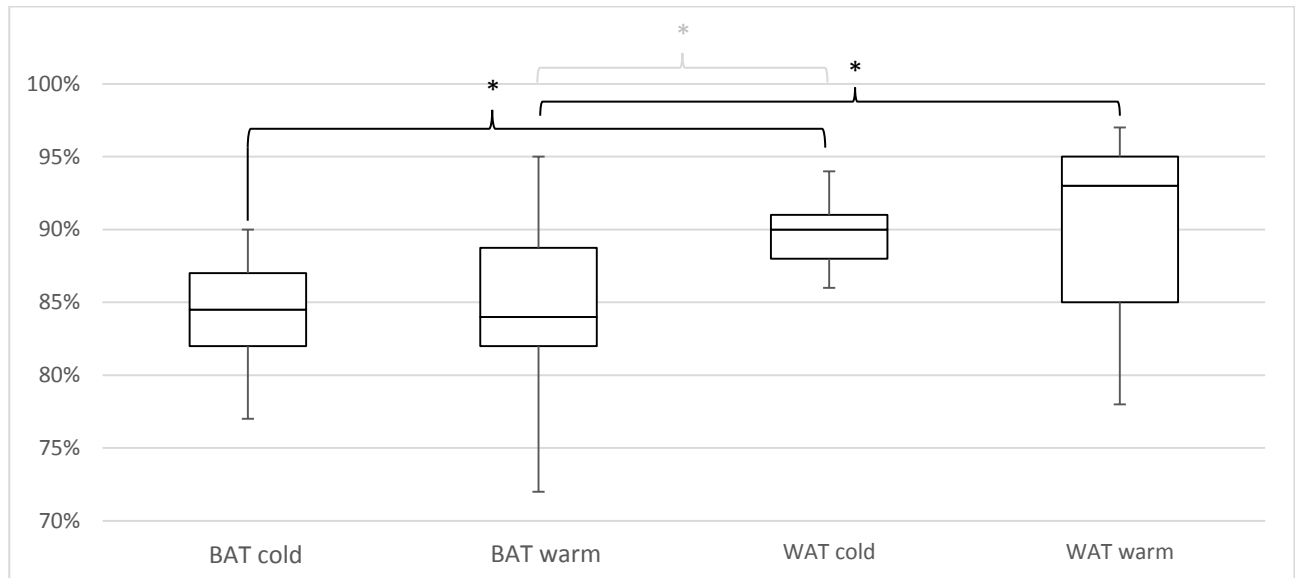


Figure 41. Distributions of fat fractions in BAT and WAT tissues in cold exposure and warm condition. Significant differences ($p < 0.05$) are marked with *. Significant yet irrelevant difference is colored light grey.

6 DISCUSSION

6.1 Phantom study

The phantom validation study gave encouraging results for the ability of ^1H MRS to distinguish various lipid samples from one another based on their fatty acid characteristics. The use of the method for the human in vivo study was especially warranted by the correlations between the measured ndb and nmidb values and the values calculated based on the sample label information (Figure 37). The most accurate results were achieved in butter, MCT oil, palm oil and sunflower oil, all of which are very different in terms of their fatty acid compositions. However, the results for avocado, olive and especially rapeseed oils deviated surprisingly much from their label values. A common property of these samples is that they have the highest fractions of monounsaturated fatty acids. The use of formula (28) required the assumption of the number of double bonds being less than 3. The only one of the samples with significant amount of fatty acids with more than two double bonds was rapeseed oil with 10% linolenic acid content [edible]. This probably explains the greatest nmidb error of rapeseed oil results. Overall, nmidb and thus also f_{pufa} had smallest errors indicating that these parameters can be determined with good confidence. The determination of chain length (CL) appeared to consistently under-estimate the actual value. However, Peterson and Månsson reported a similar behavior in their imaging study [Peterson and Månsson 2013]. They speculate that the estimation of CL might not be as stable as ndb and nmidb estimation.

The range of the fat fraction of butter was less than 2% suggesting a good precision. On the other hand differences smaller than 2% are not likely to be detected reliably using this method, at least not in human studies where several confounding factors exist [Wilson et al. 2019]. The accuracy of the butter fat fraction is difficult to estimate because the label of the sample listed only limited number of ingredients in the butter. When compared against the values given in literature the median fat fraction of 86.5% overshoots the range: 76 – 86% by 0.5% [Kamleh, 2010]. However, the fat fraction given by ^1H MRS is only the fraction of proton densities which correlates with but is not equivalent to mass fat-fraction as all NMR invisible material is missed [Reeder et al 2012]. Thus the “total tissue” of proton density fat fraction is an underestimation of the actual value which explains the overshooting of the result.

The relaxation times were only determined once and hence could not be statistically analyzed. Most of the relaxation values between different samples were within 40% of the median times. However, the values of the smallest signals, T_2 time of $S_{2,8}$ in particular, differed as much as 85% between the samples. This suggest that for accurate relaxation correction individual relaxation times instead of a general value have to be used.

The quality of the phantom spectra was consistent in all samples except the FWHM of butter which was considerably higher than the others. This might be explained by the salt content (1.5%) of the product. Surprisingly, the relaxation times of butter did not seem to differ from the other samples. Despite of the high FWHM the ndb and nmidb errors of butter were among the three smallest.

6.2 Human study

The fatty acid characteristics of WAT in this study are in a good agreement with previous gas chromatography studies [Krut 1964, Bolton-Smith 1997, Lundbom 2010] while previous MRS and NMR studies have found slightly higher values for n_{midb} and thus also for f_{pufa} [Ren 2008, Hamilton 2011]. This is interesting as the phantom validation indicated that these parameters could be determined with best accuracy in this study.

The result of this study suggest that the fatty acid characteristics of BAT and WAT tissues had only little or no difference between each other although the fat fraction was significantly smaller in BAT. Although Hamilton et al found differences between pure brown and pure white adipose tissues [Hamilton et al. 2011], the difference might not be seen in human BAT as it is actually white adipose tissue with a varying number of brown adipocytes within [Rosenwald 2013]. Moreover, the supraclavicular BAT is found to consist primarily of beige adipocytes [Sharp 2012] although recent studies suggest that it is indeed classic BAT which is adjusted to thermoneutral conditions [Cannon et al. 2020]. These might be the reason also for the small difference in fat fraction between BAT and WAT as pure BAT is reported having a fat fraction of 51.5 % [Hamilton et al. 2011].

The most interesting result of this study was that cold exposure seems to affect the fatty acid characteristics of BAT and WAT tissues differently: in BAT the fractions of SFA and PUFA decreased in cold exposure while the fraction of MUFA increased. This indicates that the intracellular saturated and polyunsaturated fatty acids are consumed during cold exposure in BAT. The reduction seems to be compensated by the uptake of monounsaturated fatty acids. On contrary, the only change between room temperature and cold exposure in WAT was the reduction of the fraction of PUFA which occurs also in BAT. This suggests that the cold-induced lipolysis in WAT affects only the polyunsaturated fatty acids. Even so, this might have clinical importance as familial longevity has been associated with high MUFA/PUFA ratio of blood serum in a human study [Gonzalez-Covarrubias et al. 2013] and also in an animal study [Shmookler Reis et al. 2011]. Thus promoting the activation of PUFA consuming BAT might have a positive effect on longevity. In addition it can be speculated that BAT improves metabolic health by the increased clearance of SFA as the low concentration of SFA in tissues is associated to good insulin sensitivity [Vessby et al. 2002].

These results are partly in line with previous studies: In a mass spectrometry-based lipidomics animal study by Xu et al the ratio of the fractions of MUFA and PUFA was found to increase in cold exposure and the fraction of PUFA was found to decrease while the other fatty acid characteristics remained unchanged in WAT [Xu et al]. In an ex-vivo NMR study the number of both saturated and unsaturated fatty acids in mouse BAT and WAT started to decrease already 2 hours after the onset of cold exposure and lasted up to 6 hours in BAT and 4 hours in WAT. [Lu et al 2016]

Although the cold exposure appeared to alter the fatty acid characteristics of the tissues, it did not seem to have an effect on the fat fraction. However, the p value of the difference in WAT fat fraction between the conditions was borderline significant. This is surprising as the fatty acid characteristics appeared to change more in BAT.

This may not be explained by increased perfusion or triglyceride clearance which should be more prominent in BAT tissue [Orava et al 2011; Bartelt et al 2011]. The 3% reduction in the fat fraction is very close to the 2% precision limit suggested by the phantom experiment. Therefore nothing conclusive can be said based on difference this small and with just borderline significance.

Chain length parameter is problematic due to its imprecise results in the phantom experiment. Moreover, the measured chain lengths in the human study are less than half of literature values [Krut 1964, Bolton-Smith 1997, Lundbom 2010]. The longer chain length in BAT in cold exposure however is in line with previous research [Tan et al. 2015]. Tan et al. described the action of fatty acid elongate gene Elovl6 which initiates the conversion of saturated and monounsaturated C16 fatty acids to C18 fatty acids during activation of BAT. Further studies are needed to establish precise determination of fatty acid chain length from MRS data.

No statistical analysis could be performed on the relaxation values in the human study. However, the values seem to differ between BAT and WAT. In a previous MR imaging study the T2* relaxation values were found to differ between the tissues [Holstila et al. 2017]. However, Hamilton et al noticed only negligible differences in their tissue sample study [Hamilton et al. 2011]. Further studies are needed to confirm the difference, especially for T1 relaxation time. To the knowledge of the author of this thesis this is the first time relaxation times have been determined from human in vivo BAT and WAT. Therefore the human relaxation values cannot be compared to similar studies. However the T2 values were surprisingly close to the ex-vivo T2 values measured by Hamilton et al. In contrast, the T1 values of this study were shorter than the values in the Hamilton et al study as can be expected. [Hamilton et al. 2011]

7 LIMITATIONS

Only four subjects participated the human study. To overcome this, the “subject” variable was treated as a covariate in the statistical analysis. A further limiting factor was that the cold exposure was not performed for one of the subjects.

Another limitation is the possible localization error of the spectroscopic voxel in the supraclavicular adipose tissue where muscle and fat tissues are close to each other. By placing the voxel partially in a muscle results in erroneously high water content and thus white fat can be mistaken as brown. Even though the voxel would have been placed carefully in the fat the possible movement of the patient might potentially corrupt the localization. In WAT the erroneous location of the voxel is relatively easy to notice due to the inherently low water content of the tissue. In practice, if the water content of WAT seems to be high one can suspect that the voxel is in faulty position.

A minor limitation was that the number of data points was not the same in the human and phantom studies. The lower number of sampled data points (1024) is the default value of ^1H MRS protocols on Philips MRI scanners and it was accidentally left unchanged in the human study. This however does not have any major effect on the data quality as most of the added data points represent only the noise after the decayed FID signal.

The phantom study was lacking actual repetitive measurements which would have increased the statistical power. In this study the relaxation values were determined only once for each sample. The statistical power was increased artificially in both human and phantom study by analyzing the individual spectra in the relaxation time measurement series as well.

The T2 relaxation time measurement in this study was conducted by using only 5 different echo times. If no schedule limitations existed, much more echo times could have been used to determine the T2 values more precisely. Multiple echo times would have allowed the correction for J coupling effects which occur as a sinusoidal modulation of the exponential signal decay. Furthermore, the TE times were chosen to range from 15 to 75 ms which is considerably longer than Hamilton et al used (13 – 33 ms) in order to minimize J-coupling effect [Hamilton et al. 2011]. Thus the T2 times of this study might be compromised by J-coupling phenomenon more than those of Hamilton.

8 CONCLUSIONS

This study shows that fatty acid characteristics of human supraclavicular and subcutaneous adipose tissues can be determined on a clinical MRI scanner although the method is relatively insensitive and thus requires high number of study subjects. However, measuring fatty acid characteristics provides new possibilities for adipose tissue research in Turku University Hospital as the method provides new insights into the physiology of adipose tissue. The new PET-MRI device in Turku PET Centre allows simultaneous measurement of PET and MRI or MRS. With this system an interesting study scheme would be a medical activation of subject's BAT and simultaneous following of the uptake of ^{18}F -FDG or other PET-tracers and change in fatty acid characteristics. This could provide comprehensive new knowledge of the function of BAT during activation.

The results of this study suggest that fatty acid metabolism during cold exposure differs between the two tissues. The observed increase of MUFA and decrease of PUFA in BAT warrants the clinical use of promoting BAT activation as a high MUFA/PUFA ratio has been associated with longevity in previous studies. In addition, the results support the previous findings of the beneficial effect of BAT on metabolic health as the clearance of SFA was found to increase in BAT during cold activation. Thus the tissue might "clean" the body from excess SFA.

Changes in fatty acid characteristics can be seen before the fat fraction has changed suggesting that fatty acid characteristics are more sensitive parameters for detection of active BAT. This warrants for re-analysis of previously measured BAT and WAT spectra in which the primary variable so far has been fat fraction. However, the great variability of the results suggests that a high number of data is needed before conclusive findings can be made.

9 ACKNOWLEDGEMENTS

This study was carried out at the Turku PET Centre, University of Turku and Turku University Hospital and was funded by personal grants from Turku University Foundation and Instrumentarium Science Foundation.

I wish to express my deepest gratitude to my supervisors: assistant chief physicist Jani Saunavaara and professor Riitta Parkkola for their excellent guidance throughout the years. I also want to thank Professor Petriina Paturi for helping me sort out the practical matters of licentiate's degree and also for reviewing this thesis together with Riitta and Jani.

Docents Sven Månsson and Sergey Vasiliev, thank you so much for reviewing my thesis and giving valuable feedback.

I am very grateful to professors Pirjo Nuutila and Kirsi Virtanen for the opportunity to join brown adipose tissue research and I also want to thank Kirsi for commenting this thesis and giving excellent feedback.

Doctor Juho Raiko was the original primus motor of BAT follow-up project. Without his hard work the data for this thesis would not have been collected. He has also been a great medical consultant and always quick to reply my questions about various physiological issues not familiar to a physicist. Juho, please accept my deepest thanks.

I want to thank statistician, geologist and my long-time friend Niko Tanski for his assistance in the statistics of this study.

Finally, I want to thank my dearest family, my parents Anneli and Kari, my wife Päivi and our daughters Kerttu and Elina for their support, understanding, love and prayers during ups and downs of life.

10 REFERENCES

- [Admiraal et al. 2013] Admiraal WM, Holleman F, Bahler L, Soeters MR, Hoekstra JB, Verberne HJ. Combining 123I-metaiodobenzylguanidine SPECT/CT and 18F-FDG PET/CT for the assessment of brown adipose tissue activity in humans during cold exposure. *J Nucl Med.* 2013;54:208–212.
- [Ahmadian et al 2007] Ahmadian M, Duncan RE, Jaworski K, Sarkadi-Nagy E, Sul HS. Triacylglycerol metabolism in adipose tissue. *Future Lipidol.* 2007;2(2):229–237.
- [Alexander et al. 2015] Alexander CM, Kasza I, Yen CL, Reeder SB, Hernando D, Gallo RL, Jahoda CA, Horsley V, MacDougald OA. Dermal white adipose tissue: a new component of the thermogenic response. *J Lipid Res.* 2015;56(11):2061–2069
- [Ang et al. 2017] Ang QY, Goh HJ, Cao Y, Li Y, Chan SP, Swain JL, Henry CJ, Leow MK. A new method of infrared thermography for quantification of brown adipose tissue activation in healthy adults (TACTICAL): a randomized trial. *J Physiol Sci.* 2017;67(3):395–406.
- [Baba et al. 2007] Baba S, Engles JM, Huso DL, Ishimori T, Wahl RL. Comparison of uptake of multiple clinical radiotracers into brown adipose tissue under cold-stimulated and nonstimulated conditions. *J Nucl Med.* 2007;48:1715–1723.
- [Baba et al. 2010] Baba S, Jacene HA, Engles JM, Honda H, Wahl RL. CT Hounsfield units of brown adipose tissue increase with activation: preclinical and clinical studies. *J Nucl Med.* 2010;51(2):246–250.
- [Barquissau et al. 2016] Barquissau V, Beuzelin D, Pisani DF, Beranger GE, Mairal A, Montagner A, Roussel B, Tavernier G, Marques MA, Moro C, Guillou H, Amri EZ, Langin D. White-to-brite conversion in human adipocytes promotes metabolic reprogramming towards fatty acid anabolic and catabolic pathways. *Mol Metab.* 2016;5(5):352–365.
- [Barrington and Maisey 1996] Barrington SF, Maisey MN. Skeletal muscle uptake of fluorine-18-FDG: effect of oral diazepam. *J Nucl Med* 1996;37:1127–1129.
- [Bartelt et al 2011] Bartelt A, Bruns OT, Reimer R, Hohenberg H, Ittrich H, Peldschus K, Kaul MG, Tromsdorf UI, Weller H, Waurisch C, Eychmüller A, Gordts PL, Rinninger F, Bruegelmann K, Freund B, Nielsen P, Merkel M, Heeren J. Brown adipose tissue activity controls triglyceride clearance. *Nat Med.* 2011;17(2):200–205.
- [Basu et al. 2011] Basu S, Kwee TC, Surti S, Akin EA, Yoo D, Alavi A. Fundamentals of PET and PET/CT imaging. *Ann N Y Acad Sci.* 2011;1228:1–18.
- [Bauwens et al. 2014] Bauwens M, Wierts R, van Royen B, Bucerius J, Backes W, Mottaghy F, Brans B. Molecular imaging of brown adipose tissue in health and disease. *Eur J Nucl Med Mol Imaging.* 2014;41(4):776–791.

- [Beare-Rogers et al. 2001] Beare-Rogers J, Dieffenbacher A and Holm JV. Lexicon of lipid nutrition (IUPAC Technical Report). *Pure Appl. Chem.* 2001;73(4):685–744.
- [Berbée et al. 2015] Berbée JF, Boon MR, Khedoe PP, Bartelt A, Schlein C, Worthmann A, Kooijman S, Hoeke G, Mol IM, John C, Jung C, Vazirpanah N, Brouwers LP, Gordts PL, Esko JD, Hiemstra PS, Havekes LM, Scheja L, Heeren J, Rensen PC. Brown fat activation reduces hypercholesterolaemia and protects from atherosclerosis development. *Nat Commun.* 2015;6:6356.
- [Bloch et al. 1946] Bloch F, Hansen WW, Packard M. Nuclear Induction. *Phys Rev.* 1946;69:127
- [Blondin et al. 2017a] Blondin DP, Frisch F, Phoenix S, Guérin B, Turcotte ÉE, Haman F, Richard D, Carpentier AC. Inhibition of intracellular triglyceride lipolysis suppresses cold-induced brown adipose tissue Metabolism and Increases Shivering in Humans. *Cell Metab.* 2017;25(2):438–447
- [Bolsoni-Lopes and Alonso-Vale 2015] Bolsoni-Lopes A, Alonso-Vale MI. Lipolysis and lipases in white adipose tissue - An update. *Arch Endocrinol Metab.* 2015;59(4):335–342.
- [Bolton-Smith 1997] Bolton-Smith C, Woodward M, Tavendale R. Evidence for age-related differences in the fatty acid composition of human adipose tissue, independent of diet. *Eur J Clin Nutr.* 1997;51(9):619–624.
- [Bonora et al. 2012] Bonora M, Patergnani S, Rimessi A, De Marchi E, Suski JM, Bononi A, Giorgi C, Marchi S, Missiroli S, Poletti F, Wieckowski MR, Pinton P. ATP synthesis and storage. *Purinergic Signal.* 2012;8(3):343–357
- [Buckingham 1960] Buckingham AD. Chemical shifts in the nuclear magnetic resonance spectra of molecules containing polar groups. *Can J Chem.* 1960;38:300–307.
- [Calder 2015] Calder PC. Functional roles of fatty acids and their effects on human health. *JPEN J Parenter Enteral Nutr.* 2015;39(1 Suppl):18S–32S.
- [Calderon-Dominguez et al. 2016] Calderon-Dominguez M, Mir JF, Fucho R, Weber M, Serra D, Herrero L. Fatty acid metabolism and the basis of brown adipose tissue function. *Adipocyte.* 2015;10;5(2):98–118.
- [Cannon et al. 2020]. Cannon B, de Jong JMA, Fischer AW, Nedergaard J, Petrovic N. Human brown adipose tissue: Classical brown rather than brite/beige? *Experimental Physiology.* 2020;105:1191–1200.
- [Carovac et al. 2011] Carovac A, Smajlovic F, Junuzovic D. Application of ultrasound in medicine. *AIM* 2011;19(3):168–171
- [Chen et al. 2016] Chen KY, Cypess AM, Laughlin MR, Haft CR, Hu HH, Bredella MA, Enerbäck S, Kinahan PE, Lichtenbelt Wv, Lin FI, Sunderland JJ, Virtanen KA, Wahl RL. Brown Adipose Reporting Criteria in Imaging Studies (BARCIST 1.0): Recommendations for standardized FDG-PET/CT experiments in humans. *Cell Metab.* 2016;24(2):210–222

- [Chondronikola et al. 2017] Chondronikola M, Beeman SC, Wahl RL. Non-invasive methods for the assessment of brown adipose tissue in humans. *J Physiol.* 2018;596(3):363–378.
- [Cinti 2011] Cinti S. Between brown and white: Novel aspects of adipocyte differentiation. *Annals of Medicine.* 2011;43:104–115.
- [Cohade et al 2003a] Cohade C, Mourtzikos KA, Wahl RL. "USA-Fat": prevalence is related to ambient outdoor temperature-evaluation with 18F-FDG PET/CT. *J Nucl Med.* 2003;44(8):1267–1270.
- [Cohade et al 2003b] Cohade C, Osman M, Pannu HK, Wahl RL. Uptake in supraclavicular area fat ("USA-Fat"): description on 18F-FDG PET/CT. *J Nucl Med.* 2003;44(2):170–176.
- [Conway and Rene 2004] Conway B, Rene A. Obesity as a disease: no lightweight matter. *Obes Rev.* 2004;5(3):145–151.
- [Cypess and Kahn 2012] Cypess AM, Kahn CR. Brown fat as a therapy for obesity and diabetes. *Curr Opin Endocrinol Diabetes Obes.* 2010 Apr;17(2):143–149.
- [Cypess et al. 2009] Cypess AM, Lehman S, Williams G, Tal I, Rodman D, Goldfine AB, Kuo FC, Palmer EL, Tseng YH, Doria A, Kolodny GM, Kahn CR. Identification and importance of brown adipose tissue in adult humans. *N Engl J Med* 2009; 360(15):1509–1517
- [Cypess et al. 2013] Cypess AM, Doyle AN, Sass CA, Huang TL, Mowschenson PM, Rosen HN, Tseng YH, Palmer EL 3rd, Kolodny GM. Quantification of human and rodent brown adipose tissue function using 99mTc-methoxyisobutylisonitrile SPECT/CT and 18F-FDG PET/CT. *J Nucl Med.* 2013;54(11):1896–1901.
- [Cypess et al. 2015] Cypess AM, Weiner LS, Roberts-Toler C, Franquet Elía E, Kessler SH, Kahn PA, English J, Chatman K, Trauger SA, Doria A, Kolodny GM. Activation of human brown adipose tissue by a β 3-adrenergic receptor agonist. *Cell Metab.* 2015;21(1):33–38.
- [Dai et al. 2015] Dai W, Weines L, Alsop D, Cypess A, editors. Feasibility repeatability of brown adipose tissue volume perfusion activity using MRI. In: *Proceedings of 23rd Int Society for Magnetic Resonance in Medicine.* Toronto, ON. 2015.
- [Deng et al. 2015] Deng J, Schoeneman SE, Zhang H, Kwon S, Rigsby CK, Shore RM, Josefson JL. MRI characterization of brown adipose tissue in obese and normal-weight children. *Pediatr Radiol.* 2015;45(11):1682–1689
- [Desbois and Smith 2009] Desbois AP and Smith VJ. Antibacterial free fatty acids: activities, mechanisms of action and biotechnological potential. *Appl Microbiol Biotechnol.* 2010; 85:1629–1642
- [Dieckmeyer et al. 2017] Dieckmeyer M, Ruschke S, Eggers H, Kooijman H, Rummeny EJ, Kirschke JS, Baum T, Karampinos DC. ADC quantification of the vertebral bone marrow water component: removing the confounding effect of residual fat. *Magn Reson Med.* 2017;78(4):1432–1441.

- [Dixon and Ekstrand 1982] Dixon RL and Ekstrand KE. The physics of proton NMR. *Med Phys*. 1982;9(6):807–818.
- [Dixon 1984] Dixon WT. Simple proton spectroscopic imaging. *Radiology*. 1984;153(1):189-94.
- [Duncan et al. 2007] Robin E. Duncan, Maryam Ahmadian, Kathy Jaworski, Eszter Sarkadi-Nagy, and Hei Sook Sul. Regulation of lipolysis in adipocytes. *Annu Rev Nutr*. 2007; 27:79–101.
- [Engel et al 1996] Engel H, Steinert H, Buck A, Berthold T, Huch Boni RA, von Schulthess GK. Whole-body PET: physiological and artifactual fluorodeoxyglucose accumulations. *J Nucl Med* 1996;37:441–446.
- [Erns and Anderson 1966] Ernst RR, Anderson WA. Application of Fourier transform spectroscopy to magnetic resonance. *Rev Sci Instrum*. 1966;37(1):93–102.
- [Fedorenko et al. 2012]. Fedorenko A, Lishko PV and Kirichok Y. Mechanism of fatty-acid-dependent UCP1 uncoupling in brown fat mitochondria. *Cell*. 2012;151(2):400–413.
- [Flores et al. 2019] Flores M, Saravia C, Vergara CE, Avila F, Valdés H, Ortiz-Viedma J. Avocado oil: characteristics, properties, and applications. *Molecules*. 2019;24(11):2172.
- [Flynn et al. 2015] Flynn A, Li Q, Panagia M, Abdelbaky A, MacNabb M, Samir A, Cypess AM, Weyman AE, Tawakol A, Scherrer-Crosbie M. Contrast-enhanced ultrasound: a novel noninvasive, nonionizing method for the detection of brown adipose tissue in humans. *J Am Soc Echocardiogr*. 2015;28(10):1247–1254.
- [Frankl et al. 2019] Frankl J, Sherwood A, Clegg DJ, Scherer PE, Öz OK. Imaging metabolically active fat: A literature review and mechanistic insights. *Int J Mol Sci*. 2019 Nov 5;20(21):5509.
- [Franssens et al. 2017] Franssens BT, Hoogduin H, Leiner T, van der Graaf Y, Visseren FLJ. Relation between brown adipose tissue and measures of obesity and metabolic dysfunction in patients with cardiovascular disease. *J Magn Reson Imaging*. 2017;46(2):497–504.
- [Franz et al. 2015] Franz D, Karampinos DC, Rummeny EJ, Souvatzoglou M, Beer AJ, Nekolla SG, Schwaiger M, Eiber M. Discrimination between brown and white adipose tissue using a 2-point dixon water-fat separation method in simultaneous PET/MRI. *J Nucl Med*. 2015;56(11):1742–1747.
- [Fukuchi et al. 2003] Fukuchi K, Ono Y, Nakahata Y, Okada Y, Hayashida K, Ishida Y. Visualization of interscapular brown adipose tissue using (99m)Tc-tetrofosmin in pediatric patients. *J Nucl Med*. 2003;44(10):1582–1585.
- [Garroway et al. 1974] Garroway AN, Grannell PK, Mansfield P. Image formation in NMR by a selective irradiative process. *J Phys C: Solid State Phys* 1974;7:L457–462.

- [Gerngroß et al. 2017] Gerngroß C, Schretter J, Klingenspor M, Schwaiger M, Fromme T. Active brown fat during 18F-FDG PET/CT imaging defines a patient group with characteristic traits and an increased probability of brown fat redetection. *J Nucl Med.* 2017;58(7):1104–1110.
- [Gesner 1551] Conradi Gesneri medici Tigurine Historiae Animalium: Lip. I De Quadrupedibus viviparis 1551.
- [Gibby 2005] Gibby WA. Basic principles of magnetic resonance imaging. *Neurosurg Clin N Am.* 2005;16:1–64.
- [Gifford et al. 2016] Gifford A, Towse TF, Walker RC, Avison MJ, Welch EB. Characterizing active and inactive brown adipose tissue in adult humans using PETCT and MR imaging. *Am J Physiol Endocrinol Metab.* 2016;311:E95–104.
- [Gonzalez-Covarrubias et al. 2013] Gonzalez-Covarrubias V, Beekman M, Uh HW, Dane A, Troost J, Paliukhovich I, van der Kloet FM, Houwing-Duistermaat J, Vreeken RJ, Hankemeier T, Slagboom EP. Lipidomics of familial longevity. *Aging Cell.* 2013;12(3):426–34.
- [Gupta et al. 2015] Gupta A, Stait-Gardner T, Moghaddam MJ and Price WS. Dipolar relaxation revisited: a complete derivation for the two spin case. *Concepts magn reso A.* 2015;44A(2) 74–113
- [Hall et al. 2017] Hall J, Jeggo PA, West C, Gomolka M, Quintens R, Badie C, Laurent O, Aerts A, Anastasov N, Azimzadeh O, Azizova T, Baatout S, Baselet B, Benotmane MA, Blanchardon E, Guéguen Y, Haghdoost S, Harms-Ringhdahl M, Hess J, Kreuzer M, Laurier D, Macaeva E, Manning G, Pernot E, Ravanat JL, Sabatier L, Tack K, Tapio S, Zitzelsberger H, Cardis E. Ionizing radiation biomarkers in epidemiological studies - An update. *Mutat Res.* 2017;771:59–84.
- [Hamilton et al. 2011] Hamilton G, Smith DL Jr, Bydder M, Nayak KS, Hu HH. MR properties of brown and white adipose tissues. *J Magn Reson Imaging.* 2011;34(2):468–473.
- [Hanson 2008] Hanson LG. Is Quantum Mechanics necessary for understanding Magnetic Resonance? *Concept Magn Reson A.* 2008;32A(5):329–340.
- [Hany et al 2002] Thomas F. Hany, Esmail Gharehpapagh, Ehab M. Kamel, Alfred Buck, Jean Himms-Hagen, Gustav K. von Schulthess. Brown adipose tissue: a factor to consider in symmetrical tracer uptake in the neck and upper chest region. *Eur J Nucl Med (2002) 29:1393–1398.*
- [Hatai 1902] Hatai S. On the presence in human embryos of an interscapular gland corresponding to the so-called hibernating gland of lower mammals. *Anat Anzeiger.* 1902;21:369–373.
- [Heaton 1972] Heaton JM. The distribution of brown adipose tissue in the human. *J. Anat.* 1972;112:35–39.
- [Hoeke et al. 2016] Hoeke G, Kooijman S, Boon MR, Rensen PC, Berbée JF. Role of brown fat in lipoprotein metabolism and atherosclerosis. *Circ Res.* 2016;118(1):173–182.

- [Holstila et al. 2013] Holstila M, Virtanen KA, Grönroos TJ, Laine J, Lepomäki V, Saunavaara J, Lisinen I, Komu M, Hannukainen JC, Nuutila P, Parkkola R, Borra RJ. Measurement of brown adipose tissue mass using a novel dual-echo magnetic resonance imaging approach: a validation study. *Metabolism*. 2013;62(8):1189–1198.
- [Holstila et al. 2017] Holstila M, Pesola M, Saari T, Koskensalo K, Raiko J, Borra RJH, Nuutila P, Parkkola R, Virtanen KA. MR Signal- fat- fraction analysis and T2* weighted imaging measure BAT reliably on humans without cold exposure. *metabolism*. 2017;70(5):23–30.
- [Hu et al 2013] Hu HH, Yin L, Aggabao PC, Perkins TG, Chia JM, Gilsanz V. Comparison of brown and white adipose tissues in infants and children with chemical-shift-encoded water-fat MRI. *J Magn Reson Imaging*. 2013;38:885–896.
- [Huttunen et al 1981] Huttunen P, Hirvonen J, Kinnula V. The occurrence of brown adipose tissue in outdoor workers. *Eur J Appl Physiol Occup Physiol*. 1981;46(4):339–345.
- [Ibrahim 2010] Ibrahim MM. Subcutaneous and visceral adipose tissue: structural and functional differences. *Obes Rev*. 2010 Jan;11(1):11–18.
- [Institute of Shortening and Edible Oils 2016] Food fats and oils. Institute of Shortening and Edible Oils. 1319 F Street NW, Suite 600 Washington, DC 20004. 10th edition. 2016.
- [Ishibashi and Seale 2010] Ishibashi J, Seale P. Medicine. Beige can be slimming. *Science*. 2010 May 28;328(5982):1113–1114.
- [Jaszczak et al. 1980]. Jaszczak RJ, Coleman RE, Lim CB. SPECT: Single photon emission computed tomography. *IEEE Trans Nucl Sci*. 1980;NS-27(3):1137–1153.
- [Kalender 2006] Kalender WA. X-ray computed tomography. *Phys Med Biol*. 2006;51(13):R29–43.
- [Kamleh, 2010]. Kamleh R, Fanni J, Mayda EE. Composition and rheological properties of butter produced in Bekaa Valley (Libanon). *J Food Agric Environ*. 2010;8:186–189.
- [Katan et al. 1997] Katan MB, Deslypere JP, van Birgelen AP, Penders M, Zegwaard M. Kinetics of the incorporation of dietary fatty acids into serum cholesteryl esters, erythrocyte membranes, and adipose tissue: an 18-month controlled study. *J Lipid Res*. 1997;38(10):2012–2022.
- [Kereshaw and Flier 2004] Kershaw EE, Flier JS. Adipose tissue as an endocrine organ. *J Clin Endocrinol Metab*. 2004;89(6):2548–2556.
- [Khanna and Branca 2012] Khanna A, Branca RT. Detecting brown adipose tissue activity with BOLD MRI in mice. *Magn Reson Med*. 2012;68:1285–1290.

- [Khedoe et al. 2015] Khedoe PP, Hoeke G, Kooijman S, Dijk W, Buijs JT, Kersten S, Havekes LM, Hiemstra PS, Berbée JF, Boon MR, Rensen PC. Brown adipose tissue takes up plasma triglycerides mostly after lipolysis. *J Lipid Res.* 2015;56(1):51–59.
- [Koskensalo et al. 2017] Koskensalo K, Raiko J, Saari T, Saunavaara V, Eskola O, Nuutila P, Saunavaara J, Parkkola R and Virtanen KA. Human brown adipose tissue temperature and fat fraction are related to its metabolic activity. *J Clin Endocrinol Metab.* 2017;102(4):1200–1207.
- [Krut 1964] Krut LH, Bronte-Stewart B. The fatty acids of human depot fat. *J Lipid Res.* 1964;5(3):343–351.
- [Labbé et al. 2015] Labbé SM, Caron A, Bakan I, Laplante M, Carpentier AC, Lecomte R, Richard D. In vivo measurement of energy substrate contribution to cold-induced brown adipose tissue thermogenesis. *Faseb J.* 2015;29(5):2046–2058.
- [Laplante et al. 2008], Laplante M, Festuccia WT, Soucy G, Blanchard PG, Renaud A, Berger JP, Olivecrona G, Deshaies Y. Tissue-specific postprandial clearance is the major determinant of PPARgamma-induced triglyceride lowering in the rat. *Am J Physiol Regul Integr Comp Physiol.* 2009;296(1):R57–66
- [Laposata 1995] Laposata M. Fatty acids. Biochemistry to clinical significance. *Am J Clin Pathol.* 1995; 104(2):172–179.
- [Lauterbur 1973] Lauterbur PC. Image formation by induced local interactions: examples employing nuclear magnetic resonance. *Nature.* 1973;242:190–191.
- [LCModel_manual] Provencher S. LCModel & LCMgui user’s manual. May 27, 2020.
- [Lehner and Kukis 1996] Lehner R, Kuksis A. Biosynthesis of triacylglycerols. *Prog Lipid Res.* 1996;35(2):169–201.
- [Lindell 2013] Lidell ME, Betz MJ, Dahlqvist Leinhard O, Heglind M, Elander L, Slawik M, Mussack T, Nilsson D, Romu T, Nuutila P, Virtanen KA, Beuschlein F, Persson A, Borga M, Enerbäck S. Evidence for two types of brown adipose tissue in humans. *Nat Med.* 2013;19(5):631–634.
- [Liu et al.] Liu S, Zhang R, Zheng Z, Zheng Y. Electromagnetic-acoustic sensing for biomedical applications. *Sensors (Basel).* 2018;18(10):3203.
- [Ljungberg 2018] Ljungberg M. Absolute quantitation of SPECT studies. *Semin Nucl Med* 2018;48(4):348–358.
- [Ljunggren 1983] Ljunggren Stig. A simple graphical representation of Fourier-based imaging methods. *JMR* 1983;54:338–343.
- [Lowe and Norberg 1957] Lowe IJ, Norberg RE. Free-induction decays in solids. *Phys Rev.* 1957;107(1):46–61.

- [Lu et al 2016] Lu X, Solmonson A, Lodi A, Nowinski SM, Sentandreu E, Riley CL, Mills EM, Tiziani S. The early metabolomic response of adipose tissue during acute cold exposure in mice. *Sci Rep*. 2017;7(1):3455
- [Lunati et al 2001] Lunati E, Farace P, Nicolato E, Righetti C, Marzola P, Sbarbati A and Osculati F. Polyunsaturated fatty acids mapping by H-1 MR-chemical shift imaging. *Magn Reson Med*. 2001; 46(5):879–883.
- [Lundbom 2010] Lundbom J, Hakkarainen A, Fielding B, Söderlund S, Westerbacka J, Taskinen MR, Lundbom N. Characterizing human adipose tissue lipids by long echo time 1H-MRS in vivo at 1.5 Tesla: validation by gas chromatography. *NMR Biomed*. 2010;23(5):466–472
- [Lundbom 2016] Lundbom J, Bierwagen A, Bodis K, Szendrödi J, Kaprio J, Rissanen A, Lundbom N, Roden M, Pietiläinen KH. Deep subcutaneous adipose tissue lipid unsaturation associates with intramyocellular lipid content. *Metabolism*. 2016;65(9):1230–1237
- [Lundström et al. 2015] Lundström E, Strand R, Johansson L, Bergsten P, Ahlström H, Kullberg J. Magnetic resonance imaging cooling-reheating protocol indicates decreased fat fraction via lipid consumption in suspected brown adipose tissue. *PLoS ONE*. 2015;10:e0126705.
- [Mansfield and Maudsley 1977] Mansfield P and Maudsley AA. Planar spin imaging by NMR. *JMR*. 1977;27(1):101–119.
- [Mlynárik 2017] Mlynárik V. Introduction to nuclear magnetic resonance. *Anal Biochem*. 2017;529:4–9.
- [Moss 1996] Basic Terminology of stereochemistry (IUPAC Recommendations 1996). *Pure Appl. Chem*. 1996; 68(12):2193–2222
- [Moss et al 1995]. Moss, G. P., Smith, P. S., & Tavernier, D. (1995). Glossary of class names of organic compounds and reactivity intermediates based on structure (IUPAC Recommendations 1995), *Pure and Applied Chemistry*, 67(8-9), 1307–1375.
- [Moura et al. 2005] Moura MA, Festuccia WT, Kawashita NH, Garófalo MA, Brito SR, Kettelhut IC, Migliorini RH. Brown adipose tissue glyceroneogenesis is activated in rats exposed to cold. *Pflugers Arch*. 2005;449(5):463–469.
- [Muzik et al. 2012] Muzik O, Mangner TJ, Granneman JG. Assessment of oxidative metabolism in brown fat using PET imaging. *Front Endocrinol (Lausanne)*. 2012;3:15.
- [Muzik et al. 2013] Muzik O, Mangner TJ, Leonard WR, Kumar A, Janisse J, Granneman JG. 15O PET measurement of blood flow and oxygen consumption in cold-activated human brown fat. *J Nucl Med*. 2013;54(4):523–531
- [Nedergaard et al 2007] Nedergaard J, Bengtsson T, Cannon B. Unexpected evidence for active brown adipose tissue in adult humans. *Am J Physiol Endocrinol Metab* 2007;293:E444–452

- [Nelson et al. 2000]. Nelson TL, Vogler GP, Pedersen NL, Hong Y and Miles TP Genetic and environmental influences on body fat distribution, fasting insulin levels and CVD: are the influences shared? *Twin Res.* 2000;3:43–50.
- [Nirengi et al. 2015] Nirengi S, Yoneshiro T, Sugie H, Saito M, Hamaoka T. Human brown adipose tissue assessed by simple, noninvasive near-infrared time-resolved spectroscopy. *Obesity (Silver Spring).* 2015;23(5):973–980
- [Ong et al. 2018] Ong FJ, Ahmed BA, Oreskovich SM, Blondin DP, Haq T, Konyer NB, et al. Recent advances in the detection of brown adipose tissue in adult humans: a review. *Clin Sci.* 2018; 132:1039–1054.
- [Orava et al 2011] Orava J, Nuutila P, Lidell ME, Oikonen V, Nojonen T, Viljanen T, Scheinin M, Taittonen M, Niemi T, Enerbäck S, Virtanen KA. Different metabolic responses of human brown adipose tissue to activation by cold and insulin. *Cell Metab.* 2011;14(2):272–279
- [Oreskovich et al. 2019] Oreskovich SM, Ong FJ, Ahmed BA, Konyer NB, Blondin DP, Gunn E, et al. MRI reveals human brown adipose tissue is rapidly activated in response to cold. *J Endocr Soc.* 2019;3:2374–2384.
- [Osuna-Prieto et al 2018] Osuna-Prieto FJ, Martinez-Tellez B, Sanchez-Delgado G, Aguilera CM, Lozano-Sánchez J, Arráez-Román D, Segura-Carretero A, Ruiz JR. Activation of human brown adipose tissue by capsinoids, catechins, ephedrine, and other dietary components: a systematic review. *Adv Nutr.* 2019;10(2):291–302.
- [Peterson and Månsson 2013] Peterson P and Månsson S. Simultaneous quantification of fat content and fatty acid composition using MR imaging. *MRM.* 2013;69:688–697.
- [Peterson and Månsson 2014] Peterson P, Månsson S. Fat quantification using multiecho sequences with bipolar gradients: investigation of accuracy and noise performance. *Magn Reson Med.* 2014;71(1):219-29.
- [Peterson et al. 2014] Peterson P, Svensson J, Månsson S. Relaxation effects in MRI-based quantification of fat content and fatty acid composition. *Magn Reson Med.* 2014;72(5):1320-9.
- [Plewes and Kucharczyk 2012] Plewes DB and Kucharczyk W. Physics of MRI: a primer. *JMRI;*2012;35:1038-1054.
- [Polimeni and Uludağ 2018] Polimeni JR, Uludağ K. Neuroimaging with ultra-high field MRI: Present and future. *Neuroimage* 2018;168:1–6.
- [Purcell et al.1946] Purcell EM, Torrey HC, Pound RV. Resonance absorption by nuclear moments in a solid. *Phys Rev.* 1946;69:37–38.
- [Qaid and Abdelrahman 2016] Qaid MM and Abdelrahman MM. Role of insulin and other related hormones in energy metabolism—A review. *Cogent Food & Agriculture.* 2016;2:1267691.

- [Qayyum 2009] Qayyum A. MR spectroscopy of the liver: principles and clinical applications. *Radiographics*. 2009;29(6):1653–1664.
- [Quesson et al. 2000] Quesson B, de Zwart JA and Moonen CT. Magnetic resonance temperature imaging for guidance of thermotherapy. *J Magn Reson Imaging*. 2000;12(4):525–533.
- [Rabi et al. 1938] Rabi II, Zacharias JR, Millman S, Kusch P. A New Method of Measuring Nuclear Magnetic Moment. *Phys Rev*. 1938;53(4):318.
- [Ràfols 2014] Esteve Ràfols M. Adipose tissue: cell heterogeneity and functional diversity. *Endocrinol Nutr*. 2014;61(2):100–112.
- [Raiko and Holstila et al. 2015] Raiko J, Holstila M, Virtanen KA, Orava J, Saunavaara V, Niemi T, Laine J, Taittonen M, Borra RJH, Nuutila P, Parkkola R. Brown adipose tissue triglyceride content is associated with decreased insulin sensitivity, independently of age and obesity. *Diabetes Obes Metab*. 2015;17(5):516–519.
- [Raiko et al. 2020] Raiko J, Koskensalo K and Sainio T. Imaging-based internal body temperature measurements: The journal Temperature toolbox. 2020. DOI: 10.1080/23328940.2020.1769006.
- [Reber et al. 2018] Reber J, Willershäuser M, Karlas A, Paul-Yuan K, Diot G, Franz D, Fromme T, Ovsepiyan SV, Bézière N, Dubikovskaya E, Karampinos DC, Holzapfel C, Hauner H, Klingenspor M, Ntziachristos V. Non-invasive measurement of brown fat metabolism based on optoacoustic imaging of hemoglobin gradients. *Cell Metab*. 2018;27(3):689–701.e4.
- [Reeder et al. 2012] Reeder SB, Hu HH, Sirlin CB. Proton Density Fat-Fraction: A Standardized MR-Based Biomarker of Tissue Fat Concentration. *J Magn Reson Imaging*. 2012;36(5):1011–1014.
- [Ren 2008] Composition of adipose tissue and marrow fat in humans by ¹H NMR at 7 Tesla. *J Lipid Res*. 2008; 49(9): 2055–2062.
- [Rhodes 2017] Rhodes CJ. Magnetic resonance spectroscopy. *Sci Prog*. 2017;100(3):241–292.
- [Rogers 2015] Rogers NH. Brown adipose tissue during puberty and with aging. *Ann Med*. 2015;47(2):142–149.
- [Rosenwald 2013] Rosenwald M, Perdikari A, Rüllicke T, Wolfrum C. Bi-directional interconversion of brite and white adipocytes. *Nat Cell Biol*. 2013;15(6):659–667
- [Ruschke et al 2016] Ruschke S, Kienberger H, Baum T, Kooijman H, Settles M, Haase A, Rychlik M, Rummeny EJ, Karampinos DC. Diffusion-weighted stimulated echo acquisition mode (DW-STEAM) MR spectroscopy to measure fat unsaturation in regions with low proton-density fat fraction. *Magn Reson Med*. 2016;75(1):32–41.

- [Saito et al 2009] Saito M, Okamatsu-Ogura Y, Matsushita M, Watanabe K, Yoneshiro T, Nio-Kobayashi J, Iwanaga T, Miyagawa M, Kameya T, Nakada K, Kawai Y, Tsujisaki M. High incidence of metabolically active brown adipose tissue in healthy adult humans: effects of cold exposure and adiposity. *Diabetes*. 2009;58(7):1526–1531.
- [Saponaro et al. 2015] Saponaro C, Gaggini M, Carli F, Gastaldelli A. The subtle balance between lipolysis and lipogenesis: a critical point in metabolic homeostasis. *Nutrients*. 2015;7(11):9453–9474.
- [Sarasniemi et al. 2018] Sarasniemi JT, Koskensalo K, Raiko J, Nuutila P, Saunavaara J, Parkkola R, Virtanen KA. Skin temperature may not yield human brown adipose tissue activity in diverse populations. *Acta Physiol (Oxf)*. 2018;224(3):e13095.
- [Sbarbati et al. 2006] Sbarbati A, Cavallini I, Marzola P, Nicolato E, Osculati F. Contrast-enhanced MRI of brown adipose tissue after pharmacological stimulation. *Magn Reson Med*. 2006;55:715–718.
- [Schreiber et al. 2017] Schreiber R, Diwoky C, Schoiswohl G, Feiler U, Wongsiriroj N, Abdellatif M, Kolb D, Hoeks J, Kershaw EE, Sedej S, Schrauwen P, Haemmerle G, Zechner R. Cold-induced thermogenesis depends on ATGL-mediated lipolysis in cardiac muscle, but not brown adipose tissue. *Cell Metab*. 2017;26(5):753–763
- [Schumaker and Adams 1969] Schumaker VN and Adams GH. Circulating lipoproteins. *Annu. Rev. Biochem*. 1969;38:113–136.
- [Seale et al 2008] Seale P, Bjork B, Yang W, Kajimura S, Chin S, Kuang S, Scimè A, Devarakonda S, Conroe HM, Erdjument-Bromage H, Tempst P, Rudnicki MA, Beier DR, Spiegelman BM. PRDM16 controls a brown fat/skeletal muscle switch. *Nature*. 2008 Aug 21;454(7207):961–967
- [Sharp et al. 2012] Sharp LZ, Shinoda K, Ohno H, Scheel DW, Tomoda E, Ruiz L, Hu H, Wang L, Pavlova Z, Gilsanz V, Kajimura S. Human BAT possesses molecular signatures that resemble beige/brite cells. *PLoS One*. 2012;7(11):e49452.
- [Shin et al. 2017] Shin H, Ma Y, Chanturiya T, Cao Q, Wang Y, Kadegowda AKG, Jackson R, Rumore D, Xue B, Shi H, Gavrilova O, Yu L. Lipolysis in brown adipocytes is not essential for cold-induced thermogenesis in mice. *Cell Metab*. 2017;26(5):764–777
- [Shmookler Reis et al. 2011] Shmookler Reis RJ, Xu L, Lee H, Chae M, Thaden JJ, Bharill P, Tazearslan C, Siegel E, Alla R, Zimniak P, Ayyadevara S. Modulation of lipid biosynthesis contributes to stress resistance and longevity of *C. elegans* mutants. *Aging (Albany NY)*. 2011;3(2):125-47.
- [Simhick et al. 2017] Simhick G, Yin A, Yin H, Zhao Q, editors. Dynamic monitoring of brown adipose tissue activation and white adipose tissue beiging. *Proceedings of 25th Int Society for Magnetic Resonance in Medicine*. Honolulu, HI; 2017.

- [Smith and Horwitz] Smith RE, Horwitz BA. Brown fat and thermogenesis. *Physiol Rev.* 1969;49(2):330–425.
- [Soher et al 1996] Soher BJ, Hurd RE, Sailasuta N and Barker PB. Quantitation of Automated Single-Voxel Proton MRS Using Cerebral Water as an Internal Reference. *Magn Reson Med.* 1996;36:335–339.
- [Strobel 2001] Strobel K, van den Hoff J and Pietzsch. Localized proton magnetic resonance spectroscopy of lipids in adipose tissue at high spatial resolution in mice in vivo. *Journal of Lipid Research.* 2008;49:473–480.
- [Symonds et al. 2012] Symonds ME, Henderson K, Elvidge L, Bosman C, Sharkey D, Perkins AC, Budge H. Thermal imaging to assess age-related changes of skin temperature within the supraclavicular region co-locating with brown adipose tissue in healthy children. *J Pediatr.* 2012;161(5):892–898.
- [Tan et al. 2015] Tan CY, Virtue S, Bidault G, Dale M, Hagen R, Griffin JL, Vidal-Puig A. Brown adipose tissue thermogenic capacity is regulated by Elov16. *Cell Rep.* 2015;13(10):2039–2047.
- [Tortora and Derrickson 2011] Tortora GJ and Derrickson B. Principles of anatomy and physiology. 13th edition. New York, United States. John Wiley & Sons Inc; 2011. 1344 p.
- [Törnroth-Horsefield and Neutze 2008] Törnroth-Horsefield S, Neutze R. Opening and closing the metabolite gate. *Proc Natl Acad Sci U S A.* 2008;105(50):19565–19566
- [U Din et al. 2016] U Din M, Raiko J, Saari T, Kudomi N, Tolvanen T, Oikonen V, Teuvo J, Sipilä HT, Savisto N, Parkkola R, Nuutila P, Virtanen KA. Human brown adipose tissue [(15)O]O₂ PET imaging in the presence and absence of cold stimulus. *Eur J Nucl Med Mol Imaging.* 2016;43(10):1878–1886.
- [U Din et al. 2017] U Din M, Raiko J, Saari T, Saunavaara V, Kudomi N, Solin O, Parkkola R, Nuutila P, Virtanen KA. Human brown fat radiodensity indicates underlying tissue composition and systemic metabolic health. *J Clin Endocrinol Metab.* 2017;102(7):2258–2267
- [Wadsak and Mitterhauser 2010] Wadsak W, Mitterhauser M. Basics and principles of radiopharmaceuticals for PET/CT. *Eur J Radiol.* 2010;73(3):461-469.
- [van der Graaf 2010] van der Graaf M. In vivo Magnetic resonance spectroscopy: basic methodology and clinical applications. *Eur Biophys J.* 2010;39:527–540.
- [van Marken Lichtenbelt et al 2009] van Marken Lichtenbelt WD, Vanhommerig JW, Smulders NM, Drossaerts JM, Kemerink GJ, Bouvy ND, Schrauwen P, Teule GJ. Cold-activated brown adipose tissue in healthy men. *N Engl J Med.* 2009;360(15):1500–1508.
- [Verma et al. 2017] Verma SK, Nagashima K, Yaligar J, Michael N, Lee SS, Xianfeng T, et al. Differentiating brown and white adipose tissues by high-resolution diffusion NMR spectroscopy. *J Lipid Res.* 2017; 58:289–298.

- [Vessby et al. 2002] Vessby B, Gustafsson I-B, Tengblad S, Boberg M and Andersson A, Desaturation and elongation of fatty acids and insulin action. *Ann. N.Y. Acad. Sci.* 2002;967:183–195.
- [Wilson et al. 2019] Wilson M, Andronesi O, Barker PB, Bartha R, Bizzi A, Bolan PJ, et al. Methodological consensus on clinical proton MRS of the brain: Review and recommendations. *Magn Reson Med.* 2019;82(2):527-550.
- [Virtanen et al 2009] Virtanen KA, Lidell ME, Orava J, Heglind M, Westergren R, Niemi T, Taittonen M, Laine J, Savisto NJ, Enerbäck S, Nuutila P. Functional brown adipose tissue in healthy adults. *N Engl J Med* 2009; 360(15):1518–1525;
- [Wu et al. 2012] Wu J, Boström P, Sparks LM, Ye L, Choi JH, Giang AH, Khandekar M, Virtanen KA, Nuutila P, Schaart G, Huang K, Tu H, van Marken Lichtenbelt WD, Hoeks J, Enerbäck S, Schrauwen P, Spiegelman BM. Beige adipocytes are a distinct type of thermogenic fat cell in mouse and human. *Cell.* 2012;150(2):366–376.
- [Wu et al. 2020] Wu M, Junker D, Branca RT, Karampinos DC. Magnetic resonance imaging techniques for brown adipose tissue detection. *Front Endocrinol (Lausanne).* 2020;11:421
- [Xu et al 2019] Xu Z, You W, Zhou Y, Chen W, Wang Y, Shan T. Cold-induced lipid dynamics and transcriptional programs in white adipose tissue. *BMC Biol.* 2019;17(1):74.
- [Yaligar et al. 2019] Yaligar J, Verma SK, Gopalan V, Anantharaj R, Thu Le GT, Kaur K, Mallilankaraman K, Shing Leow MK, Velan SS. Dynamic contrast-enhanced MRI of brown and beige adipose tissues. *Magn Reson Med.*2019;84:384–95.
- [Yamada et al 1995] Yamada S, Kubota K, Kubota R, Ido T, Tamahashi N. High accumulation of fluorine-18-fluorodeoxyglucose in turpentine-induced inflammatory tissue. *J Nucl Med* 1995; 36:1301–1306.
- [Yoneshiro et al. 2011] Yoneshiro T, Aita S, Matsushita M, Kameya T, Nakada K, Kawai Y, Saito M. Brown adipose tissue, whole-body energy expenditure, and thermogenesis in healthy adult men. *Obesity (Silver Spring).* 2011;19(1):13–16
- [Yoon et al 2018] Yoon BK, Jackman JA, Valle-González ER, Cho NJ. Antibacterial free fatty acids and monoglycerides: biological activities, experimental testing, and therapeutic applications. *Int J Mol Sci.* 2018;19(4):1114.
- [Zhou et al. 2018] Zhou J, Wu NN, Yin RL, Ma W, Yan C, Feng YM, Zhang CH, Zhao D. Activation of brown adipocytes by placental growth factor. *Biochem Biophys Res Commun.* 2018;504(2):470–477.
- [Zingaretti et al. 2009] Zingaretti MC, Crosta F, Vitali A, Guerrieri M, Frontini A, Cannon B, Nedergaard J, Cinti S. The presence of UCP1 demonstrates that metabolically active adipose tissue in the neck of adult humans truly represents brown adipose tissue. *Faseb J* 2009; 23(9):3113–3120.

[Zou et al. 2018] Zou R, Xiong T, Zhang L, Li S, Zhao F, Tong Y, Qu Y, Mu D. Proton magnetic resonance spectroscopy biomarkers in neonates with hypoxic-ischemic encephalopathy: a systematic review and meta-analysis. *Front Neurol.* 2018;9:732.

[Öz et al. 2014] Öz G, Alger JR, Barker PB, Bartha R, Bizzi A, Boesch C, Bolan PJ, Brindle KM, Cudalbu C, Diñçer A, Dydak U, Emir UE, Frahm J, González RG, Gruber S, Gruetter R, Gupta RK, Heerschap A, Henning A, Hetherington HP, Howe FA, Hüppi PS, Hurd RE, Kantarci K, Klomp DW, Kreis R, Kruiskamp MJ, Leach MO, Lin AP, Luijten PR, Marjańska M, Maudsley AA, Meyerhoff DJ, Mountford CE, Nelson SJ, Pamir MN, Pan JW, Peet AC, Poptani H, Posse S, Pouwels PJ, Ratai EM, Ross BD, Scheenen TW, Schuster C, Smith IC, Soher BJ, Tkáč I, Vigneron DB, Kauppinen RA; MRS Consensus Group. Clinical proton MR spectroscopy in central nervous system disorders. *Radiology.* 2014;270(3):658–79.